
Highly accurate offline trajectory planning for industrial robots based on detailed kinematic and dynamic models

DIPLOMA THESIS

Conducted in partial fulfillment of the requirements for the degree of a
Diplom-Ingenieur (Dipl.-Ing.)

supervised by

Univ.-Prof. Dr. techn. A. Kugi
Dr. techn. B. Bischof

submitted at the

TU Wien

Faculty of Electrical Engineering and Information Technology
Automation and Control Institute

by

Ing. Robert Sturmlechner, BSc
Matriculation number 00928818
Wien
Österreich

Vienna, 10. November 2020

Complex Dynamical Systems Group

A-1040 Wien, Gußhausstr. 27–29, Internet: <https://www.acin.tuwien.ac.at>

Preamble

First of all, I would like to take the opportunity and thank Prof. Kugi for giving me the opportunity to write my Master's thesis under his supervision and work at the Automation and Control Institute. In particular, my special thanks go to my supervisor, Dr. Bernhard Bischof, for his guidance and support throughout the whole time of my Master's thesis. I cannot count all the things that I've learned from him, and I am deeply thankful for the insights that he provided. I would also like to thank Prof. Markus Vince, Dipl.-Ing. Michael Schwegel and Dr.techn. Christian Hartl-Nesic for fruitful discussions and for offering help whenever needed.

Moreover, I would like to thank my future parents-in-law for their permanent support and continuous encouragement during the entire time of my studies. They never doubted me which helped me a lot to continue believing in myself. I also would like to thank my mother and sister for believing in me.

Last but not least I would like to thank my fiancée for her support in all matters, her patience and guidance through the ups and downs of pursuing my studies. She of all people knows what hard work means, wherefore she managed to help me rise above myself more than once. I couldn't have done it without her.

Vienna, 10. November 2020

Abstract

Industrial robots are widely used in the production industry due to their cost-efficiency, high repeatability, and programmability. For a number of manufacturing processes, improving the robot's absolute accuracy is of crucial importance. Recent developments show that the demand shifts away from standardised products of high quantity towards individuality. Hence, to keep the production downtime due to changes in the process as short as possible, precise offline planning gains significance. While the repeatability of industrial robots being less than one millimeter is already satisfactory, the absolute accuracy still needs to be improved for a number of applications. Current research focuses on offline and online approaches to address this topic. The online approaches are typically based on adaptive or learning feedback controllers, which require additional sensors such as inertial measurement units. Offline approaches utilize calibrated models of the robot's kinematics and/or dynamics to determine control input trajectories for a predefined task that improve the absolute accuracy. In this thesis, an offline approach is developed that encompasses a precise kinematic model as well as non-constant gear ratios and non-linear stiffness of the drive chain. An optimal control problem is solved to determine optimal motor accelerations for a predefined trajectory, which minimize the position errors and are used as a reference trajectory for high-bandwidth joint velocity controllers. The approach in this work is developed for an industrial robot with six degrees of freedom. Results demonstrate that the presented approach is suitable, since the absolute accuracy by calibration is improved by 70%. As a conclusion it can be stated that it is worth accepting a higher effort during the offline planning stage in order to achieve improvements in the precision of industrial robots.

Kurzzusammenfassung

Aufgrund der zahlreichen Vorteile von Industrierobotern, wie beispielsweise Flexibilität, Wiederholgenauigkeit und Kosteneffizienz, werden diese immer häufiger für diverse Aufgaben in der Industrie herangezogen. Für viele Fertigungsprozesse ist es jedoch notwendig, die Absolutgenauigkeit von Industrierobotern weiter zu erhöhen. Jüngste Entwicklungen zeigen, dass sich die Nachfrage weg von standardisierten Produkten mit hoher Stückzahl hin zu individuellen Produkten mit geringer Quantität verschiebt. Um die Standzeiten aufgrund von notwendigen Prozessänderungen so kurz wie möglich zu gestalten, gewinnt die Offline-Planung an Bedeutung. Während sich die Wiederholgenauigkeit von Industrierobotern bereits im Millimeterbereich befindet, was durchaus als zufriedenstellend bezeichnet werden kann, besteht bei der Absolutgenauigkeit noch Verbesserungsbedarf für eine Vielzahl von Anwendungen. Derzeit werden sowohl online als auch offline Methoden zur Lösung dieses Problems erforscht. Online Methoden basieren auf geschlossenen Regelkreisen und stützen sich auf externe Sensoren wie z.B. der Inertialsensoren. Offline Methoden verwenden kalibrierte Modelle der Kinematik und/oder Dynamik des Roboters, um Referenztrajektorien für eine vordefinierte Aufgabe zu bestimmen, welche die Absolutgenauigkeit verbessern. In dieser Arbeit wird ein Offline-Ansatz entwickelt, der ein präzises kinematisches Modell sowie nicht konstante Getriebeübersetzungen und die nichtlineare Steifigkeit des Antriebes umfasst. Ein Optimalsteuerungsproblem wird gelöst, um optimale Motorbeschleunigungen für eine vordefinierte Trajektorie zu bestimmen, welche die Positionsfehler minimieren und als Referenztrajektorie für Drehzahlregler mit hoher Bandbreite verwendet werden. Die innerhalb dieser Arbeit entwickelte Methode erweist sich als geeignet, die Absolutgenauigkeit eines Industrieroboters zu erhöhen. Die Verbesserung durch Kalibrierung ist beträchtlich und liegt bei 70 %. Daraus kann geschlossen werden, dass der höhere Aufwand in der Offline-Planungsphase in Kauf genommen werden sollte, um entsprechende Verbesserungen in der Präzision von Industrierobotern zu ermöglichen.

Contents

Nomenclature	1
1 Introduction	3
1.1 Literature Review	4
1.1.1 Gear Transmission	4
1.1.2 Elastic Joints	7
1.1.3 Kinematic Parameter Identification	7
1.1.4 Offline Trajectory Planning	10
1.2 Aim and Overview of this Work	11
2 Modelling of Elastic Joint Robots	13
2.1 Kinematic Model	13
2.2 Dynamic System	14
2.2.1 Non-Constant Gear Ratio	16
2.2.2 Kinetic and Potential Energy	17
2.2.3 Equations of Motion	18
3 Parameter Identification	19
3.1 Non-Constant Gear Ratio Parameters	19
3.1.1 Identification Process	19
3.1.2 Results	23
3.2 Kinematic Model Parameters	30
3.2.1 Identifiable Parameters	30
3.2.2 Set of Identification Poses	32
3.2.3 Classical Identification	34
3.2.4 Results	35
4 Offline Trajectory Planning	37
4.1 Optimal Control Problem	37
4.2 Generation of Reference Trajectories	40
4.2.1 Polynomial Trajectory Planning	40
4.2.2 Numeric Inverse Kinematics	40
4.3 Trajectory Examples	41
4.3.1 Straight Line	42
4.3.2 Conical Spiral	47
5 Conclusion	53

A System Parameters	55
A.1 Non-Constant Gear Transmission	55
A.2 Modified Denavit-Hartenberg Parameters	56
A.3 Non-linear Stiffness	61
A.4 Dynamic Parameters	61

Die approbierte gedruckte Originalversion dieser Diplomarbeit ist an der TU Wien Bibliothek verfügbar.
 The approved original version of this thesis is available in print at TU Wien Bibliothek.

List of Figures

1.1	Components of different gears: a) Harmonic drive and b) Cycloid drive [4]	4
1.2	A typical transmission error of a strain wave gear (SWG) [6–8].	5
2.1	Schematic of the Robot COMAU Racer-7-1.4 [15]. In this work, q_i are the joint angles instead of θ_i . The wrist center point (WCP) is not used in this work, it is commonly used to separate the positioning and orientation task of the end-effector.	15
2.2	Motor M to link L connection representing an elasticity and a non-constant gear ratio.	16
3.1	Data processing sequence to calculate the kinematic error ω_e , where $\omega_{G,i} = [\omega_{G,i}(t_0) \dots \omega_{G,i}(t_{N-1})]^T$ with $i = [x, y, z]$ is the gyroscope data of the axis i and $\omega_{G,fa}$ is one filtered rotation axis component $\omega_{G,j}$, $j \in [x, y, z]$	21
3.2	Gyroscope mounting places on the COMAU Racer-7-1.4.	22
3.3	Fast Fourier Transform (FFT) result of the kinematic error of the first gear of a clockwise (CW) rotation (in red) and a counter-clockwise (CCW) rotation (in blue). The constant motor angular rate was $7468^\circ/\text{s}$ (link side angular rate is $\sim 88^\circ/\text{s}$).	24
3.4	Comparison of the kinematic error of the first gear previous to the compensation (in red) and after the compensation (in blue) at a motor speed of $7468^\circ/\text{s}$ (link side speed is $\sim 88^\circ/\text{s}$).	25
3.5	Comparison of the kinematic error of the first gear before the compensation (in red) and after the compensation (in blue) at a motor speed of $3734^\circ/\text{s}$ (link side speed is $\sim 44^\circ/\text{s}$) which is $\sim 20\%$ of the maximal velocity. . . .	26
3.6	Fast Fourier Transform result of the kinematic error of the second gear of a clockwise (CW) rotation (in red) and a counter-clockwise (CCW) rotation (in blue). The constant motor angular rate was $8300^\circ/\text{s}$ (link side angular rate is $\sim 100^\circ/\text{s}$).	27
3.7	Comparison of the kinematic error of the second gear before the compensation (in red) and after the compensation (in blue) at a motor speed of $8300^\circ/\text{s}$ (link side speed is $\sim 100^\circ/\text{s}$).	27
3.8	Fast Fourier Transform result of the kinematic error of a clockwise (CW) rotation (in red) and a counter-clockwise (CCW) rotation (in blue). The constant motor angular rate was $4192^\circ/\text{s}$ (link side angular rate is $\sim 61^\circ/\text{s}$).	28
3.9	Comparison of the kinematic error previous to the compensation (in red) and after the compensation (in blue) at a motor speed of $4.19 \cdot 10^3^\circ/\text{s}$ (link side speed $\sim 61^\circ/\text{s}$).	29
3.10	Installation of the sensor system and the robot COMAU Racer-7-1.4. . . .	33

3.11	Positions of the end-effector for the determined pose set with the DETMAX algorithm are drawn as yellow dots with black border. The blue dots indicate random possible end-effector positions to get an idea about the workspace of the robot.	34
3.12	Euclidian distance from the nominal to the measured position of the end-effector of the validation configuration set in red and blue, respectively.	35
4.1	Path velocity of the straight line trajectory. Result using the optimal control input determined with (4.3) and a weighting factor of $\nu = 10^{-14}$	42
4.2	Norm of the position error $\ \mathbf{p}_d - \mathbf{p}_e\ _2$ of the straight line trajectory. Two results with different weighting values are compared.	43
4.3	Frequency analysis of the control input $\mathbf{u} = \ddot{\boldsymbol{\theta}}$ calculated with two different weighting values ν for all axes (axis 1 (a), axis 2 (b), axis 3 (c), axis 4 (d), axis 5 (e) and axis 6 (f)) of the straight line example.	44
4.4	Comparison of the control input $u_2 = \ddot{\theta}_2$ in (a) and the states ($\dot{\theta}_2$ and \dot{q}_2 in (b) and (c), respectively) of axis 2 of the straight line trajectory calculated with different weighting factors ν	45
4.5	Errors of the link angles (a), of the orientation of the end-effector (b) and of the position of the end-effector (c) for the straight line trajectory. The optimal control problem is solved with a weighting factor of $\nu = 10^{-14}$	45
4.6	The control input $\mathbf{u} = \ddot{\boldsymbol{\theta}}$ and the angular rate at the motor side $\dot{\boldsymbol{\theta}}$ is depicted in (a) and (b), respectively, for the straight line trajectory. The optimal control problem is solved with a weighting factor of $\nu = 10^{-14}$	46
4.7	The angular rate at the link side $\dot{\mathbf{q}}$ for the straight line trajectory. The optimal control problem is solved with a weighting factor of $\nu = 10^{-14}$	46
4.8	Comparison between the desired and the calculated conical spiral trajectory including orientation frames of the end-effector.	47
4.9	Velocity of the conical spiral trajectory. Result using the optimal control input determined with (4.3) and a weighting factor of $\nu = 10^{-14}$	48
4.10	Frequency analysis for the control input $\mathbf{u} = \ddot{\boldsymbol{\theta}}$ calculated with different weighting factors ν for all axes (axis 1 (a), axis 2 (b), axis 3 (c), axis 4 (d), axis 5 (e) and axis 6 (f)) of the conical spiral example.	49
4.11	Comparison of the control input $u_2 = \ddot{\theta}_2$ (a) and the states ($\dot{\theta}_2$ in (b) and \dot{q}_2 in (c)) of axis 2 of the conical spiral trajectory calculated with different weighting factors ν	50
4.12	Norm of the position error $\ \mathbf{p}_d - \mathbf{p}_e\ _2$ of the conical spiral trajectory. Two results with different weighting factors are compared. A larger weighting factor ν increases the error significantly.	50
4.13	Errors of the link angles (a), of the orientation of the end-effector (b) and of the position of the end-effector (c) for the conical spiral trajectory. The optimal control problem is solved with a weighting factor of $\nu = 10^{-14}$	51
4.14	Angular rate at the link side $\dot{\mathbf{q}}$ of the conical spiral trajectory. The optimal control problem is solved with a weighting factor of $\nu = 10^{-14}$	51

4.15	The control input $\mathbf{u} = \ddot{\boldsymbol{\theta}}$ of the conical spiral trajectory is illustrated in (a) and (b). The angular rate at the motor side $\dot{\boldsymbol{\theta}}$ is depicted in (c) and (d) of the conical spiral trajectory. The optimal control problem is solved with a weighting factor of $\nu = 10^{-14}$	52
A.1	The stiffness curve of axis 2 (a) and 3 (b) determined by load experiments by Moien Reyhani-Masouleh.	61

List of Tables

3.1	Comparison of the mean gyroscope data in each direction before the alignment of the rotation axis and after the alignment for a counter-clockwise (CCW) rotation of the first gear.	24
3.2	The RMS values of the kinematic error of the first gear before and after the compensation of different measurements.	25
3.3	The RMS values of the kinematic error previous to and after the compensation of different measurements.	26
3.4	The RMS values of the kinematic error before and after the compensation of different measurements.	29
3.5	A list of identifiable mDH parameters of the COMAU Racer-7-1.4 with position measurements (i: identifiable, n: not identifiable, x: not existing).	32
3.6	Position errors of the optimisation set before and after the calibration, in meter.	35
3.7	Position errors of the validation set before and after the calibration, in meter.	36
3.8	A list of identified mDH parameter deviations and the basic gear transmission ratios of gear 4, 5 and 6 of the COMAU Racer-7-1.4. The basic gear transmission ratios of gear 1 to 3 are identified in Section 3.1.	36
A.1	List of the joint position limits.	55
A.2	List of the joint angular velocity limits.	55
A.3	List of the joint angular acceleration limits.	55
A.4	3 dB frequencies of the acausal Gaussian filter used to process the raw sensor data at gears.	56
A.5	Basic gear ratio u_0 of each gear ($\theta = u_0\varphi$).	56
A.6	Calculated Fourier series parameters for the gear ratio of the first gear at a link side speed of $\sim 88^\circ/\text{s}$ (clockwise rotation).	56
A.7	Calculated Fourier series parameters for the gear ratio of the second gear at a link side speed of $\sim 100^\circ/\text{s}$ (clockwise rotation).	57
A.8	Calculated Fourier series parameters for the gear ratio of the third gear at a link side speed of $\sim 61^\circ/\text{s}$ (clockwise rotation).	57
A.9	Calculated Fourier series parameters for the gear ratio of the first gear at a link side speed of $\sim 88^\circ/\text{s}$ (counter-clockwise rotation).	57
A.10	Calculated Fourier series parameters for the gear ratio of the second gear at a link side speed of $\sim 100^\circ/\text{s}$ (counter-clockwise rotation).	58
A.11	Calculated Fourier series parameters for the gear ratio of the third gear at a link side speed of $\sim 61^\circ/\text{s}$ (counter-clockwise rotation).	58
A.12	Nominal mDH parameters of the COMAU Racer-7-1.4 [15].	58

A.13 First half of the 50 robot configurations, used to identify the mDH parameters of the COMAU Racer-7-1.4.	59
A.14 Second half of the 50 robot configurations, used to identify the mDH parameters of the COMAU Racer-7-1.4.	60

Nomenclature

General Notation

a, A, ν, \dots	scalars
$\mathbf{a}, \mathbf{A}, \boldsymbol{\nu}, \dots$	vectors and matrices
$\dot{a}, \dot{\theta}, \dots$	total derivative with respect to time
$\ddot{a}, \ddot{\theta}, \dots$	second-order total derivative with respect to time
$\mathbf{q}_i, \mathbf{q}_{0,i}$	i th element of the vectors \mathbf{q} and \mathbf{q}_0 with $i \in \mathbb{N}$
$\hat{a}, \hat{u}, \hat{m}, \dots$	amplitude
\tilde{a}, f	frequency
$a_d, \mathbf{p}_d, \mathbf{R}_d, \dots$	desired quantity

General Symbols

t	time in seconds (s)
$\mathbf{0}_{m \times n}$	vector or matrix exclusively containing zeros with m rows and n columns
$\mathbf{I}_{m \times m}$	identity matrix with m rows and m columns
$\mathbf{R}_i(\alpha)$	rotation matrix of angle α around axis i
$\mathbf{t}_i(d)$	translation vector of length d in direction i
$\mathbf{T}_{i-1}^i, \mathbf{H}_{i-1}^i$	homogeneous transformation matrix from frame $i-1$ to frame i
\mathbf{R}_e	orientation of the end-effector in the inertial frame $(0, x_0, y_0, z_0)$
\mathbf{p}_e	position of the end-effector in the inertial frame $(0, x_0, y_0, z_0)$
θ	motor rotary angle
u, Ξ	gear ratio, from the drive side to the output side of a gear
u_0	basic gear ratio
φ	virtual inner link angle
$\Delta\varphi_g$	deflection due to gravity
$\boldsymbol{\tau}_g$	torque induced by gravity
\mathbf{q}	link angle
$\boldsymbol{\omega}_e$	kinematic error in $^\circ/\text{s}$
$\boldsymbol{\xi}$	generalised coordinates
L	Lagrange function
T	kinetic energy
V	potential energy
\mathbf{D}	mass matrix
\mathbf{C}	Coriolis matrix
\mathbf{g}	vector of potential forces
$\boldsymbol{\tau}$	generalised force vector
m	mass
\mathbf{c}	vector to the center of mass
$\boldsymbol{\kappa}$	elastic torque

τ_{ext}	vector of external forces
τ_d	vector of motor forces
τ_f	vector of friction forces
T_s	sampling time
t_0	initial time
ω_G	gyroscope data
ζ	vectorized modified Denavit-Hartenberg parameter
\mathbf{J}_I	identification Jacobian
O_i	observability index i
\mathbf{x}	system states
ν	weighting factor
\mathbf{u}	control input vector

1 Introduction

Nowadays, industrial robots are used for a variety of different tasks due to their flexibility, repeatability and cost-efficiency. For specific robotic applications such as milling, surgery and painting, the absolute accuracy is of significant importance. Moreover, the demand for individualised products increases. Thus, robot cells often need to be adapted for each individual product. Such adaptations do not only take a significant amount of time but also force the manufacturing process to be interrupted. Hence, offline planning becomes more important. During the stage of offline planning, the manufacturing process of a new product is designed, while the robot cell continues working on the current task. Since high absolute accuracy as well as high repeatability need to be ensured, a precise preparation during the offline planning phase is crucial.

While the repeatability of industrial robots lies already below 1 mm, the low absolute accuracy, being within several millimeters, is still a major drawback. Two types of errors typically occur. On the one hand, there are non-geometric errors such as link compliance, gear backlash, thermal expansion and most important gear elasticity. On the other hand, geometric errors such as a wrong link length might also appear.

So far, a number of studies have been conducted to either increase the absolute accuracy by focusing on stationary or dynamic cases or both. In the stationary case, a calibration of the kinematic model and incorporating effects like joint elasticity improves the absolute accuracy. An identification of the dynamic parameters increases the accuracy for the dynamic case, incorporating effects like friction or non-constant gear ratio into the dynamic model of a robot.

The motivation of this work is to address this field of research by deriving accurate kinematic and dynamic models, which also take into consideration elastic gear transmissions and non-constant gear ratios. The models are then used to determine optimal motor trajectories by solving an optimal control problem to achieve highly accurate trajectories of the robot's end-effector. The methods in this work are developed for an industrial robot with six degrees of freedom and serial kinematics.

The advanced models are used for offline planning of a motor acceleration trajectory for each joint. The kinematic model is improved through a calibration, which is employed to generate a desired angle trajectory for each joint for a given Cartesian trajectory. An optimal control problem is designed using the desired angles to determine the motor acceleration trajectories based on the enhanced dynamic model. The accuracy of the dynamic model is improved by calibrating the dynamic parameters and including the elasticity of the drive chain as well as the non-constant gear ratios in the model.

1.1 Literature Review

Since the aim of this work is to improve the absolute accuracy of an industrial robot, the following literature review covers some essential related topics. Section 1.1.1 and Section 1.1.2 give a short literature overview concerning gear transmission and gear elasticity, respectively. The parameters of the kinematic model are extracted from CAD drawings rather than being measured on the assembled robot. This results in the necessity to identify the real kinematic parameters. A selection of relevant literature in this field of research is provided in Section 1.1.3. As a last step in this chapter, some ideas of offline trajectory generation are given in Section 1.1.4.

1.1.1 Gear Transmission

The manufacturers of serial, man-sized industrial robots mainly use strain wave gearings (SWG) due to their multiple advantages such as minor to zero backlash, high repeatability and accuracy, high torsional and tilting stiffness, small size, light weight and high reduction ratio, see [1, Chapter 4 and 11] and [2, 3]. There exist two types of SWG (Harmonic drives and Cycloid drives) which are shown in Figure 1.1. Effects such as friction, manufacturing

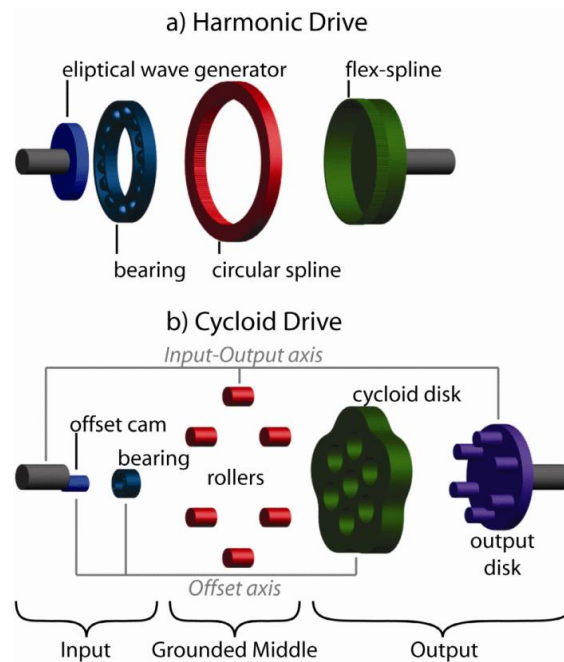


Figure 1.1: Components of different gears: a) Harmonic drive and b) Cycloid drive [4]

tolerances, expansion and contraction, which occur due to temperature, assembling errors and wear lead to errors in the transmission ratio of the gears. A typical transmission error of a SWG is given in [2, 3] and depicted in Figure 1.2. Measurements of the gear's output side show that the transmission error, defined as the difference between input and output angular rate, is periodic and can, therefore, be approximated by a Fourier series [5].

The research mainly focuses on the transmission error of Harmonic drives and rarely on Cycloid drives. Nevertheless, the characteristic of the transmission error of Cycloid drives is identical to Harmonic drives due to the similar operating principle [4]. Therefore, it is possible to apply the existing approaches for Harmonic drives to Cycloid drives, which are installed on the provided industrial robot.

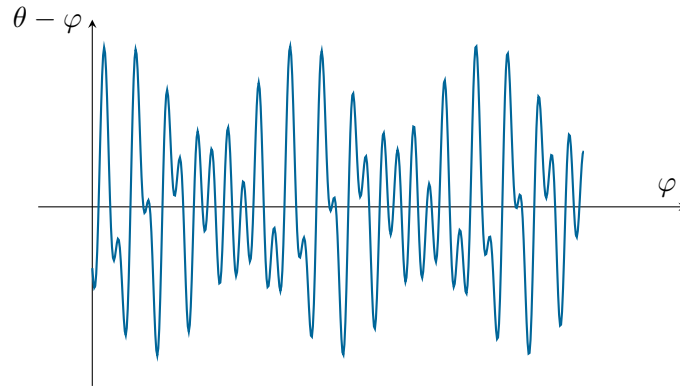


Figure 1.2: A typical transmission error of a strain wave gear (SWG) [6–8].

Shi et al. [6] define a transmission error of a Harmonic drive, which includes a deformation of the flexible spine, a misalignment in the wave generator, and a kinematic error. The error is identified by an offline method. The kinematic error itself is composed of a linear term and a sum of harmonics. The harmonic orders are determined by a Fast Fourier Transformation (FFT) of the unbiased kinematic error. The angle at the output side and the drive side of the gear are measured with absolute encoders at a test bench. Then, three steps are carried out: Firstly, the bias is removed from the data. Secondly, the harmonic orders are determined by the FFT. Thirdly, amplitudes and phase shifts are calculated using the FFT data. There are no numerical results given but it is shown that the kinematic error is independent of the velocity and that it is sufficiently compensated for clockwise and counter-clockwise rotations.

Ghorbel et al. [7] decompose the kinematic error of a Harmonic drive into a basic component and one related to stiffness. The basic component is approximated by a Fourier series and a basic transmission. The coefficients of the Fourier series are determined by numerical integration of the measured data. The impact of the load on the kinematic error is investigated, showing that a high load decreases the amplitude of the error. The load dependency is not added to the final model in order to reduce the complexity, since each dynamic load would require a specific profile to be compensated. An angular speed test shows that un-modelled dynamics, e.g. friction, as well as excitations due to high speed lead to deviations between the measured and the simulated angle error at high frequencies. At low speed, the high frequency components are less significant than at high speed. The kinematic error model is used in the dynamic model of a Harmonic drive, where a scaling with the velocity is natural. Again, the measurements are conducted on a test bench with encoders on each end of the gear. No exact numbers are given, however,

it is shown that the presented model of the kinematic error is useful to model Harmonic drive dynamics accurately.

Yamamoto et al. [8] break down the kinematic error of a Harmonic drive into a synchronous and a non-linear elastic component. A sum of harmonics is determined from the spectrum of the error above a given threshold and used to approximate the synchronous component of the kinematic error. The non-linear elastic component is estimated with a conceptual non-linear hysteresis model based on the conventional rolling friction. The parameters of the hysteresis model are identified by a trial and error experiment to fit recorded waveforms. A more precise variant would have been an identification using experiments with force sensors. The experimental setup consists of two encoders, a gear, a motor, an inertia load and an angular feedback controller. Yamamoto et al. show that their model approximates the angular transmission error very well. The 3σ value is reduced by approximately 40 %, with σ being the standard deviation.

In Thümmel's thesis [9], the transmission of a Cycloid drive is approximated by a Fourier series with a basic transmission component. The frequencies are divided into two parts, the first part being the basis frequency with some higher harmonics and the second is a frequency equal to the number of teeth of the gear with a small number of higher harmonics. In the end, just two frequencies are used. The other parameters, amplitude and phase shift, are adjusted in the course of an optimisation procedure of the dynamic robot parameters, including for example the mass, and the inertia.

Each axis is measured individually. A sensor fusion of an optical coordinate measuring tool, a gyroscope, and an acceleration sensor is performed to obtain the angle and angular rate from the output side of the gear. The angle on the drive side is measured with an encoder. Friction and stiffness are identified by specific measurements. The model fits the measurements to approximately 70 % [10].

Tönshoff et al. [11] divide the transmission error of a precision gear into an elastic error caused by the load and a kinematic error introduced by finite finishing accuracy of the teeth. The kinematic error is approximated as in [8]. The FFT of the measured error is not sufficient to identify the harmonics because the desired resolution is not achievable due to the limited positioning range of robots and machine tools. Therefore, the Chirp-Z Transformation (CZT) is used to determine the frequency and phase out of the combined results of three experiments. Rabiner et al. [12] state that applications for the CZT are high resolution, narrowband frequency analysis, spectral analysis and time interpolation, thereby supporting [11]. Measurements are conducted on a test bench with an acceleration sensor at the output shaft. The overall compensation of the errors is approximately 60 %.

In most of the above mentioned works, the gear is mounted on a test bench and not installed in a robot [3, 6–8]. Hence, the harmonics of the transmission error can be easily found. If a gear is built in a robot, it is impossible to exactly identify the harmonics [9, 11], since the range of 2π cannot be covered.

In this thesis, a priori knowledge about the number of the gear's teeth is not available. The gear transmission is approximated with a sum of harmonics plus a basic transmission. The harmonics are identified by a FFT based on the kinematic error and the direct neighbours of the identified components are added to the model to make up for the imprecise identification.

1.1.2 Elastic Joints

The installed SWGs are intrinsically flexible due to their mechanical structure [13, 14]. Their elasticity can be covered by a non-linear approach [7, 8], or by a linear spring [1, 15]. The generalised coordinates of an industrial robot are the link angle positions. By considering elastic joints, the generalised coordinates must be extended by the motor positions. This doubles the number of states contained in the dynamic model [14]. In this work, the elasticity of the second and third gear is taken into account by a non-linear stiffness model, which is determined by load experiments using a 6-DOF force sensor. Linear stiffness is assumed for the remaining gears.

1.1.3 Kinematic Parameter Identification

The forward kinematics of an industrial robot can be specified by different methods. The methods range from combinations of homogeneous transformations to *products of exponentials* (POE) [1, 16, 17]. Usually, the *Denavit-Hartenberg* (DH) convention is used in industrial robot controllers and in the scientific community, because it represents a minimal set of parameters for the robot's kinematics [18]. It consists of two rotations and two translations to describe the transformation between two adjacent links by four parameters.

The disadvantage of the DH convention is that two parallel links with a parameter deviation, small or big, can lead to significant pose errors. Hence, Hayati et al. [19] extended the DH convention with an additional parameter β_i that describes a rotation about the y -axis at the frame i . This convention is referred to as *modified Denavit-Hartenberg* (mDH) in this thesis.

The mDH parameters are obtained from the technical drawings of the robot. In reality, the parameters deviate from their nominal values due to manufacturing tolerances. Calculating the forward kinematics with these nominal mDH parameters induces position and orientation errors. Therefore, an identification of those deviations is necessary to improve the absolute accuracy.

The classical calibration method for parameters of a robot arm, with a serial kinematics, is based on a least-squares approach [18]. The forward kinematics is a non-linear function of the mDH-parameters and the generalised coordinates. A linearisation of the kinematic model, by a Taylor series expansion at the estimated values of the parameters, provides a basis for the identification [1, Chapter 6]. Khalil et al. [20] demonstrate that, despite the numerous methods to identify parameters of kinematic models, the

classical approach supports the largest number of identifiable parameters. The planar calibration method uses measured end points in the same geometrical plane, which reduces the number of identifiable parameters by approximately 12%. The frame link method exploits the possibility that for some end-effector locations more than one configuration exists. This method reduces the amount of identifiable parameters by approximately 30%.

In statistics, the form of the approximation with a Taylor series expansion is called a regression model where the regressor matrix represents the sensitivity of the robot pose due to parameter deviations [1]. In robot calibration tasks, the regressor matrix is also called the identification Jacobian. This raises the following questions: what if the regressor matrix is singular and is there a method to utilise the property of sensitivity of the regressor matrix for the identification process?

The identification Jacobian can be ill-conditioned (nearly singular) due to a bad choice of poses, which will be discussed later. A singular identification Jacobian indicates that at least one parameter is not identifiable because it has no effect on the model or its effect is grouped with others [20]. The parameter deviations which are not identifiable can be determined by mathematical methods (numerical as well as analytical) and by analysing the structure of the robot.

The numerical methods examine different decompositions of the regressor matrix of N poses. Thereby, N must be much larger than the amount of parameters for useful results. One approach is to exploit the QR decomposition, where the regressor matrix is decomposed as a combination of an orthogonal and an upper triangular matrix. The diagonal elements of the upper triangular matrix which are zero or close to zero indicate the subscript/index of the unidentifiable parameters. Another numerical method is the singular value decomposition (SVD). The identification Jacobian is decomposed into two unitary matrices and a rectangular diagonal matrix. The diagonal entries of the rectangular diagonal matrix are called singular values. The singular values (SVs) which are zero or close to zero indicate unidentifiable parameter deviations [21].

Meggiolaro et al. [22] propose an analytical method to determine the unidentifiable parameters. General cases of linear combinations between columns of the identification Jacobian are proposed. Moreover, the physical consequences of parameter deviations are considered, as well. These two steps result in an elimination of redundant errors and a non-singular regressor matrix. In [22] it is shown that the numerical methods are more time efficient.

An analysis of the sensitivity property of the regressor matrix leads to the so called observability indices which come from the optimal experimental design theory [23, 24]. Five indices, O_1 to O_5 , are used in the parameter identification, which have different relationships to the SVs of the regressor matrix and to the experimental design. For example, O_1 is related to the volume of a hyperellipsoid whose axes are the SVs representing the solution space. Maximising O_1 results in uniformly large axes and hence, a large influence on the parameter deviation sensitivity. O_4 is defined as the noise amplification index by

combining O_2 and O_3 . The index O_2 is the inverse condition number of the identification Jacobian. The index O_3 is defined as the smallest SV. Despite the name, maximising O_4 reduces the influence of noise and unmodelled errors.

Parameter identification methods which utilise orientation and position data have to use a scaled regressor matrix. As a consequence of different units, the SVs are not comparable. However, a task variable scaling allows comparability. An exception is a human-sized arm, where meters and radians are directly comparable. The observability index O_1 is invariant to scaling which makes it the optimal index for unscaled experiments [1, 23, 25].

The overall identification Jacobian is composed of N poses. Therefore, the sensitivity of the regressor matrix can be increased by choosing an optimal set of poses. Various approaches exist to improve the optimal set, e.g., Partial Swarm Optimisation [26], DETMAX [27], Generic Algorithm method [28]. A well-known algorithm is DETMAX which increases the D-optimality (equal to the index O_1) iteratively. At each iteration, two steps are carried out until a specified objective is reached, e.g., optimality threshold, number of iterations. First, the initial pose set of N poses is increased by one pose which increases the overall optimality of the set. Second, the set is reduced by one pose which decreases the overall optimality the least. DETMAX is used and extended by many researchers. For example, Daney et al. [29] improves the algorithm by adding a tabu search and using a second observability index.

In total there are three major steps to complete the identification process. Firstly, the unidentifiable parameters need to be excluded, secondly, a set of poses which are sensitive to parameter deviations are generated and thirdly, an optimisation problem is solved. Caenen et al. [30] incorporate linear stiffness coefficients of the joints into the identification process. The basis is the geometric parameters of the mDH convention. Adding linear stiffness leads to an improvement of the average absolute position from 2.82 mm to 0.58 mm of a six degree of freedom robot of cylindrical type by using only position data. It clearly states that adding joint compliance improves the absolute accuracy about 5%. However, the joint stiffness of robots is often far from linear and should be identified in a separate process. Nowadays, it is possible to conduct precise payload experiments due to significant improvements in the field of torque/force sensors.

Brom et al. [31] show that rating robot poses with an observability index, namely O_1 , to obtain an optimal set of measurements poses, can reduce the amount of poses needed to identify the parameters from the initial amount of 102 to 12 poses. The parameter set includes three translations and three rotations for all but the last axis. The last translation only consists of three translations due to the measurement constraints. They clearly show the usefulness of an observability index.

Nubiola et al. [28] identify non-geometric as well as geometric parameters to reduce the position error by half. Their method uses the identified mDH parameter, linear stiffness coefficients, and a Fourier series for the gear transmission of the sixth axis. In

the end, the cyclic error compensation of the sixth axis which was approximated with a Fourier series, was neglected due to minor influence on the accuracy.

In this work, the classical identification method is used as well as the improved DETMAX algorithm of Daney et al. [29].

1.1.4 Offline Trajectory Planning

The field of offline trajectory planning reaches from using polynomial/trigonometric functions to optimal control methods [1, 16]. Polynomial and trigonometric functions are the simplest form to plan robot trajectories. Parametrising trajectories with those functions has the drawback that constraints on angular rate, acceleration or other derivatives are not possible. However, initial and terminal conditions can be considered. Other common ways to parametrise trajectories are splines, radial basis functions [32] or the Sigmoid-function [33], where constraints of the position and of the corresponding derivatives can be incorporated. These techniques do not include a compensation of geometrical (e. g. imprecise DH values) and non-geometrical errors (e. g. joint elasticity).

In [34], an approach is proposed to compensate two types of errors which are relevant for the precise positioning of a robot. The first is a collection of errors of different sources, e. g. imprecise DH values, joint compliance, which are not covered by the work in [34]. The non-linear periodic behaviour of the gears constitutes the second term. The periodic error is approximated by a sum of sinusoids. The offline correction scheme subtracts the errors from the desired joint trajectories and uses the result to adjust the reference trajectory. This process reduces the vibrations of the joint positions caused by the periodic error from 0.15 mm to 0.09 mm. Olabi et al. [35] use a similar approach, but include the gear elasticity in addition which reduces the average error in the z -direction from 0.20 mm to 0.03 mm.

In [36], semivariograms are fitted to the position errors along each direction to pinpoint error similarities. A semivariogram represents the degree of error similarity between two points by an Euclidean distance. It is used to identify the essential bandwidth for the hidden layer of the proposed neural network (NN), especially for the used radial basis functions (RBFs). The RBF neural network consists of three layers, the input, the hidden, and the output layer. The input of the neural network are the joint positions and the output is the estimated error in each direction. The estimation is performed by a linear combination of RBFs at the hidden layer. Due to the identification of the bandwidths with semivariograms, only the weighting factors of the output layer have to be learned. The learning is carried out using the pseudo-inverse method, where a pseudo-inverse matrix made up of the hidden layer vectors multiplied with the position error determines the weighting factors. The sum of the estimated position error and the desired position is used as reference for the robot control unit. The proposed method reduces the mean position error from 1.36 mm to 0.11 mm.

Liu et al. [37] use the screw theory to model the kinematics and dynamics. A particle swarm optimization (PSO) algorithm is proposed to find the optimal angular trajectory

for each joint which minimises the synthesis error. The synthesis error is defined as the combination of the trajectory planning error caused by the trajectory interpolation and the dynamic error caused by elastic joints. It is shown that the error can be reduced by approximately 88.94 %.

Trajectory planning algorithms which incorporate optimal control problems (OPC), do have the advantage that not only constraints on derivatives are possible, but also a given performance index is optimised, e. g. shortest time, smallest amount of energy consumed. OCPs can be solved numerically by direct and indirect methods. Direct methods transform an infinite- to a finite-dimensional optimisation problem by discretisation of the time, whereas indirect methods convert the optimal control problem to a boundary-value problem. Techniques like collocation methods, single- and multiple-shooting are utilised for these steps. Direct multiple-shooting methods include the states and the control input as optimisation variables. This leads to a large Jacobian, but exhibits a sparse structure [38–40].

Gattringer et al. [41] calibrate the kinematic and dynamic model of a 6-DOF industrial robot. A full model for the kinematics is used and Coulomb and viscous friction is included. The calibration of the kinematic parameters increases the absolute accuracy for the position from double-digit to sub-millimeter values and for the orientation from single-digit to sub-degree values. A direct multiple-shooting method with a sequential quadratic programming is applied to determine a final calibrated trajectory with a balance between minimal time and minimal energy consumption. However, including additional joint effects into the dynamics of the robot, e. g. non-linear gear transmission, as well as an objective to minimise the pose error, could increase the accuracy further.

In summary, a compensation strategy for geometrical and non-geometrical errors has to combine a calibrated kinematic model [34, 35, 41–43], identified dynamic parameters [41, 43, 44] and additional effects like elastic joints and friction [34–37, 41, 43, 44]. Residual errors can be reduced by applying further techniques like ILC [43], yet leaving the area of offline planning. Therefore, in this work, a calibrated kinematic model, identified dynamic parameters, elastic joints and non-constant gear ratios are used to determine a highly accurate robot pose trajectory by solving an optimal control problem.

1.2 Aim and Overview of this Work

The repeatability of the provided industrial robot, a COMAU Racer-7-1.4, is specified with 0.03 mm^1 , whereas the absolute accuracy can range up to double-digit millimeter [1, Section 4.9] and thus still needs improvement. This work aims at enhancing the absolute accuracy of the COMAU robot by implementing three consecutive steps. Firstly, the non-constant gear transmission of the first, second and third gear are identified to compensate for vibrations at the end-effector of the robot. The identification includes a basic constant transmission and a Fourier series for the cyclic fraction. Secondly, the

¹<https://www.comau.com/en/our-competences/robotics/robot-team/racer7-14>, last visited on 01. Sep. 2020

actual mDH parameters are identified in a calibration procedure to compensate position errors due to inaccuracies during the manufacturing process. Prior to conducting such a calibration, the identifiable parameters have to be determined. Moreover, a set of poses is designed and used for the calibration which amplifies parameter uncertainties. The first two steps described so far are used to accurately model an industrial robot with elastic joints, where the elasticity of the gear transmission is assumed to be given.

The results gained by implementing step one and two can be used to calculate the desired trajectories of the motor angles for specified pose trajectories. The third step increases the absolute accuracy without a complex control scheme and additional sensors. The dynamic model is extended by elastic joints and non-constant gear ratios. The elasticity of the joints are determined in a previous work. An offline trajectory determination approach is introduced to generate motor angular acceleration trajectories based on the specified angular trajectories. The accurate extended robot model is used in the proposed method. The motor angular accelerations serve as input signals for the subordinate low-level control of the robot's motors. Therefore, effects like friction are handled by the low-level controllers. These trajectories lead to a high accuracy in the output domain.

The remainder of this work is structured as follows. The kinematic and dynamic model, extended with elastic joints, are presented in Chapter 2. Moreover, the identification of the gear transmission is formulated and the results are discussed. Prior to the identification of the mDH parameters, the actual identifiable parameters of the used setting are determined. Additionally, the best pose sets for the identification and verification phase are designed. Hence, the mDH parameter identification is carried out, discussed and verified in Chapter 3. The preceding results are used to generate accurate link angle trajectories from desired pose trajectories. Finally, the offline trajectory planning is defined as an optimal control problem which is solved for two pose reference trajectories in Chapter 4, followed by a discussion about the simulation results and possible future work in Chapter 5.

2 Modelling of Elastic Joint Robots

Kinematic and dynamic models can be used to describe and control the behaviour of a robot. Kinematic models consider the geometric relation without taking into account forces, whereas dynamic models describe the relation between forces and the resulting motion. The kinematics of serial manipulators are usually determined by applying the DH convention.

The dynamic model is determined by the Euler-Lagrange formalism. The formalism uses the Lagrange function, which is the difference between the kinetic and potential energy. The determination of said energies is straightforward, which is an advantage of the Euler-Lagrange formalism.

In this chapter, the kinematic and dynamic model of an elastic joint robot with non-constant gear ratio and non-linear joint stiffness is determined and explained in detail.

2.1 Kinematic Model

The Denavit-Hartenberg convention consists of four homogeneous transformations to describe the transformation from one to another joint frame. A homogeneous transformation $\mathbf{T} \in \text{SE}(3)$ is a 4×4 matrix given by

$$\mathbf{T} = \begin{bmatrix} \mathbf{R} & \mathbf{t} \\ \mathbf{0}_{1 \times 3} & 1 \end{bmatrix}, \quad (2.1)$$

with $\mathbf{R} \in \text{SO}(3)$ being a rotation matrix and $\mathbf{t} \in \mathbb{R}^3$ being a translation vector. The *special Euclidean group* $\text{SE}(n)$ of the order n is a subgroup of the group of affine transformations. The *special orthogonal group* $\text{SO}(n)$ of the order n consists of purely all orthogonal matrices, where the determinant equals one [45].

The convention describes the transformation between two frames, frame $i - 1$ and i , with only four parameters q_i , a_i , d_i and α_i , in a Cartesian coordinate system. The joint frames i are set up as follows (cf. [16]):

- The z_i -axis is set to be collinear to the rotation axis of joint $i + 1$, whereby the parameter q_i describes the rotation about the z_i -axis.
- The common normal between the z_{i-1} - and the z_i -axis is chosen as the x_i -axis.
- The angle between the z -axes about the x_i -axis is the parameter α_i .

- The distance along the z_{i-1} -axis between the origin of the frame $i-1$ and the x_i -axis is described by the parameter d_i .
- The origin of the i th frame is set at the intersection of the common normal and the z_i -axis, whereby the distance between the origin and the z_{i-1} -axis along the common normal is represented by the parameter a_i .
- The y_i -axis is chosen so that the frame is a right-handed one.

The base frame ($i = 0$) can be set almost freely. There is only one restriction, namely the rotation axis of the joint and the z_0 -axis are collinear.

These rules lead to the homogeneous transformation from frame $i-1$ to frame i

$$\mathbf{T}_{i-1}^i = \begin{bmatrix} \mathbf{R}_z(q_i) & \mathbf{0}_{3 \times 1} \\ \mathbf{0}_{1 \times 3} & 1 \end{bmatrix} \begin{bmatrix} \mathbf{0}_{3 \times 3} & \mathbf{t}_x(a_i) \\ \mathbf{0}_{1 \times 3} & 1 \end{bmatrix} \begin{bmatrix} \mathbf{0}_{3 \times 3} & \mathbf{t}_z(d_i) \\ \mathbf{0}_{1 \times 3} & 1 \end{bmatrix} \begin{bmatrix} \mathbf{R}_x(\alpha_i) & \mathbf{0}_{3 \times 1} \\ \mathbf{0}_{1 \times 3} & 1 \end{bmatrix}. \quad (2.2)$$

In the case of nearly parallel or parallel revolute joint axes, a common normal does not exist. Therefore, Hayati et al. [19] proposed an alternative step to define the origin of the frame i . The intersection of the z_i -axis with a perpendicular plane to the z_{i-1} -axis defines the origin. This alternative eliminates the parameter d_i , but introduces a necessary rotation around the y_i -axis. The mDH convention's homogeneous transformation reads as

$$\mathbf{H}_{i-1}^i = \begin{bmatrix} \mathbf{R}_z(q_i) & \mathbf{0}_{3 \times 1} \\ \mathbf{0}_{1 \times 3} & 1 \end{bmatrix} \begin{bmatrix} \mathbf{0}_{3 \times 3} & \mathbf{t}_x(a_i) \\ \mathbf{0}_{1 \times 3} & 1 \end{bmatrix} \begin{bmatrix} \mathbf{R}_x(\alpha_i) & \mathbf{0}_{3 \times 1} \\ \mathbf{0}_{1 \times 3} & 1 \end{bmatrix} \begin{bmatrix} \mathbf{R}_y(\beta_i) & \mathbf{0}_{3 \times 1} \\ \mathbf{0}_{1 \times 3} & 1 \end{bmatrix}. \quad (2.3)$$

The overall homogeneous transformation for the considered manipulator with six joints, visualised in Figure 2.1, reads as

$$\mathbf{T}_0^6 = \mathbf{T}_0^1 \mathbf{T}_1^2 \mathbf{H}_2^3 \mathbf{T}_3^4 \mathbf{T}_4^5 \mathbf{T}_5^6 = \begin{bmatrix} \mathbf{R}_e & \mathbf{p}_e \\ \mathbf{0}_{1 \times 3} & 1 \end{bmatrix}, \quad (2.4)$$

where $\mathbf{R}_e \in \text{SO}(3)$ is the orientation and $\mathbf{p}_e \in \mathbb{R}^3$ is the position of the end-effector - both expressed in the inertial frame $(0, x_0, y_0, z_0)$.

2.2 Dynamic System

The considered robot, COMAU Racer-7-1.4, has six degrees of freedoms (DOFs) as can be seen in the schematics of Figure 2.1. All joints are revolute. In this work, the motors and links have an elastic connection, which is why the joint and the motor angles and angular rates are independent states. This results in the generalised coordinates $\boldsymbol{\xi} \in \mathbb{R}^{12}$, which are the six angles associated to the joint q_i and to the motor θ_i : $\boldsymbol{\xi} = [\xi_1, \xi_2, \dots, \xi_{12}]^T = [q_1, q_2, \dots, q_6, \theta_1, \dots, \theta_6]^T$.

A straightforward way to determine the equations of motion is the Euler-Lagrange formalism [1, Chapter 11]:

$$\frac{d}{dt} \frac{\partial L}{\partial \dot{\xi}_i} - \frac{\partial L}{\partial \xi_i} = \tau_i, \quad i = 1, \dots, 12, \quad (2.5)$$

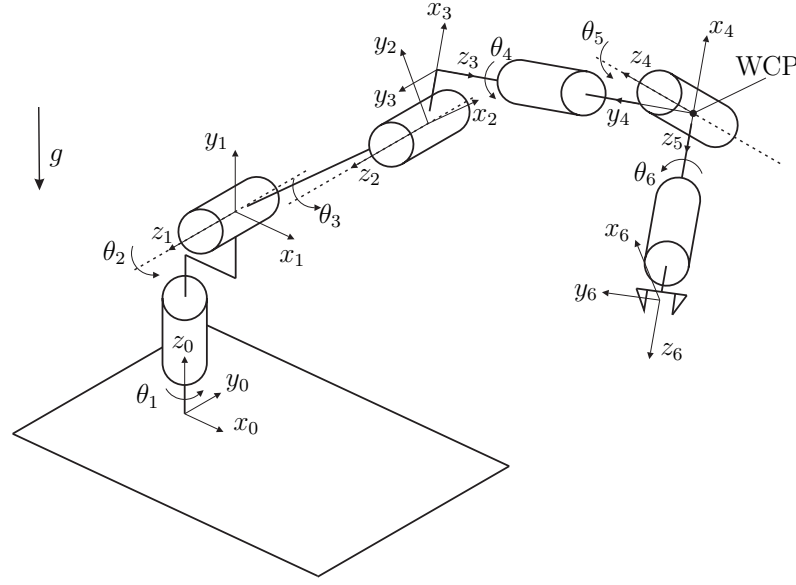


Figure 2.1: Schematic of the Robot COMAU Racer-7-1.4 [15]. In this work, q_i are the joint angles instead of θ_i . The wrist center point (WCP) is not used in this work, it is commonly used to separate the positioning and orientation task of the end-effector.

where τ_i are the generalised forces, $L = T - V$ is the Lagrange function, T is the kinetic energy, and V is the potential energy of the system.

For robots with rigid links, equation (2.5) can be reformulated in vector form [15]

$$\mathbf{D}(\boldsymbol{\xi})\ddot{\boldsymbol{\xi}} + \mathbf{C}(\boldsymbol{\xi}, \dot{\boldsymbol{\xi}})\dot{\boldsymbol{\xi}} + \mathbf{g}(\boldsymbol{\xi}) = \boldsymbol{\tau} , \quad (2.6)$$

with the symmetric positive definite mass matrix $\mathbf{D}(\boldsymbol{\xi}) \in \mathbb{R}^{12 \times 12}$, where $T = \frac{1}{2}\dot{\boldsymbol{\xi}}^T \mathbf{D}(\boldsymbol{\xi}) \dot{\boldsymbol{\xi}}$ holds, the centrifugal and Coriolis forces $\mathbf{C}(\boldsymbol{\xi}, \dot{\boldsymbol{\xi}})\dot{\boldsymbol{\xi}} \in \mathbb{R}^{12}$, the vector of potential forces $\mathbf{g}(\boldsymbol{\xi}) \in \mathbb{R}^{12}$ and the generalised force vector $\boldsymbol{\tau} = [\tau_1, \tau_2, \dots, \tau_{12}]^T$. The elements of the matrix \mathbf{C} can be described as

$$\mathbf{C}[k, j] = \sum_{i=1}^{12} c_{ijk} \dot{\xi}_i , \quad (2.7)$$

where c_{ijk} are the *Christoffel symbols* of the first kind. They are defined as

$$c_{ijk} = \frac{1}{2} \left(\frac{\partial d_{kj}}{\partial \xi_i} + \frac{\partial d_{ki}}{\partial \xi_j} - \frac{\partial d_{ij}}{\partial \xi_k} \right) , \quad (2.8)$$

where d_{ij} is the (ij) -element of the mass matrix \mathbf{D} , see [16, Chapter 7].

2.2.1 Non-Constant Gear Ratio

In this work, the non-constant gear ratio is approximated by the sum of a constant basic transmission and a Fourier series, cf. [9], and reads as

$$u(\varphi) = u_0 + \sum_{j=1}^{n_u} \hat{u}_j \cos(\tilde{u}_j \varphi + \bar{u}_j) , \quad (2.9)$$

with the output side angle of the gear φ , see Figure 2.2, the number of considered frequencies n_u , the basic transmission u_0 , the frequencies $\tilde{\mathbf{u}} = [\tilde{u}_1, \dots, \tilde{u}_{n_u}]$, the phase shifts $\bar{\mathbf{u}} = [\bar{u}_1, \dots, \bar{u}_{n_u}]$ and the amplitudes $\hat{\mathbf{u}} = [\hat{u}_1, \dots, \hat{u}_{n_u}]$. The gear ratio (2.9) can be written in the linear parametric form

$$u(\varphi) = u_0 + \sum_{j=1}^{n_u} \hat{a}_j \cos(\tilde{u}_j \varphi) - \hat{b}_j \sin(\tilde{u}_j \varphi) \quad (2.10a)$$

$$\text{with } \hat{a}_j = \hat{u}_j \cos(\bar{u}_j) \text{ and } \hat{b}_j = \hat{u}_j \sin(\bar{u}_j) . \quad (2.10b)$$

The angular rate relation due to the gear ratio is given by

$$\dot{\theta} = u(\varphi) \dot{\varphi} . \quad (2.11)$$

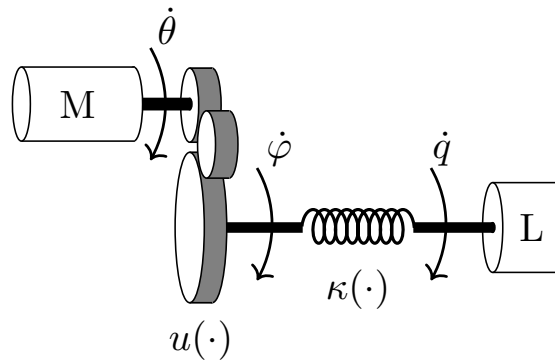


Figure 2.2: Motor M to link L connection representing an elasticity and a non-constant gear ratio.

The relation between the output side and motor side angle is determined by solving (2.11), using separation of variables with (2.10)

$$\int d\theta = \int u(\varphi) d\varphi , \quad (2.12)$$

which leads to

$$\Xi(\varphi) = \theta = u_0 \varphi + \sum_{j=1}^{n_u} \frac{1}{\tilde{u}_j} (\hat{a}_j \sin(\tilde{u}_j \varphi) + \hat{b}_j \cos(\tilde{u}_j \varphi)) + U_C(\theta_0, \varphi_0) , \quad (2.13)$$

with the constant of integration U_C as a function of the initial values $\theta_0 = \theta(0)$ and $\varphi_0 = \varphi(0)$. The constant of integration is

$$U_C(\theta_0, \varphi_0) = \theta_0 - u_0 \varphi_0 - \sum_{j=1}^{n_u} \frac{1}{\tilde{u}_j} (\hat{a}_j \sin(\tilde{u}_j \varphi_0) + \hat{b}_j \cos(\tilde{u}_j \varphi_0)) . \quad (2.14)$$

2.2.2 Kinetic and Potential Energy

The derivation of the kinetic and potential energy of serial chain manipulators with elastic joints are only shortly summarised in this section. For further details, please see [15]. The transformation of the inertia tensor from the link/mass-frame to the inertial frame is left aside for simplicity and readability, as well as the substitution of the angular and translational velocity by the joint angle velocities.

The kinetic energy of a serial manipulator with rigid links is given by

$$T = \frac{1}{2} \dot{\boldsymbol{\xi}}^T \mathbf{D}(\boldsymbol{\xi}) \dot{\boldsymbol{\xi}} = \sum_{i=1}^6 T_{L,i} + T_{M,i} , \quad (2.15)$$

where $T_{L,i}$ is the kinetic energy of the link i and $T_{M,i}$ is the kinetic energy of the motor i . Both kinetic energies consist of translational and rotational elements. Additionally, they are functions of the angular and translational velocities. The kinetic energy of a link L or motor M can be written as

$$T_{j,i} = \frac{1}{2} m_{j,i} \dot{\mathbf{c}}_{j,i}^T \dot{\mathbf{c}}_{j,i} + \frac{1}{2} \boldsymbol{\omega}_{j,i}^T \mathbf{I}_{j,i} \boldsymbol{\omega}_{j,i} , \quad j = M, L , \quad (2.16)$$

with the inertia tensor $\mathbf{I}_{j,i}$ with respect to its center of mass and transformed to the inertial frame. In (2.16), $\mathbf{c}_{j,i}$ denotes the vector to the center of mass, and $\boldsymbol{\omega}_{j,i}$ the angular velocity of the link or the motor, both expressed in the inertial frame. Hence, $\dot{\mathbf{c}}_{j,i}$ and $\boldsymbol{\omega}_{j,i}$ are functions of \mathbf{q} and $\dot{\mathbf{q}}$ and $\boldsymbol{\omega}_{M,i}$ is a function of \mathbf{q} , $\dot{\mathbf{q}}$, $\boldsymbol{\theta}$ and $\dot{\boldsymbol{\theta}}$.

The energy stored in the elastic joints with linear stiffness, using the output side angle $\varphi = \Xi^{-1}(\boldsymbol{\theta})$, can be written as

$$V_s = \frac{1}{2} (\mathbf{q} - \boldsymbol{\varphi})^T \mathbf{K}_s (\mathbf{q} - \boldsymbol{\varphi}) , \quad (2.17)$$

with the positive definite stiffness matrix $\mathbf{K}_s = \text{diag}([k_{s,1}, k_{s,2}, \dots, k_{s,6}])$ and $k_{s,i}$ being the linear stiffness coefficient. For the non-linear stiffness case the equation changes to

$$V_s = \sum_{i=1}^6 \int_0^{q_i - \varphi_i} \kappa_i(\alpha) d\alpha , \quad (2.18)$$

with the non-linear elastic torque $\kappa_i(\alpha)$ as a monotonically increasing function of the angle α , where $\kappa_i(0) = 0$ holds.

The potential energy due to gravity is given by

$$V_g = \sum_{i=1}^6 m_{L,i} \mathbf{g}_e^T \mathbf{c}_{L,i} + m_{M,i} \mathbf{g}_e^T \mathbf{c}_{M,i}, \quad (2.19)$$

with the gravity vector $\mathbf{g}_e = [0, 0, g]^T$. The sum $V = V_s + V_g$ gives the total potential energy. The partial derivative of the total energy with respect to the generalized coordinates gives the gravity component of the dynamic system model,

$$\mathbf{g}^T = \frac{\partial V}{\partial \boldsymbol{\xi}}. \quad (2.20)$$

2.2.3 Equations of Motion

In [15, (2.63)], it is demonstrated that the sum of (2.16) over $j = M, L$ and $i = 1, \dots, 6$ leads to the total kinetic energy of an elastic joint robot

$$T_E = \begin{bmatrix} \dot{\mathbf{q}} \\ \dot{\boldsymbol{\theta}} \end{bmatrix}^T \begin{bmatrix} \mathbf{D}_E(\mathbf{q}) & \mathbf{U}(\mathbf{q}) \\ \mathbf{U}(\mathbf{q})^T & \mathbf{D}_M \end{bmatrix} \begin{bmatrix} \dot{\mathbf{q}} \\ \dot{\boldsymbol{\theta}} \end{bmatrix}, \quad (2.21)$$

with the constant motor inertia diagonal matrix $\mathbf{D}_M \in \mathbb{R}^{6 \times 6}$, the positive definite mass matrix $\mathbf{D}_E \in \mathbb{R}^{6 \times 6}$ and the motor/link inertia couplings are considered in the upper triangle matrix $\mathbf{U}(\mathbf{q}) \in \mathbb{R}^{6 \times 6}$.

Hence, the equations of motion of a robot with elastic joints in the form of (2.6) and utilizing (2.21), (2.7), and (2.20) are given by

$$\underbrace{\begin{bmatrix} \mathbf{D}_E(\mathbf{q}) & \mathbf{U}(\mathbf{q}) \\ \mathbf{U}(\mathbf{q})^T & \mathbf{D}_M \end{bmatrix}}_{\mathbf{D}(\mathbf{q})} \underbrace{\begin{bmatrix} \ddot{\mathbf{q}} \\ \ddot{\boldsymbol{\theta}} \end{bmatrix}}_{\dot{\boldsymbol{\xi}}} + \underbrace{\begin{bmatrix} \mathbf{C}_E(\mathbf{q}, \dot{\mathbf{q}}) & \mathbf{C}_1(\mathbf{q}, \dot{\mathbf{q}}) \\ \mathbf{C}_2(\mathbf{q}, \dot{\mathbf{q}}) & 0 \end{bmatrix}}_{\mathbf{C}(\mathbf{q}, \dot{\mathbf{q}})} \underbrace{\begin{bmatrix} \dot{\mathbf{q}} \\ \dot{\boldsymbol{\theta}} \end{bmatrix}}_{\dot{\boldsymbol{\xi}}} + \underbrace{\begin{bmatrix} \mathbf{g}_L(\mathbf{q}) + \boldsymbol{\kappa}(\mathbf{q} - \boldsymbol{\varphi}) \\ -\boldsymbol{\kappa}(\mathbf{q} - \boldsymbol{\varphi}) \end{bmatrix}}_{\mathbf{g}(\boldsymbol{\xi})} + \underbrace{\begin{bmatrix} \boldsymbol{\tau}_{f,J}(\dot{\mathbf{q}}) \\ \boldsymbol{\tau}_{f,M}(\dot{\boldsymbol{\theta}}) \end{bmatrix}}_{\boldsymbol{\tau}_f(\dot{\boldsymbol{\xi}})} = \begin{bmatrix} \boldsymbol{\tau}_{ext} \\ \boldsymbol{\tau}_d \end{bmatrix}, \quad (2.22)$$

where $\boldsymbol{\tau}_f(\dot{\boldsymbol{\xi}}) \in \mathbb{R}^{12}$ describes the friction forces, $\boldsymbol{\tau}_{ext} \in \mathbb{R}^6$ are the generalised external forces and $\boldsymbol{\tau}_d \in \mathbb{R}^6$ is the vector of the generalised forces of the motors. In (2.22), $\mathbf{C}_1(\mathbf{q}, \dot{\mathbf{q}}) \in \mathbb{R}^{6 \times 6}$ and $\mathbf{C}_2(\mathbf{q}, \dot{\mathbf{q}}) \in \mathbb{R}^{6 \times 6}$ are the Coriolis matrices resulting from the motor/link inertia couplings.

Neglecting the motor/link inertia couplings yields $\mathbf{U}(\mathbf{q}) = \mathbf{0}$, $\mathbf{C}_1 = \mathbf{0}$, $\mathbf{C}_2 = \mathbf{0}$, and the simplified model reads as, cf. [15],

$$\mathbf{D}_E(\mathbf{q}) \ddot{\mathbf{q}} + \mathbf{C}_E(\mathbf{q}, \dot{\mathbf{q}}) \dot{\mathbf{q}} + \mathbf{g}_L(\mathbf{q}) + \boldsymbol{\tau}_{f,J}(\dot{\mathbf{q}}) = \boldsymbol{\kappa}(\mathbf{q} - \boldsymbol{\varphi}) + \boldsymbol{\tau}_{ext} \quad (2.23a)$$

$$\mathbf{D}_M \ddot{\boldsymbol{\theta}} + \boldsymbol{\tau}_{f,M}(\dot{\boldsymbol{\theta}}) = \boldsymbol{\tau}_d - \boldsymbol{\kappa}(\mathbf{q} - \boldsymbol{\varphi}). \quad (2.23b)$$

3 Parameter Identification

This chapter elaborates on the identification of the model parameters for the non-constant gear ratios and the forward kinematics. All other parameters of the model introduced in Chapter 2 are supposed to be known for this work. In Section 3.1, the focus lies on the gear ratio parameter identification, while in Section 3.2 the mDH parameters are determined. Each section closes with the presentation and discussion of the results.

3.1 Non-Constant Gear Ratio Parameters

In this work, the gear ratio consists of a constant basic value and a Fourier series, as shown in Section 2.2.1. The basic value and the Fourier parameters are determined in a three-step process. First, the measured data is processed. Second, the frequencies used in the Fourier series are determined by a FFT. Additionally, the direct neighbours of the identified main frequencies are taken into account to compensate for the imprecise identification. Third, the remaining Fourier parameters and the basic value are identified by minimising the quadratic error between the measured and calculated drive side angular rate.

The first three joints have the highest impact on the robot's accuracy. Hence, the non-constant gear ratios are only identified for the first, second and third axis. The parameters of gear four, five and six are not fully determined. Their influence on the pose error is not substantial. Therefore, only the basic value is identified side by side with the mDH parameters in Section 3.2 for those gears.

3.1.1 Identification Process

The kinematic error is the input of the identification process and it is composed of the difference of the measured and calculated link side angular rate of the gear [9]. The drive side angle is measured by an encoder, whereas the output side angular rate is measured by a gyroscope mounted on the related link of the gear. The drive side angular rate is determined by a numerical derivation of the measured drive side angle. The identification procedure is executed for each joint separately. Thereby, the full operational range of the specific joint is covered and the measurement is performed multiple times for each rotation direction with constant velocity.

Data Processing

The raw data of the applied sensors is not suitable for calculations, wherefore refinements are carried out before the estimation of the Fourier parameters and the basic value are

performed. The following two methods are applied to improve the measured output side angular rate:

1. Filtering with an acausal filter and
2. aligning to rotation axis.

The drive side angular rate is filtered with the same acausal filter as the output side angular rate to ensure that both signals have the same bandwidth.

Filtering: A discrete form of the acausal Gaussian filter, with the impulse response

$$v_G(t) = \frac{1}{\sigma_q \sqrt{2\pi}} \exp\left(-\frac{t^2}{2\sigma_q^2}\right), \quad (3.1)$$

is used to remove noise from the measurements, where σ_q is the standard deviation

$$\sigma_q = \frac{\sqrt{\ln(2)}}{2\pi f_c} \quad (3.2)$$

and f_c the 3dB-bandwidth frequency, see [46].

The 3dB-bandwidth frequency is chosen as a multiple of the base frequency, which is listed in Table A.4 for each gear.

Alignment to Rotation Axis: An alignment to the rotation axis is essential due to the inclined installation of the gyroscope. An optimal mounting of the sensor yield a non-zero result only for the rotation axis. Therefore, the unconstrained optimisation problem is solved to determine two rotation angles to align the angular rate data to the desired rotation axis.

$$\min_{\alpha, \beta} \left\| \sum_{k=0}^{N-1} r(t_k) \mathbf{e} - \mathbf{R}_i(\alpha) \mathbf{R}_j(\beta) \boldsymbol{\omega}_G(t_k) \right\|_2^2 \quad (3.3)$$

In (3.3), $t_k = t_0 + kT_s$, $k \in [0, N-1]$ is a discrete time step of the measurement, T_s is the sampling time, N is the number of measurement data points, \mathbf{e} is the orientation vector of the desired rotation axis, $r(t) = \|\boldsymbol{\omega}_G(t)\|_2$ is the magnitude of the measured angular rate of the gyroscope, $\boldsymbol{\omega}_G(t) = [\omega_{G,x}(t), \omega_{G,y}(t), \omega_{G,z}(t)]^T$ is the gyroscope data, $\mathbf{R}_i(\alpha)$ and $\mathbf{R}_j(\beta)$ are the rotation matrices about the axis $i, j \in [x, y, z]$, ($i \neq j$), with the rotation angles α and β .

Due to the alignment, only one component of $\mathbf{R}_i(\alpha^*) \mathbf{R}_j(\beta^*) \boldsymbol{\omega}_G(t_k) \in \mathbb{R}^3$ is non-zero and further referred to as $\omega_{G,fa}(t_k) \in \mathbb{R}$ or in vector form as $\boldsymbol{\omega}_{G,fa} = [\omega_{G,fa}(t_0), \dots, \omega_{G,fa}(t_{N-1})]$.

Gravity Impact

The angular rate of the axes two and three cannot be measured without the influence of gravity when the robot is installed as depicted in Figure 2.1. The gravity

torque $\boldsymbol{\tau}_g = [\tau_g(t_0), \tau_g(t_1), \dots, \tau_g(t_{N-1})]$ is calculated by the gravity component of the dynamic model, defined by (2.20) in Chapter 2, with the output side angle $\mathbf{q} = [q(t_0), q(t_1), \dots, q(t_{N-1})]$ at each time step $t_k = t_0 + kT_s$, $k \in [0, N - 1]$. The deflection $\Delta\boldsymbol{\varphi}_g = [\Delta\varphi_g(t_0), \Delta\varphi_g(t_1), \dots, \Delta\varphi_g(t_{N-1})]$ is looked up from the non-linear stiffness curve via $\boldsymbol{\tau}_g = [\tau_g(t_0), \tau_g(t_1), \dots, \tau_g(t_{N-1})]$ at each time step t_k . The non-linear stiffness curves are depicted in Appendix A.3. The angular rate variation due to the gravity $\Delta\dot{\boldsymbol{\varphi}}_g = [\Delta\dot{\varphi}_g(t_0), \Delta\dot{\varphi}_g(t_1), \dots, \Delta\dot{\varphi}_g(t_{N-1})]$ is determined by the time derivative of the deflection $\Delta\boldsymbol{\varphi}_g = [\Delta\varphi_g(t_0), \Delta\varphi_g(t_1), \dots, \Delta\varphi_g(t_{N-1})]$.

Kinematic Error

The kinematic error $\boldsymbol{\omega}_e = [\omega_e(t_0), \omega_e(t_1), \dots, \omega_e(t_{N-1})]$ is defined as the difference between the transmitted drive side angular rate $u_0\dot{\boldsymbol{\theta}}_f = u_0[\dot{\theta}_f(t_0), \dot{\theta}_f(t_1), \dots, \dot{\theta}_f(t_{N-1})]$, with the basic gear ratio u_0 , and the output side angular rate $\dot{\boldsymbol{\varphi}} = [\dot{\varphi}(t_0), \dot{\varphi}(t_1), \dots, \dot{\varphi}(t_{N-1})]$ of a gear at each time step t_k , see (3.4)

$$\boldsymbol{\omega}_e = u_0\dot{\boldsymbol{\theta}}_f - \dot{\boldsymbol{\varphi}}. \quad (3.4)$$

A typical time evolution of the error is depicted in Figure 1.2. The data processing sequence with all its actions to determine the kinematic error from measurement data is shown in Figure 3.1.

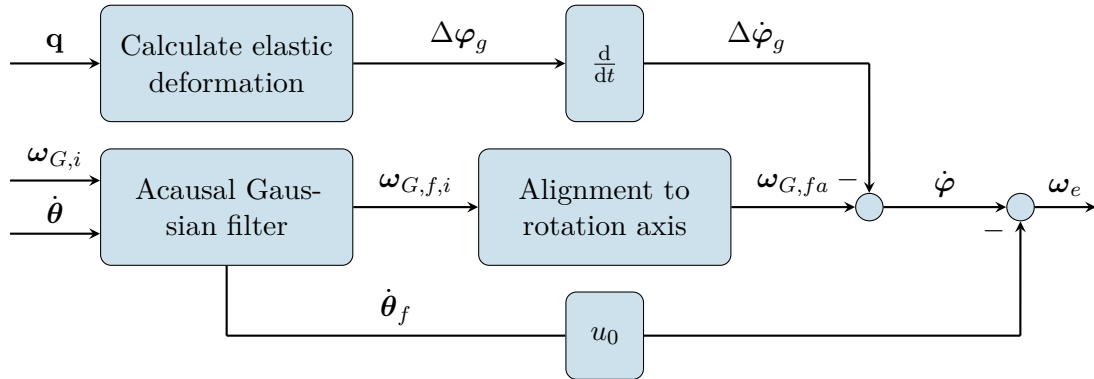


Figure 3.1: Data processing sequence to calculate the kinematic error $\boldsymbol{\omega}_e$, where $\boldsymbol{\omega}_{G,i} = [\omega_{G,i}(t_0) \dots \omega_{G,i}(t_{N-1})]^T$ with $i = [x, y, z]$ is the gyroscope data of the axis i and $\boldsymbol{\omega}_{G,fa}$ is one filtered rotation axis component $\boldsymbol{\omega}_{G,j}$, $j \in [x, y, z]$.

Frequency Analysis

A frequency analysis of the kinematic error $\boldsymbol{\omega}_e$ is conducted after the raw data is processed. Due to the mechanical joint limits a full turn is not possible to achieve. Hence, it is not possible to gain the required resolution for the FFT.

In this work, the FFT is used to perform a coarse search for the frequencies included in the kinematic error. The obtained results are extended by the direct neighbouring

frequencies of the identified main frequencies to cover floating point harmonics and to account for the imprecise identification.

Gear Ratio Parameter Identification

The non-constant gear ratio is determined for several cases. The verification of the identified parameter sets show that for each rotation direction a set of parameters is necessary to compensate for the kinematic error. This is mainly, due to the internal unmodelled effects like friction.

The parameters of the Fourier series $\hat{\mathbf{a}} = [\hat{a}_1, \dots, \hat{a}_{n_u}]$, $\hat{\mathbf{b}} = [\hat{b}_1, \dots, \hat{b}_{n_u}]$ and the basic ratio u_0 are identified by an unconstrained optimisation problem based on the angular rate relation (2.11). The optimisation problem for the gear ratio parameters reads as

$$\min_{\psi_t = [\hat{\mathbf{a}}, \hat{\mathbf{b}}, u_0]} \left\| \sum_{k=0}^{N-1} u(\theta_f(t_k), \psi_t) \dot{\theta}_f(t_k) - \dot{\varphi}(t_k) \right\|_2^2. \quad (3.5)$$

The frequencies $\tilde{\mathbf{u}}$ of the Fourier series (2.9) are determined in advance by the frequency analysis, see Section 3.1.1.

System Installation

The gyroscope used to measure the output side angular rate can be placed at any available mounting point on the robot. A clean cable installation is mandatory because any entanglement can influence the measurement. The sensor is fixed to the subsequent link of the gear that is intended to be measured, as depicted in Figure 3.2.

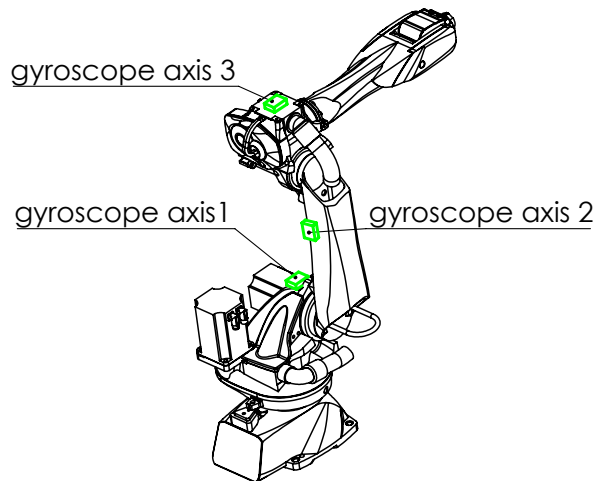


Figure 3.2: Gyroscope mounting places on the COMAU Racer-7-1.4.

The measurements of the kinematic error of gear one can be slightly affected by tilting effects due to gravity influence. This can be prevented by positioning the robot such that the tilting moment around the first axis is almost zero.

Experimental Procedure

The experiments are conducted as follows:

- The first three joints are measured separately.
- Each joint should optimally be free of external forces and torques, except for gravity.
- More than one rotation in the working range in each direction is measured, such that validation data is available.

Six rotations in the operational range in each direction are carried out to identify and validate the gear transmission parameters.

3.1.2 Results

The results of the identified gear transmissions are presented and discussed in this chapter. The actual identified values are listed in Appendix A.1.

The experiments with the COMAU Racer-7-1.4 show that one set of gear ratio parameters, identified with data of one rotational direction, does not compensate for the kinematic error in both directions. It can be concluded that the deviations between the results are caused by the gear effects mentioned in Section 1.1.1. The unmodelled effects such as friction, internal elasticity and backlash, are not in the scope of this work. Therefore, two sets of gear ratio parameters are identified, one for each rotational direction.

Gear 1

The output side angular rate is measured at a constant motor velocity of 7468 °/s (link side angular rate is ~ 88 °/s), which is 40 % of the maximal velocity. The physical boundaries of the joint at the link side are $\pm 165^\circ$, which results in a range of 330° . The acceleration reduces the practically usable range with constant velocity to 220° at the link side.

Alignment of the gyroscope data: The misalignment of the gyroscope emerges from the single mounting hole on the first link on the robot. The rotation angles to align the z -axis are determined by (3.3) and the results are $\alpha^* = 2.3401 \cdot 10^{-2}$ rad and $\beta^* = -1.0019 \cdot 10^{-2}$ rad. The identified angles α^* and β^* are used by subsequent rotations about the x -axis ($\mathbf{R}_x(\alpha^*)$) and y -axis ($\mathbf{R}_y(\beta^*)$), respectively. An alignment improves the orientation of the rotation axis, as shown in Table 3.1.

	before, in $^{\circ}/s$	after, in $^{\circ}/s$
x -axis	-0.88	$-8.40 \cdot 10^{-4}$
y -axis	2.05	-0.01
z -axis	-88.03	-88.06

Table 3.1: Comparison of the mean gyroscope data in each direction before the alignment of the rotation axis and after the alignment for a counter-clockwise (CCW) rotation of the first gear.

Frequency Analysis: The motion range of 220° allows an extraction of a periodic range of 180° to identify the frequencies. The dominant frequencies derived from the kinematic error using FFT are 84, 101, 202 and 303 1° , see Figure 3.3. The number of frequencies are extended to include the direct neighbouring values of the derived frequencies, see Table A.6 and Table A.9.

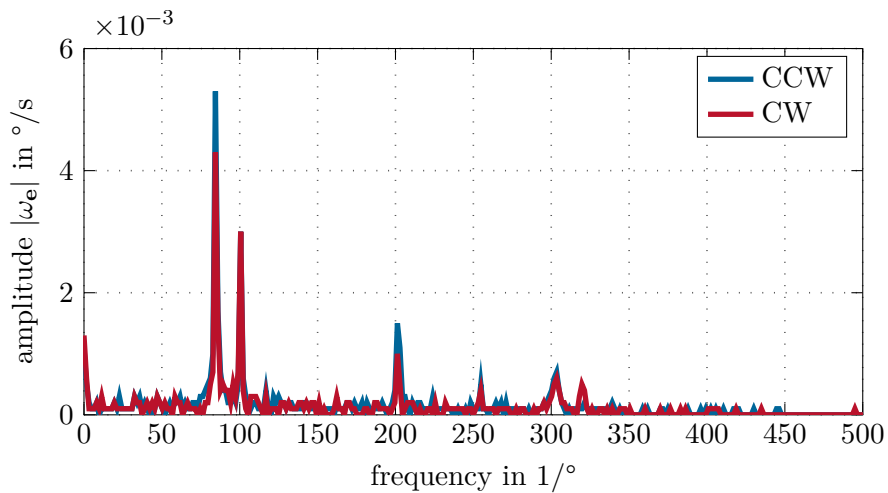


Figure 3.3: Fast Fourier Transform (FFT) result of the kinematic error of the first gear of a clockwise (CW) rotation (in red) and a counter-clockwise (CCW) rotation (in blue). The constant motor angular rate was $7468^{\circ}/s$ (link side angular rate is $\sim 88^{\circ}/s$).

Fourier Series Parameters: The identified Fourier parameters of clockwise rotation for the gear ratio computed by (3.5) are listed in Table A.6. The parameters of the counter-clockwise rotation for the gear ratio are listed in Table A.9. The identified basic gear ratio u_0 is 84.80. The identification is conducted as shown in Section 3.1.1.

The determined Fourier parameters are verified by additional measurements at the same motion range and speed. A verification at a speed of $3734^{\circ}/s$, which is approximately 20% of the maximal velocity, is conducted, see Figure 3.5. A reduction of the RMS value of the kinematic error from $1.3079 \cdot 10^{-1}^{\circ}/s$ to $6.0316 \cdot 10^{-2}^{\circ}/s$ is possible. The RMS

value of the kinematic errors for a speed of $7468^\circ/\text{s}$ are listed in Table 3.2. It is shown that the error can be reduced by approximately 72%. The original kinematic error and the one using the identified parameters are depicted in Figure 3.4.

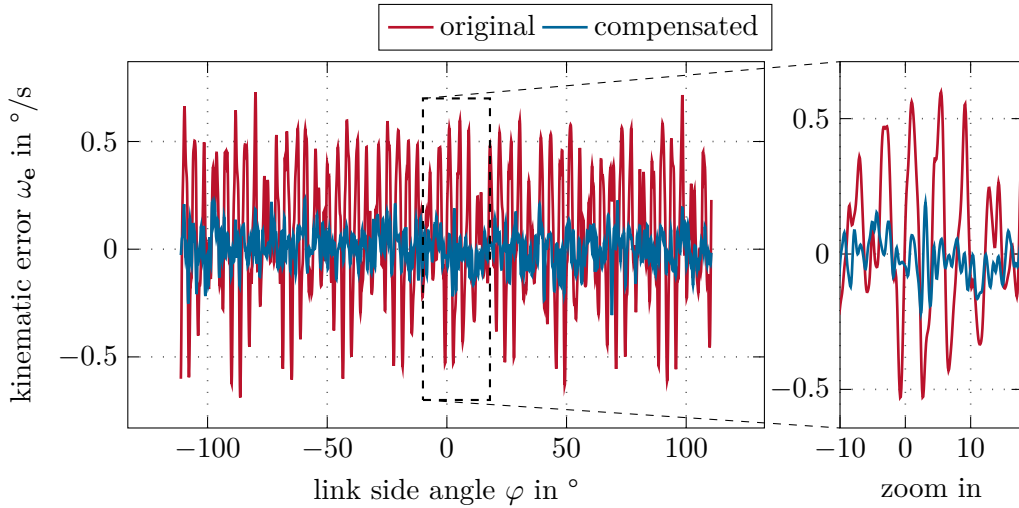


Figure 3.4: Comparison of the kinematic error of the first gear previous to the compensation (in red) and after the compensation (in blue) at a motor speed of $7468^\circ/\text{s}$ (link side speed is $\sim 88^\circ/\text{s}$).

used for	Rotation Direction	RMS before, in $^\circ/\text{s}$	RMS after, in $^\circ/\text{s}$
identification	CW	$2.6317 \cdot 10^{-1}$	$8.1959 \cdot 10^{-2}$
identification	CCW	$3.0028 \cdot 10^{-1}$	$7.4551 \cdot 10^{-2}$
validation	CW	$2.5876 \cdot 10^{-1}$	$7.9136 \cdot 10^{-2}$
validation	CCW	$2.9898 \cdot 10^{-1}$	$7.4148 \cdot 10^{-2}$

Table 3.2: The RMS values of the kinematic error of the first gear before and after the compensation of different measurements.

Gear 2

The output side angular rate is measured at a constant motor velocity of $8300^\circ/\text{s}$ (link side angular rate is $\sim 100^\circ/\text{s}$), which is 40% of the maximal velocity. The physical boundaries of the joint at the link side are -85° to 155° , which results in a range of 240° . The acceleration reduces the practically usable range with constant velocity to 100° at the link side. The alignment of the gyroscope data is performed as described in Section 3.1.2.

Frequency Analysis: The motion range of the link rotation of 100° allows an extraction of a periodic range of 90° to identify the frequencies. The dominant frequencies derived from the kinematic error using FFT are 83, 167 and 333 1/° , see Figure 3.6. The number

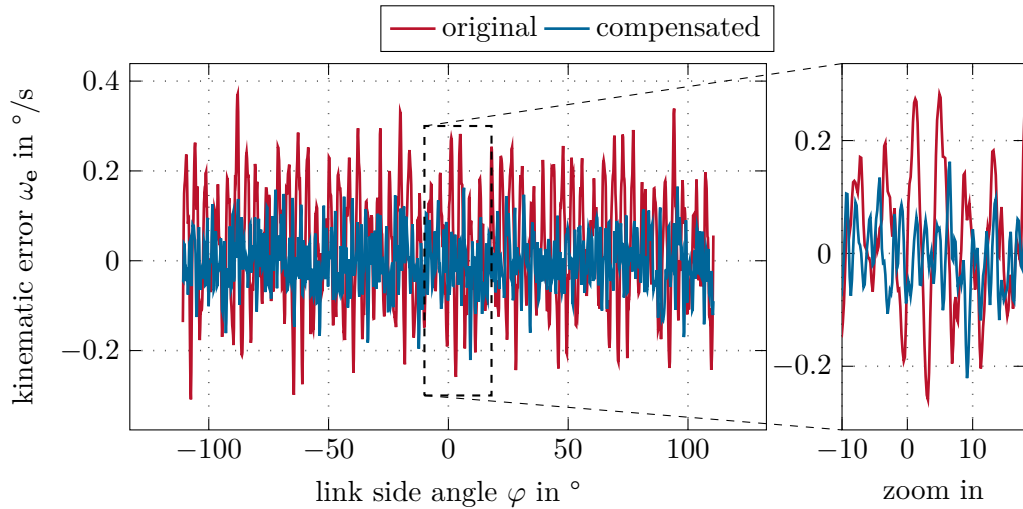


Figure 3.5: Comparison of the kinematic error of the first gear before the compensation (in red) and after the compensation (in blue) at a motor speed of $3734\text{ }^\circ/\text{s}$ (link side speed is $\sim 44\text{ }^\circ/\text{s}$) which is $\sim 20\%$ of the maximal velocity.

of frequencies are extended to include the direct neighbouring values of the derived frequencies, see Table A.7 and Table A.10.

Fourier Series Parameters: The identified Fourier parameters of clockwise rotation for the gear ratio computed by (3.5) are listed in Table A.7. The parameters of the counter-clockwise rotation for the gear ratio are listed in Table A.10. The identified basic gear ratio u_0 is 82.84. The identification is performed as shown in Section 3.1.1.

The determined Fourier parameters are verified by additional measurements at the same speed and motion range. A validation at a lower speed, 30% of the maximal speed, shows a reduction of the RMS value of the kinematic error from $1.6539 \cdot 10^{-1}\text{ }^\circ/\text{s}$ to $7.7654 \cdot 10^{-2}\text{ }^\circ/\text{s}$. The RMS values of the kinematic errors are listed in Table 3.3. It is shown that the error can be reduced by approximately 70%. The kinematic error and its compensated version are depicted in Figure 3.7.

used for	Rotation Direction	RMS before, in $^\circ/\text{s}$	RMS afterwards, in $^\circ/\text{s}$
identification	CW	$2.4382 \cdot 10^{-1}$	$5.9218 \cdot 10^{-2}$
identification	CCW	$2.2296 \cdot 10^{-1}$	$1.0445 \cdot 10^{-1}$
validation	CW	$2.6049 \cdot 10^{-1}$	$7.4176 \cdot 10^{-2}$
validation	CCW	$2.1404 \cdot 10^{-1}$	$9.7815 \cdot 10^{-2}$

Table 3.3: The RMS values of the kinematic error previous to and after the compensation of different measurements.

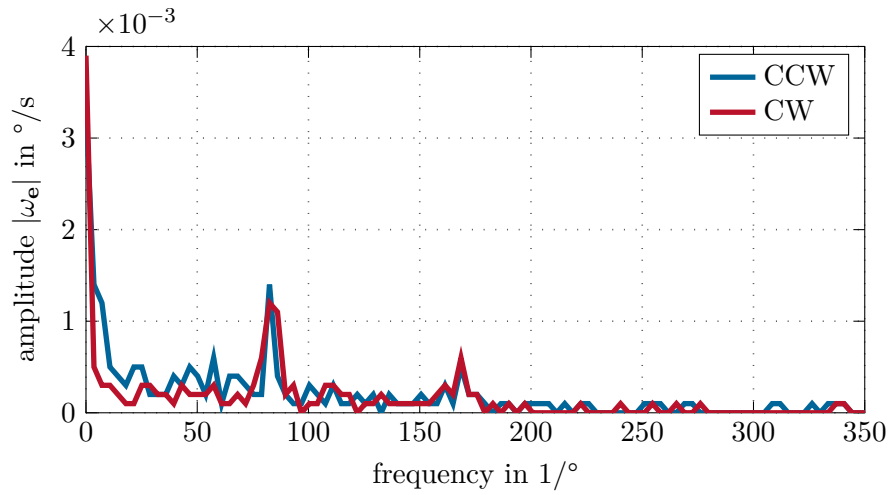


Figure 3.6: Fast Fourier Transform result of the kinematic error of the second gear of a clockwise (CW) rotation (in red) and a counter-clockwise (CCW) rotation (in blue). The constant motor angular rate was $8300\text{ }^\circ/\text{s}$ (link side angular rate is $\sim 100\text{ }^\circ/\text{s}$).

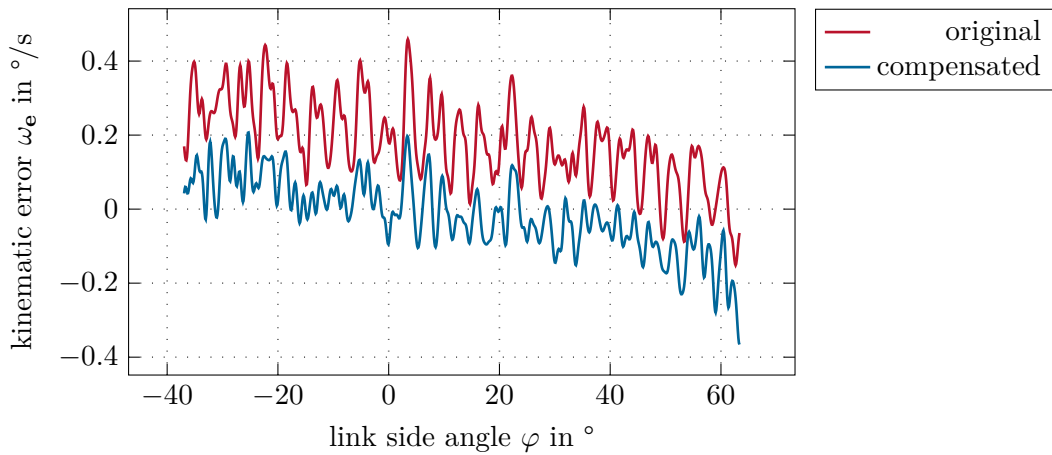


Figure 3.7: Comparison of the kinematic error of the second gear before the compensation (in red) and after the compensation (in blue) at a motor speed of $8300\text{ }^\circ/\text{s}$ (link side speed is $\sim 100\text{ }^\circ/\text{s}$).

Gear 3

The output side angular rate, the drive side angle and angular rate of the third gear is measured at a constant motor velocity of $4192^\circ/\text{s}$ (link side angular rate is $\sim 61^\circ/\text{s}$), which is 20% of the maximal velocity. The physical boundaries of the joint at the link side are -170° to 0° , which results in a range of 170° . The acceleration reduces the practically usable range with constant velocity to 53.49° at the link side. The alignment of the gyroscope data is performed as described in Section 3.1.2.

Frequency Analysis: The motion range of 53.49° does not allow to extract a periodic range to identify the frequencies. The dominant frequencies derived from the kinematic error using FFT are 70, 140 and $280\text{ }1/^\circ$, see Figure 3.8. The number of frequencies are extended to include the direct neighbouring values of the derived frequencies, see Table A.8 and Table A.11.

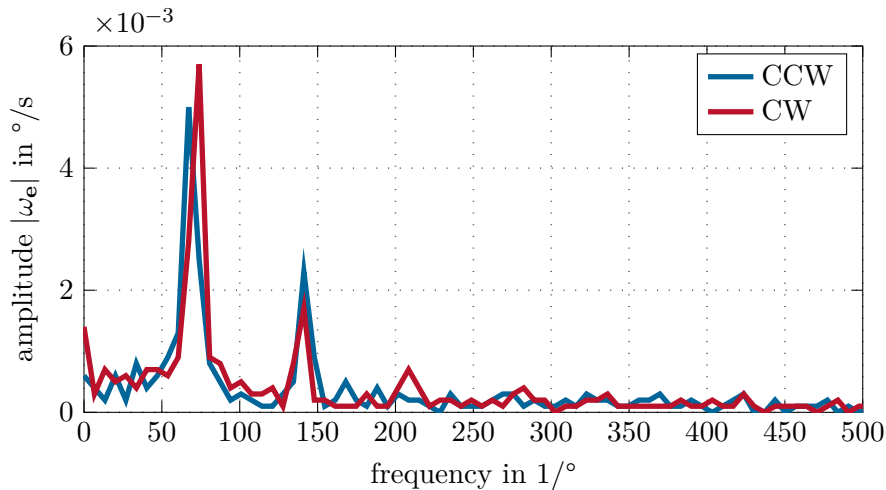


Figure 3.8: Fast Fourier Transform result of the kinematic error of a clockwise (CW) rotation (in red) and a counter-clockwise (CCW) rotation (in blue). The constant motor angular rate was $4192^\circ/\text{s}$ (link side angular rate is $\sim 61^\circ/\text{s}$).

Fourier Series Parameters: The identified Fourier parameters of clockwise rotation for the gear ratio computed by (3.5) are listed in Table A.8. The parameters of the counter-clockwise rotation are listed in Table A.11. The identified basic gear ratio u_0 is 69.05. The identification is performed as shown in Section 3.1.1.

The determined Fourier parameters are verified by additional measurements at the same speed and motion range. Due to the small motion range a validation with another speed is not conducted. The RMS value of the kinematic errors are listed in Table 3.4. It is shown that the error can be reduced by approximately 70%. The kinematic error and its compensated version are depicted in Figure 3.9.

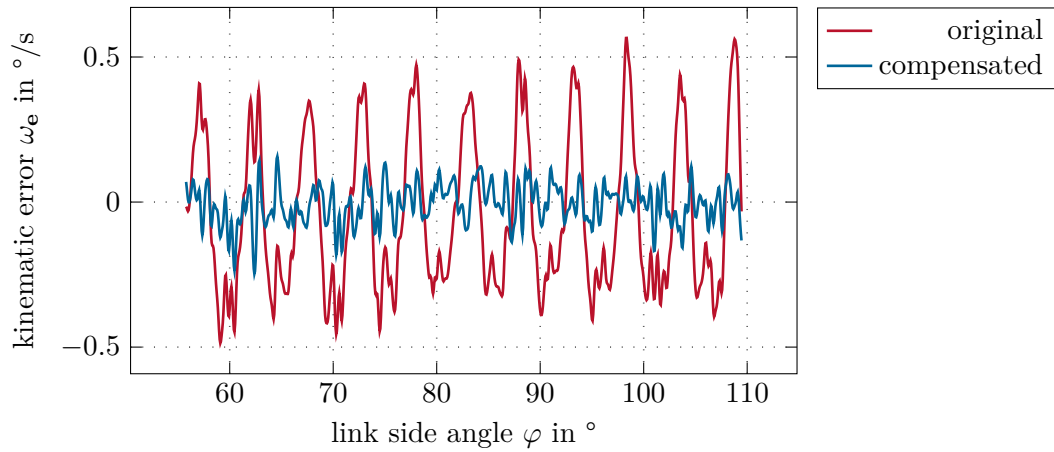


Figure 3.9: Comparison of the kinematic error previous to the compensation (in red) and after the compensation (in blue) at a motor speed of $4.19 \cdot 10^3$ °/s (link side speed ~ 61 °/s).

used for	Rotation Direction	RMS before, in °/s	RMS afterwards, in °/s
identification	CW	$2.7386 \cdot 10^{-1}$	$6.6944 \cdot 10^{-2}$
identification	CCW	$3.1313 \cdot 10^{-1}$	$8.1778 \cdot 10^{-2}$
validation	CW	$2.7282 \cdot 10^{-1}$	$6.6862 \cdot 10^{-2}$
validation	CCW	$3.0412 \cdot 10^{-1}$	$9.1894 \cdot 10^{-2}$

Table 3.4: The RMS values of the kinematic error before and after the compensation of different measurements.

3.2 Kinematic Model Parameters

The parameters of the kinematic model introduced in Section 2.1 are identified in three steps in this work. Firstly, the identifiable parameters are determined by an analysis of the robot's structure and a singular value decomposition (SVD) of the identification Jacobian [21]. Secondly, the extended DETMAX algorithm introduced by Daney et al. in [29] is used to calculate sets of optimal robot poses for the identification and verification phase. Thirdly, the identifiable parameters are determined by the classic identification process.

As mentioned in Section 3.1, the basic gear ratios of the fourth, fifth and sixth gear are added to the parameter set.

3.2.1 Identifiable Parameters

The kinematic model presented in Section 2.1 comprises 24 parameters. However, not all of them are identifiable due to the used measurement method and due to the dependency amongst each other, cf. [20]. The measurements are taken by an optical 6D tracking system called OptiTrack, which consists of 12 cameras and 6 reflecting markers mounted on the robot's end-effector. In small measurement areas or by using a large number of cameras (> 20), the accuracy of the system is about¹ 0.10 mm [47] and 0.05° according to the specifications of the cameras. The position of an object is calculated by the mean of the positions of all reflectors mounted on the tracking target. A set of reflectors is labelled as one rigid body. The orientation is calculated by the position difference of the reflectors. A high accuracy for the orientation is achieved with large distances between the reflectors. In this work, the original OptiTrack rigid body², with six reflectors mounted in small distances, is used. Since the COMAU Racer-7-1.4 as the considered obstacle for the calibration process of the sensor system, the large measurement area and the small rigid bodies entail that the accuracy of the orientation data is not precise enough and only the position data is usable.

The limitation to the position data leads automatically to a non-identifiable parameter α_6 , which could be identifiable with orientation data. The remaining identifiable parameters are determined by analysing the structure of the robot and the identification Jacobian \mathbf{J}_I .

The structure of the robot shows that the z_5 - and z_6 -axis are collinear, wherefore the translation parameters d_5 or d_6 are linear dependent and not identifiable.

The introduced Hayati-Parameter β_i is identifiable at one of the parallel rotation axes, but prevents the identification of the translation d_i along the z -axis. In conclusion, β_3 is identifiable, but d_3 is not. The parameters β_i ($i = 1, 2, 4, 5, 6$) are not part of the kinematic model, as described in Section 2.1.

¹<https://optitrack.com/applications/robotics/>, last visited on 01. Sept. 2020

²<https://optitrack.com/accessories/markers/#mcp1090>, last visited on 01. Sept. 2020

As mentioned in Section 1.1.3, the identification Jacobian \mathbf{J}_I is the partial derivative of the forward kinematics with respect to the mDH-parameters at the current joint position and a singular \mathbf{J}_I indicates the presence of non-identifiable parameters. The position deviation $\Delta \mathbf{p}_e$ reads as

$$\Delta \mathbf{p}_e = \mathbf{p}_{e,m} - \mathbf{p}_e(\mathbf{q}, \boldsymbol{\zeta}), \quad (3.6)$$

with $\mathbf{p}_{e,m}$ as the measured position of the OptiTrack system and $\mathbf{p}_e(\mathbf{q}, \boldsymbol{\zeta})$ of (2.4) being the nominal position of the end-effector. Note that $\mathbf{p}_e(\mathbf{q}, \boldsymbol{\zeta})$ is a function of the mDH parameters $\boldsymbol{\zeta} = [\zeta_1, \zeta_2, \dots, \zeta_{24}]^T = [\boldsymbol{\alpha}^T, \boldsymbol{\beta}^T, \mathbf{a}^T, \mathbf{d}^T]^T$, with $\boldsymbol{\alpha}$, $\boldsymbol{\beta}$, \mathbf{a} , and \mathbf{d} being the vectorized mDH-parameters of all axes, and the link angles $\mathbf{q} = [q_1, q_2, \dots, q_6]^T$. It is assumed that the deviation is small, which allows a Taylor series approximation of first order

$$\Delta \mathbf{p}_e = \frac{\partial \mathbf{p}_e}{\partial \boldsymbol{\alpha}} \Delta \boldsymbol{\alpha} + \frac{\partial \mathbf{p}_e}{\partial \boldsymbol{\beta}} \Delta \boldsymbol{\beta} + \frac{\partial \mathbf{p}_e}{\partial \mathbf{d}} \Delta \mathbf{d} + \frac{\partial \mathbf{p}_e}{\partial \mathbf{a}} \Delta \mathbf{a} + \frac{\partial \mathbf{p}_e}{\partial \mathbf{q}} \Delta \mathbf{q}, \quad (3.7)$$

with $\Delta \boldsymbol{\alpha}$, $\Delta \boldsymbol{\beta}$, $\Delta \mathbf{a}$, and $\Delta \mathbf{d}$ being the parameter deviations between the real and the nominal values and $\Delta \mathbf{q}$ is the deviation from the joint angles. If the measurement data includes the orientation, \mathbf{p}_e is replaced in (3.7) by the pose information including the position and the orientation data.

Introducing the identification Jacobian $\mathbf{J}_I = \left[\frac{\partial \mathbf{p}_e}{\partial \boldsymbol{\alpha}}, \frac{\partial \mathbf{p}_e}{\partial \boldsymbol{\beta}}, \frac{\partial \mathbf{p}_e}{\partial \mathbf{a}}, \frac{\partial \mathbf{p}_e}{\partial \mathbf{d}}, \frac{\partial \mathbf{p}_e}{\partial \mathbf{q}} \right]$, the approximation is rewritten as

$$\Delta \mathbf{p}_e = \mathbf{J}_I \Delta \mathbf{v}, \quad (3.8)$$

where $\Delta \mathbf{v}$ is the vector of all deviations $\Delta \boldsymbol{\alpha}$, $\Delta \boldsymbol{\beta}$, $\Delta \mathbf{a}$, $\Delta \mathbf{d}$, and $\Delta \mathbf{q}$. After excluding the above mentioned non-identifiable parameters, \mathbf{J}_I is calculated for K random pose configurations with the nominal parameters and combined to one matrix. The number of poses K is chosen randomly but has to be greater than the number of parameters. In this work, $K = 1000$.

The singular value decomposition reads as

$$\bar{\mathbf{J}}_I^T = [\mathbf{J}_{I,1}^T \mathbf{J}_{I,2}^T \dots \mathbf{J}_{I,M}^T]^T = \mathbf{U} \mathbf{S} \mathbf{V}^T, \quad (3.9)$$

with the stacked identification Jacobian $\bar{\mathbf{J}}_I$ ($n \times m$, $n = 30$ and $m = 3K$), the $m \times m$ unitary matrix \mathbf{U} , the $m \times n$ rectangular diagonal matrix with non-negative real numbers on the diagonal $\mathbf{S} = \text{diag}(\sigma_1, \sigma_2, \dots, \sigma_m)$ and \mathbf{V} being an $n \times n$ unitary matrix. Here, σ_i is called singular value. The MATLAB function `svd()` is used to determine the matrices. If the singular value $\sigma_i \cong 0$ then the parameter ζ_i or q_i is not identifiable.

In this work, the goal is to identify the constant gear ratios $u_{0,i}$ of the axis 4, 5 and 6. The joint angles $\mathbf{q} = \mathbf{q}(\boldsymbol{\varphi}, \boldsymbol{\kappa})$ are a function of the link side angles of the gear $\boldsymbol{\varphi}$ and the non-linear stiffness $\boldsymbol{\kappa}$ of the gear. The link side angle reads as $\boldsymbol{\varphi} = \mathbf{u}_0 \boldsymbol{\theta}$ for the constant gear ratio \mathbf{u}_0 and $\boldsymbol{\theta}$ is the motor side angle. Therefore, the identifiability of the deviation of the joint angles $\Delta \mathbf{q}$ is used as an indication for the identifiability of the constant gear ratio \mathbf{u}_0 .

The resulting identifiable and non-identifiable parameters are listed in Table 3.5 and the finally used parameters are $\check{\mathbf{v}} = [d_2, d_4, d_5, a_1, \dots, a_5, \alpha_1, \dots, \alpha_5, \beta_3, u_{0,4}, u_{0,5}, u_{0,6}] \in \mathbb{R}^{17}$.

Frame j	d_j	a_j	α_j	β_j	q_j	Frame j	d_j	a_j	α_j	β_j	q_j
1	n	i	i	x	i	4	i	i	i	x	i
2	i	i	i	x	i	5	i	i	i	x	i
3	n	i	i	i	i	6	n	n	n	x	i

Table 3.5: A list of identifiable mDH parameters of the COMAU Racer-7-1.4 with position measurements (i: identifiable, n: not identifiable, x: not existing).

3.2.2 Set of Identification Poses

The sensitivity of the identification Jacobian \mathbf{J}_I to parameter deviations is used to find the identifiable parameters. This characteristic is further exploited in determining K robot configurations for the calibration in this section, with

$$\check{\mathbf{J}}_I^T = [\check{\mathbf{J}}_{I,1}^T, \dots, \check{\mathbf{J}}_{I,K}^T]^T, \quad \check{\mathbf{J}}_{I,i} = \frac{\partial \mathbf{p}_e(\mathbf{q}_i, \mathbf{v})}{\partial \check{\mathbf{v}}}, \quad i = 1, \dots, K,$$

where \mathbf{q}_i is the i th robot configuration, \mathbf{v} is the vector of all mDH parameters and $\check{\mathbf{v}}$ is the vector of all identifiable mDH parameters, see Section 3.2.

The extended DETMAX algorithm, introduced in [29], is executed to determine $K = 50$ robot configurations for the parameter identification and 13 for validation. The goal of the algorithm is to increase the observability indices of the set. In this work the indices

$$O_1 = \frac{\sqrt[m]{\prod_{i=1}^m \sigma_i}}{\sqrt{K}} \quad (3.10)$$

and

$$O_4 = \frac{(\min \boldsymbol{\sigma})^2}{\max \boldsymbol{\sigma}} \quad (3.11)$$

are used, with the vector of all singular values $\boldsymbol{\sigma} = [\sigma_1, \sigma_2, \dots, \sigma_m]$, where m is the number of identifiable parameters $\check{\mathbf{v}} \in \mathbb{R}^m$.

The extended DETMAX algorithm starts with a full initialised set containing $K = 50$ random configurations and has two main parts. In the first part, 10 configurations are randomly chosen with the constraint to increase the index O_1 of the set. The one new configuration that maximises the index O_4 of the original set the most is added to the set. The second part removes one configuration from the set that has the least influence on index O_1 , to return to the desired amount of configurations. These two steps are repeated as long as the change in the observability index from one iteration to the next is above a given threshold.

The randomly chosen configurations are constraint by the axes' limits, given in Table A.1, and the workspace. The workspace is limited by the robot settings and the used sensor system. The workspace setting of the COMAU Racer-7-1.4 restricts the z -position above zero ($z \geq 0$), as can be seen in Figure 3.11. The cameras of the OptiTrack system cover the full robot workspace as depicted in Figure 3.10.

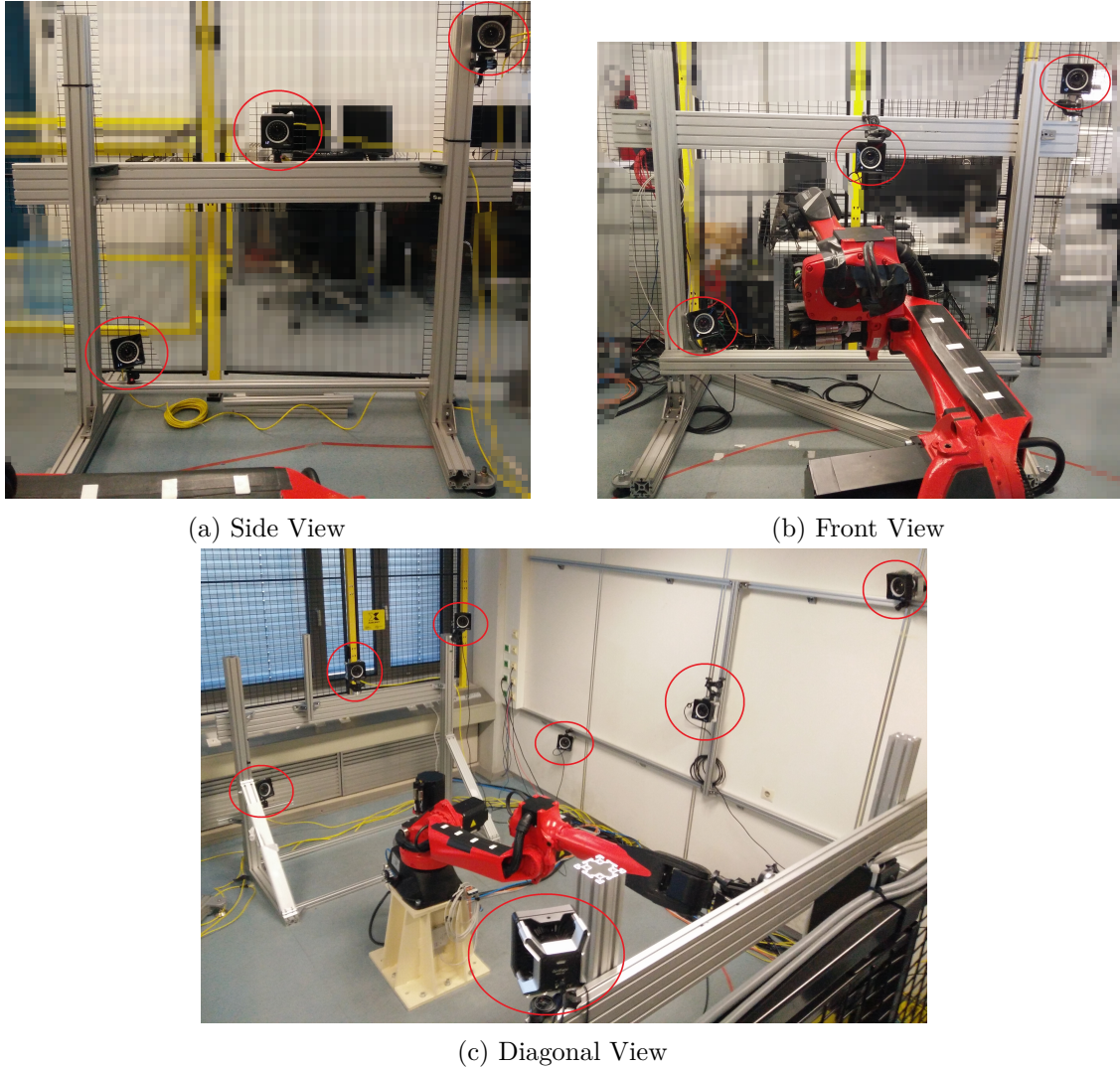


Figure 3.10: Installation of the sensor system and the robot COMAU Racer-7-1.4.

The resulting robot poses used for the identification process are listed in Table A.13 and Table A.14 and depicted in Figure 3.11. Thereby, each end-effector position is marked as yellow dot.

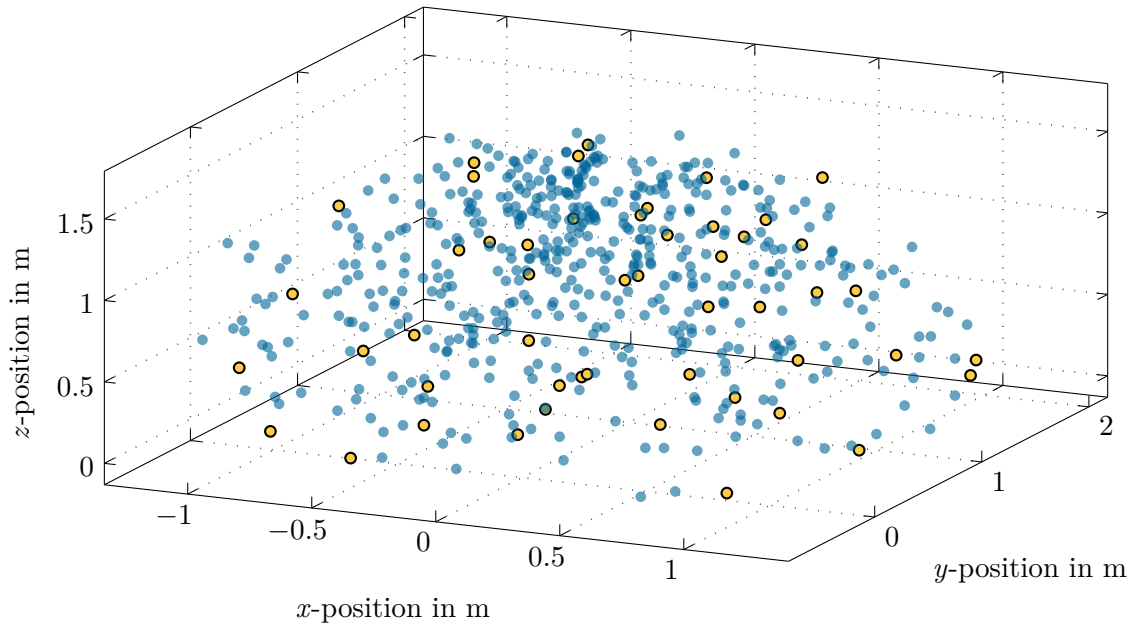


Figure 3.11: Positions of the end-effector for the determined pose set with the DETMAX algorithm are drawn as yellow dots with black border. The blue dots indicate random possible end-effector positions to get an idea about the workspace of the robot.

3.2.3 Classical Identification

The identification of the parameters is performed by minimising the quadratic difference between the nominal position from (2.4) and the measured position, hence called classical identification [20]. The COMAU Racer-7-1.4 consists of 20 independent and identifiable kinematic parameters $\check{\alpha}$, $\check{\beta}$, $\check{\mathbf{a}}$, $\check{\mathbf{d}}$, and $\check{\mathbf{u}}_0$, as shown in Table 3.5. They are collected in the vector $\check{\mathbf{v}} \in \mathbb{R}^{17}$, except the known basic gear ratios $u_{0,1}$, $u_{0,2}$, and $u_{0,3}$, see Section 3.1. The unconstrained optimisation problem reads as

$$\min_{\check{\mathbf{v}}=[\check{\alpha}, \check{\beta}, \check{\mathbf{a}}, \check{\mathbf{d}}, u_{0,4}, u_{0,5}, u_{0,6}]} \sum_{i=1}^M \|\mathbf{p}_e(\check{\mathbf{v}}, \mathbf{q}_i) - \mathbf{p}_{e,m}\|_2^2. \quad (3.12)$$

The nominal position \mathbf{p}_e is determined with the set of configurations $\boldsymbol{\theta}$ listed in Table A.13 and Table A.14. The set contains the motor angles $\boldsymbol{\theta}$, which have to be translated to the link side \mathbf{q} . Firstly, the inverted gear ratio is used to translate the motor angle to the link side, $\varphi_i = \Xi^{-1}(\theta_i)$ for $i = 1, 2, 3$ and $\varphi_i = \theta_i/u_{0,i}$ for $i = 4, 5, 6$. Secondly, the influence of the gravity is added $\mathbf{q} = \boldsymbol{\varphi} + \Delta\boldsymbol{\varphi}_g$, as described in Section 3.1.1. After the transformation from the motor to the link side, the nominal position is calculated by the direct kinematics (2.4).

3.2.4 Results

The identification procedure introduced in this work improves the absolute accuracy significantly. The extended classical identification has proven valid and accurate.

The maximum and mean position errors can be reduced by 81 % and the minimal errors by 67 % of the calibration set, see Table 3.6. The validation is performed using 13 robot pose configurations, which are different to the ones used for the identification. The validation shows similar results, which proves the accuracy of the proposed identification algorithm, see Table 3.7 and Figure 3.12.

The mDH-parameter deviations from the nominal values are listed in Table 3.8. These small deviations increase the absolute accuracy, as can be seen by the Euclidean distance from the nominal to the measured and optimised position depicted in Figure 3.12.

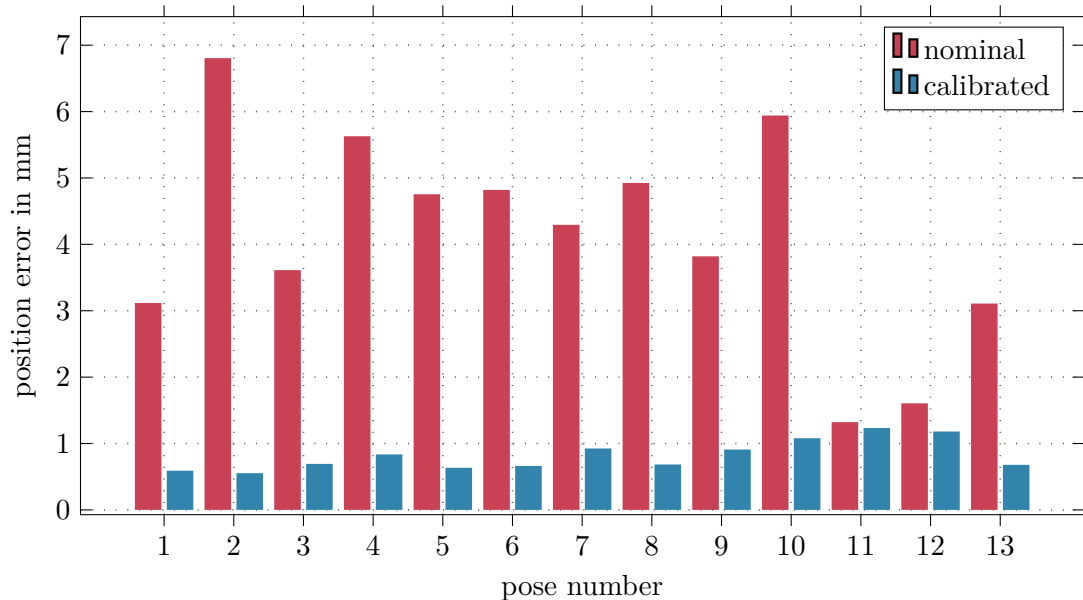


Figure 3.12: Euclidian distance from the nominal to the measured position of the end-effector of the validation configuration set in red and blue, respectively.

	before	after
max error in m	$6.9350 \cdot 10^{-3}$	$1.3277 \cdot 10^{-3}$
min error in m	$2.3018 \cdot 10^{-4}$	$7.6606 \cdot 10^{-5}$
mean error in m	$3.1659 \cdot 10^{-3}$	$6.1685 \cdot 10^{-4}$
standard deviation in m	$2.0244 \cdot 10^{-3}$	$2.6849 \cdot 10^{-4}$

Table 3.6: Position errors of the optimisation set before and after the calibration, in meter.

	before	after
max error in m	$6.8050 \cdot 10^{-3}$	$1.2332 \cdot 10^{-3}$
min error in m	$1.3222 \cdot 10^{-3}$	$5.5309 \cdot 10^{-4}$
mean error in m	$4.1348 \cdot 10^{-3}$	$8.1988 \cdot 10^{-4}$
standard deviation in m	$1.6045 \cdot 10^{-3}$	$2.2836 \cdot 10^{-4}$

Table 3.7: Position errors of the validation set before and after the calibration, in meter.

Frame j	Δd_j in m	Δa_j in m	$\Delta \alpha_j$ in rad	$\Delta \beta_j$ in rad	$u_{0,j}$
1	x	$-1.3453 \cdot 10^{-4}$	$-2.6899 \cdot 10^{-4}$	x	x
2	$7.7391 \cdot 10^{-5}$	$-6.3955 \cdot 10^{-4}$	$3.3536 \cdot 10^{-4}$	x	x
3	x	$-1.4147 \cdot 10^{-4}$	$9.2909 \cdot 10^{-5}$	$8.4190 \cdot 10^{-4}$	x
4	$-1.9136 \cdot 10^{-4}$	$-9.2677 \cdot 10^{-5}$	$-3.9434 \cdot 10^{-4}$	x	51.4232
5	x	$4.9013 \cdot 10^{-4}$	$2.7095 \cdot 10^{-5}$	x	46.0081
6	x	x	x	x	49.9998

Table 3.8: A list of identified mDH parameter deviations and the basic gear transmission ratios of gear 4, 5 and 6 of the COMAU Racer-7-1.4. The basic gear transmission ratios of gear 1 to 3 are identified in Section 3.1.

4 Offline Trajectory Planning

The goal of this chapter is to determine optimal control inputs for the robot to achieve highly accurate trajectories of the robot's pose. For this, the detailed models of the robot's kinematics and dynamics, described in the previous chapters, are used. The robot is equipped with high bandwidth velocity controllers for each axis. Hence, the angular acceleration of the motors is chosen as control input for the offline trajectory planning and the friction of the drive chains can be neglected.

The inverse kinematics is used to transform the two times continuously differentiable reference trajectory in the output space to the joint space. An optimal control approach is applied to determine optimal motor accelerations for a reference trajectory in the joint space.

The influence of the weighting factor which is used in the cost functional of the optimal control problem (OCP) is discussed in this chapter. Highlighting the differences in the results of the OCP with a detailed model and the OCP with a simple model is not part of this work. A verification of the offline trajectory planning on a real robot, which would show the differences between those two approaches, is the goal of future work.

In this work, a conical spiral and a straight line are chosen to demonstrate the presented algorithm. The desired orientation of the end-effector is constant and given. The identified parameters are used from Chapter 3 and the dynamic parameters of the links and motors from [15], see Section 2.2.2.

4.1 Optimal Control Problem

In this section, an optimal control problem is formulated to realize high-accuracy trajectory tracking. The goal is to determine optimal motor accelerations such that the joint coordinates follow a reference trajectory with minimal deviations. Therefore, the dynamic model including the non-constant gear ratios and the non-linear joint elasticities, as introduced in Chapter 2, is used.

The angular velocity $\dot{\theta}$ must be continuous to ensure finite acceleration and torques. Therefore, the control input \mathbf{u} of the dynamic system is chosen to be the motor acceleration $\ddot{\theta}$. An integration of the control input $\int \mathbf{u} dt = \dot{\theta}_{ref}$ induces the reference trajectory for the velocity controllers of the axes.

The simplified dynamic system (2.23) is used for the optimal control problem. Thereby, the joint friction $\tau_{f,J}$ is neglected and set to zero and the external forces τ_{ext} are assumed

to be zero. The dynamics of the motors as given in (2.23b) is not required because the motor acceleration $\ddot{\theta}$ is used as control input instead of the motor torque τ_d .

The states of the resulting system (2.23a) are given by $\mathbf{x} = [\mathbf{q}^T, \dot{\mathbf{q}}^T, \boldsymbol{\theta}^T, \dot{\boldsymbol{\theta}}^T]^T$. Hence, the dynamic system for the optimal control problem reads as

$$\dot{\mathbf{x}} = \frac{d}{dt} \begin{bmatrix} \mathbf{q} \\ \dot{\mathbf{q}} \\ \boldsymbol{\theta} \\ \dot{\boldsymbol{\theta}} \end{bmatrix} = \begin{bmatrix} \dot{\mathbf{q}} \\ \mathbf{D}_E^{-1}(\mathbf{q})(\boldsymbol{\kappa}(\boldsymbol{\Xi}^{-1}(\boldsymbol{\theta}) - \mathbf{q}) - \mathbf{g}_L(\mathbf{q}) - \mathbf{C}_E(\mathbf{q}, \dot{\mathbf{q}})\dot{\mathbf{q}}) \\ \dot{\boldsymbol{\theta}} \\ \mathbf{u} = \ddot{\boldsymbol{\theta}} \end{bmatrix} = \mathbf{f}(\mathbf{x}, \mathbf{u}) \quad (4.1)$$

with $\boldsymbol{\Xi}(\cdot)$ being the gear ratio function defined in (2.13), $\boldsymbol{\kappa}(\cdot)$ being the non-linear joint elasticity defined in Section 2.2.2, $\mathbf{D}_E(\mathbf{q})$ is the mass matrix, $\mathbf{g}_L(\mathbf{q})$ represents the gravitation forces, and $\mathbf{C}_E(\mathbf{q}, \dot{\mathbf{q}})\dot{\mathbf{q}}$ are the Coriolis and centrifugal forces.

As shown in Section 3.1.1, the identified non-constant gear ratio varies in each rotation direction. It is assumed that this behaviour is caused by unmodelled gear effects. Friction, wear, backlash and inner gear elasticity can introduce non-linear phase shift and non-linear amplitude behaviour [7]. Therefore, the gear ratio function used within the dynamic system equation is only used with parameters of the clockwise rotation.

The objective function of the optimal control problem is chosen as the difference between the reference and the actual link angle to improve the absolute accuracy. Additionally, a quadratic term for the control input with a weighting factor is added to the cost functional to be able to limit the bandwidth of the control input. The optimal control problem is formulated as

$$\min_{\mathbf{u}(\cdot), \mathbf{x}(\cdot)} \int_{t_0}^{t_e} \left(\|\mathbf{q}(t) - \mathbf{q}_d(t)\|_2^2 + \nu \|\mathbf{u}(t)\|_2^2 \right) dt \quad (4.2a)$$

$$\text{s.t. } \dot{\mathbf{x}} = \mathbf{f}(\mathbf{x}(t), \mathbf{u}(t)) \quad (4.2b)$$

$$\mathbf{x}_{min} \leq \mathbf{x}(t) \leq \mathbf{x}_{max}, \quad \forall t \in [t_0, t_e] \quad (4.2c)$$

$$\mathbf{u}_{min} \leq \mathbf{u}(t) \leq \mathbf{u}_{max}, \quad \forall t \in [t_0, t_e] \quad (4.2d)$$

$$\mathbf{q}(t_0) = \mathbf{q}_d(t_0), \quad \mathbf{q}(t_e) = \mathbf{q}_d(t_e) \quad (4.2e)$$

$$\boldsymbol{\theta}(t_0) = \boldsymbol{\Xi}(\mathbf{q}(t_0) - \boldsymbol{\kappa}^{-1}(\mathbf{g}(\mathbf{q}(t_0)))) \quad (4.2f)$$

$$\boldsymbol{\theta}(t_e) = \boldsymbol{\Xi}(\mathbf{q}(t_e) - \boldsymbol{\kappa}^{-1}(\mathbf{g}(\mathbf{q}(t_e)))) \quad (4.2g)$$

$$\dot{\mathbf{q}}(t_0) = \dot{\mathbf{q}}(t_e) = \mathbf{0} \quad (4.2h)$$

$$\dot{\boldsymbol{\theta}}(t_0) = \dot{\boldsymbol{\theta}}(t_e) = \mathbf{0} \quad (4.2i)$$

$$\mathbf{u}(t_0) = \mathbf{u}(t_e) = \mathbf{0}, \quad (4.2j)$$

with \mathbf{x}_{min} and \mathbf{x}_{max} being the upper and lower limits of each axis for the system states (angular position, angular rate), see Table A.1 and A.2, \mathbf{u}_{min} and \mathbf{u}_{max} being the upper and lower limits of the motor accelerations, see Table A.3, the initial $\dot{\mathbf{q}}(t_0)$ and terminal $\dot{\mathbf{q}}(t_e)$ link angular rate and the initial state $\dot{\boldsymbol{\theta}}(t_0)$ and terminal state $\dot{\boldsymbol{\theta}}(t_e)$ of the motor angular rate, $\mathbf{u}(t_0)$ and $\mathbf{u}(t_e)$ being the initial and the terminal motor acceleration and

$\nu > 0$ is a weighting factor. The initial and terminal state of the motor angle $\boldsymbol{\theta}$ in (4.2f) and (4.2g) ensure that the initial and terminal conditions of the dynamic system are fulfilled.

A direct multiple shooting method is used to solve the optimal control problem. Direct methods reduce optimal control problems to static non-linear programming problems (NLPs) [38, 39].

The multiple shooting method has two significant steps in the conversion. Firstly, the time span $t = [t_0, t_e]$ is split into N equidistant segments $T_s = (t_e - t_0)/(N - 1)$, wherefore the state $x_k = \mathbf{x}(t_k)$ and control input $u_k = \mathbf{u}(t_k)$ at each time step $t_k = t_0 + kT_s$ are treated as optimisation variables. Secondly, the ordinary differential equations (ODEs) representing the dynamics of the system are approximated by a discretisation method, e. g. Euler or Runge-Kutta method [39].

An approximation with the Runge-Kutta scheme introduces oscillations to the system because the dynamics of the industrial robot are described by stiff ODEs due to the elastic joints. Therefore, the trapezoidal method is used in this work. This leads to the transcribed NLP

$$\min_{\mathbf{y}} \sum_{k=0}^{N-1} \|\mathbf{q}_k - \mathbf{q}_{d,k}\|_2^2 + \nu \|\mathbf{u}_k\|_2^2 \quad (4.3a)$$

$$\text{s.t. } \mathbf{x}_{k+1} = \mathbf{x}_k + \frac{T_s}{2}(\mathbf{f}_k + \mathbf{f}_{k+1}), \quad \mathbf{f}_k = \mathbf{f}(\mathbf{x}_k, \mathbf{u}_k), \quad (4.3b)$$

$$\mathbf{x}_{min} \leq \mathbf{x}_k \leq \mathbf{x}_{max}, \quad \forall k = 1, 2, \dots, N-1 \quad (4.3c)$$

$$\mathbf{u}_{min} \leq \mathbf{u}_k \leq \mathbf{u}_{max}, \quad \forall k = 1, 2, \dots, N-1 \quad (4.3d)$$

$$\mathbf{q}_0 = \mathbf{q}_{d,0}, \mathbf{q}_{N-1} = \mathbf{q}_{d,N-1} \quad (4.3e)$$

$$\boldsymbol{\theta}_0 = \boldsymbol{\Xi}(\mathbf{q}_0 - \kappa^{-1}(\mathbf{g}(\mathbf{q}_0))) \quad (4.3f)$$

$$\boldsymbol{\theta}_{N-1} = \boldsymbol{\Xi}(\mathbf{q}_{N-1} - \kappa^{-1}(\mathbf{g}(\mathbf{q}_{N-1}))) \quad (4.3g)$$

$$\dot{\mathbf{q}}_0 = \dot{\mathbf{q}}_{N-1} = \mathbf{0} \quad (4.3h)$$

$$\dot{\boldsymbol{\theta}}_0 = \dot{\boldsymbol{\theta}}_{N-1} = \mathbf{0} \quad (4.3i)$$

$$\mathbf{u}_0 = \mathbf{u}_{N-1} = \mathbf{0}, \quad (4.3j)$$

with the optimisation variables $\mathbf{y} = [\mathbf{u}_0, \mathbf{x}_0, \mathbf{u}_1, \mathbf{x}_1, \dots, \mathbf{u}_{N-1}, \mathbf{x}_{N-1}]^T$. Moreover, $\dot{\mathbf{q}}_1$, $\dot{\mathbf{q}}_{N-1}$, $\boldsymbol{\theta}_1^{(i)}$ and $\boldsymbol{\theta}_{N-1}^{(i)}$ are the initial and terminal states of the link and motor angular rate ($i = 1$) and angular acceleration ($i = 2$), $\mathbf{q}_k = [q_{k,1}, \dots, q_{k,6}]^T$ and $\mathbf{u}_k = [u_{k,1}, \dots, u_{k,6}]^T$ are the link angles and the control input at time step k and $\mathbf{q}_{d,k} = [q_{d,k,1}, \dots, q_{d,k,6}]^T$ are the desired link angles at time step k .

The NLP (4.3) can be solved with the software tools CasADi, and IPOPT. CasADi is an open-source tool that generates derivative information using algorithmic differentiation. It supports ODE/DAE integration, sensitivity analysis and interfaces to numerical tools, such as the Interior Point Optimizer (IPOPT). The IPOPT is an open-source

package for large-scale non-linear optimisation. IPOPT performs an interior point line search filter method that aims to find a local solution of the NLP.

The implementation of (4.3) is carried out with CasADi [48] and IPOPT [49], using the solver MA27 [50]. The NLP is defined symbolically with CasADi syntax and solved with the combination of IPOPT and MA27.

4.2 Generation of Reference Trajectories

In this section, an algorithm is proposed to generate smooth end-effector position trajectories and a numerical inverse kinematic method is employed to determine the link side angles. The output is used as a reference for the optimal control problem proposed in Section 4.1.

4.2.1 Polynomial Trajectory Planning

The trajectory planning is a huge research field with various established algorithms [16, Chapter 4]. In this work, the variation in time of the desired position $\mathbf{p}_d(t) = [p_{d,x}(\lambda_x(t)) \ p_{d,y}(\lambda_y(t)) \ p_{d,z}(\lambda_z(t))]^T$ in the Euclidean space is parametrized by a 7th order polynomial, which reads as

$$\lambda(t) = \sum_{i=0}^7 \hat{m}_i t^i, \quad (4.4)$$

with the polynomial coefficients \hat{m}_i . The advantage of the polynomial approach is the simplicity and the possibility to include initial and terminal constraints. The order of seven is chosen because of the smoothness up to the second derivative, i. e. the acceleration. Polynomials of higher order are often used to generate suitable trajectories [1].

Here, the requirements for the robot's end-effector motion are zero velocity and acceleration at the start and at the end of the trajectory, in addition to the continuous differentiability up to order two. The initial and terminal conditions are achievable by setting the polynomial coefficients \hat{m}_i accordingly. They can be determined by solving (4.4) for the initial $\lambda(t_0)$ and terminal conditions $\lambda(t_e)$ and its first and second time derivative, $\dot{\lambda}(t_0) = \dot{\lambda}(t_e) = 0$ and $\ddot{\lambda}(t_0) = \ddot{\lambda}(t_e) = 0$, respectively. The results are

$$\begin{aligned} \hat{m}_0 &= \lambda(t_0), & \hat{m}_1 &= 0, & \hat{m}_2 &= 0, \\ \hat{m}_3 &= 0, & \hat{m}_4 &= -35 \frac{\Delta\lambda}{t_e^4}, & \hat{m}_5 &= 84 \frac{\Delta\lambda}{t_e^5}, \\ \hat{m}_6 &= -70 \frac{\Delta\lambda}{t_e^6}, & \hat{m}_7 &= 20 \frac{\Delta\lambda}{t_e^7}, \end{aligned}$$

with $\Delta\lambda = \lambda(t_e) - \lambda(t_0)$.

4.2.2 Numeric Inverse Kinematics

The reference trajectory in the output space has to be transformed to the joint space using the inverse kinematics. In [15], an analytic expression of the inverse kinematics of the con-

sidered robot is introduced. However, only the classical DH-parameters are used. Hence, the inverse kinematics problem is solved by a numerical approach [1, Chapter 2.7], such that the accurate model parameters from Chapter 3 can be used. A constraint optimisation problem is formulated to minimise the difference between the reference angles and the optimised angles. The joint angles $\mathbf{q}_0(t) = [q_{0,1}(t), q_{0,2}(t), q_{0,3}(t), q_{0,4}(t), q_{0,5}(t), q_{0,6}(t)]^T$ are determined by the analytic inverse kinematics of [15] and are used as initial value.

The constraint optimisation problem is solved for every time instant $k = 1, \dots, N$ and reads as [16]

$$\min_{\mathbf{q}_k} (\mathbf{q}_k - \mathbf{q}_{0,k})^T (\mathbf{q}_k - \mathbf{q}_{0,k}) \quad (4.5a)$$

$$\text{s.t. } \mathbf{p}_{d,k} = \mathbf{p}_e(\mathbf{q}_k) \quad (4.5b)$$

$$\mathbf{I}_{3 \times 3} = \mathbf{R}_{d,k}^{-1} \mathbf{R}_e(\mathbf{q}_k) \quad (4.5c)$$

with $\mathbf{I}_{3 \times 3}$ being the identity matrix of size 3×3 and $\mathbf{p}_e(\mathbf{q}_k)$ and $\mathbf{R}_e(\mathbf{q}_k)$ the position and orientation of the end-effector at the time step t_k calculated by the forward kinematics (2.4) incorporating the identified mDH-parameters.

The calculated desired link angles $\mathbf{q}_{d,k}$ result in a more accurate performance due to the precisely identified model parameters used in the inverse kinematics. The results of this section are used in Section 4.1, where the dynamics of the system including elastic joints and non-constant gear ratios on the trajectory are covered by an optimal control scheme.

4.3 Trajectory Examples

In this section, two different end-effector trajectories are used to verify the proposed offline trajectory planning method. The position and orientation accuracy are examined as well as the influence of the weighting factor ν on the accuracy and on the necessary controller bandwidth. The reference joint angles are determined as given in (4.5).

The desired orientation of the end-effector \mathbf{R}_d is calculated by the forward kinematics (2.4) with the nominal mDH parameters for the link angles $q_1 = q_3 = q_4 = q_6 = 0$, $q_2 = \pi/2$ and $q_5 = \pi/2$, resulting in

$$\mathbf{R}_d = \begin{bmatrix} -1 & 0 & 0 \\ 0 & -1 & 0 \\ 0 & 0 & 1 \end{bmatrix}. \quad (4.6)$$

The orientation of the end-effector represented by \mathbf{R}_d is used for both cases, the conical spiral and the straight line. The end-effector's orientation is constant over the time intervall $[t_0, t_e]$.

4.3.1 Straight Line

The straight line is defined as

$$\mathbf{p}_d(t) = \begin{bmatrix} x_0 \\ \lambda_y(t) \\ z_0 \end{bmatrix}, \quad (4.7)$$

with x_0 being the desired constant position on the x -direction and z_0 being the constant position on the z -direction. The y -position $\lambda_y(t)$ is determined in the time interval $t = [t_0, t_e]$, see (4.4). The y -position $\lambda_y(t)$ starts at $\lambda_y(t_0)$ and ends at $\lambda_y(t_e)$.

The straight line parameters are $x_0 = 0.834$ m, $z_0 = 1$ m, $y_d(t_0) = 0$ m and $y_d(t_e) = 0.50$ m, $t_0 = 0$ s and $t_e = 2.50$ s with a sampling time of $T_s = 1$ ms.

The desired link angle trajectories $\mathbf{q}_{d,i}$, $i = 1, \dots, 6$, of the straight line are calculated with the inverse kinematics (4.5), using the desired end-effector position determined by (4.7).

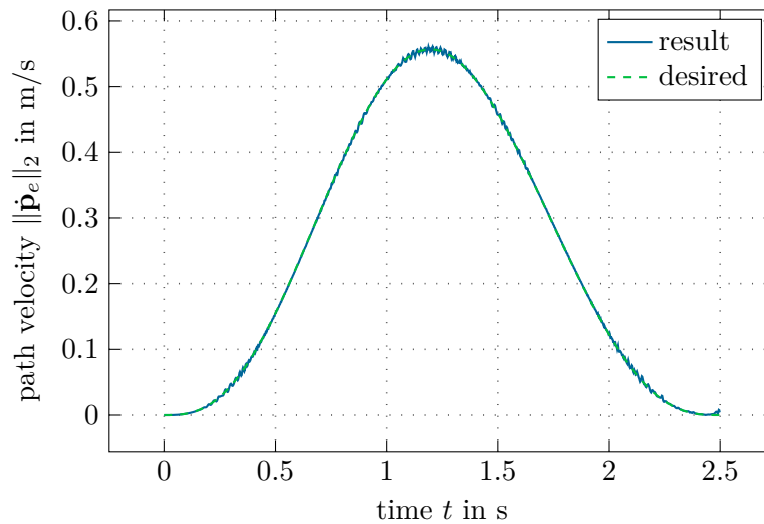


Figure 4.1: Path velocity of the straight line trajectory. Result using the optimal control input determined with (4.3) and a weighting factor of $\nu = 10^{-14}$.

The optimal control problem (4.3) for the straight line trajectory is solved using two different weighting factors ν . The results are needed to investigate the influence of ν on the required control bandwidth and on the pose accuracy. The frequency analysis for two weighting factors for all axes are depicted in Figure 4.3. All results indicate that by decreasing the weighting factor ν , the bandwidth increases slightly, as for the conical spiral in Section 4.3.2.

The influence of the weighting factor ν on the states and the control input is illustrated in Figure 4.4 and on the position error of the end-effector in Figure 4.2. The

velocity of the desired end-effector trajectory in the output space is depicted in Figure 4.1. The comparison between the desired and the calculated velocity with optimal control input in Figure 4.1 shows a good tracking behaviour. The results show the predicted behaviour, a smaller weighting factor increases the oscillations of the control input and the motor angular rate. A smaller weighting factor also decreases the oscillations on the link side, as can be seen in Figure 4.4(c). The opposite behaviour is to be observed for the position error of the end-effector, which is depicted in Figure 4.2, where a smaller weighting factor yields a higher accuracy.

The control bandwidth for axis 5 and 6 cannot be identified due to small velocity values, see Figure 4.3(e) and (f). The control bandwidth of axis 1, 2, 3 and 4 are significantly smaller for a high weighting factor as for a small weighting factor. A bandwidth of 100 Hz can be achieved for a weighting factor of 10^{-14} , as can be seen in Figure 4.3. The results indicate that for a higher position accuracy, a lower weighting factor is needed, which requires a higher control bandwidth.

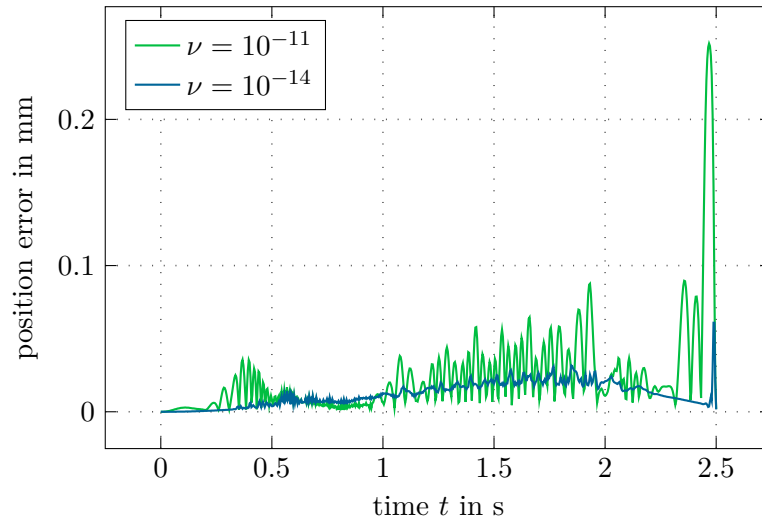


Figure 4.2: Norm of the position error $\|\mathbf{p}_d - \mathbf{p}_e\|_2$ of the straight line trajectory. Two results with different weighting values are compared.

The solution of the optimal control problem (4.3) with a weighting factor of $\nu = 10^{-14}$ for the straight line trajectory shows moderate errors for the desired link angles as well as for the orientation of the end-effector. The results are depicted in Figure 4.5. The position error is illustrated in Figure 4.5(c), the control input and motor angular rates in Figure 4.6 and the link angular rates in Figure 4.7.

The initial and terminal constraints on the angular rate and acceleration are fulfilled, as can be seen in Figures 4.6 and 4.7. Due to the the low weighting factor ν , high oscillations are present in the control input (Figure 4.6).

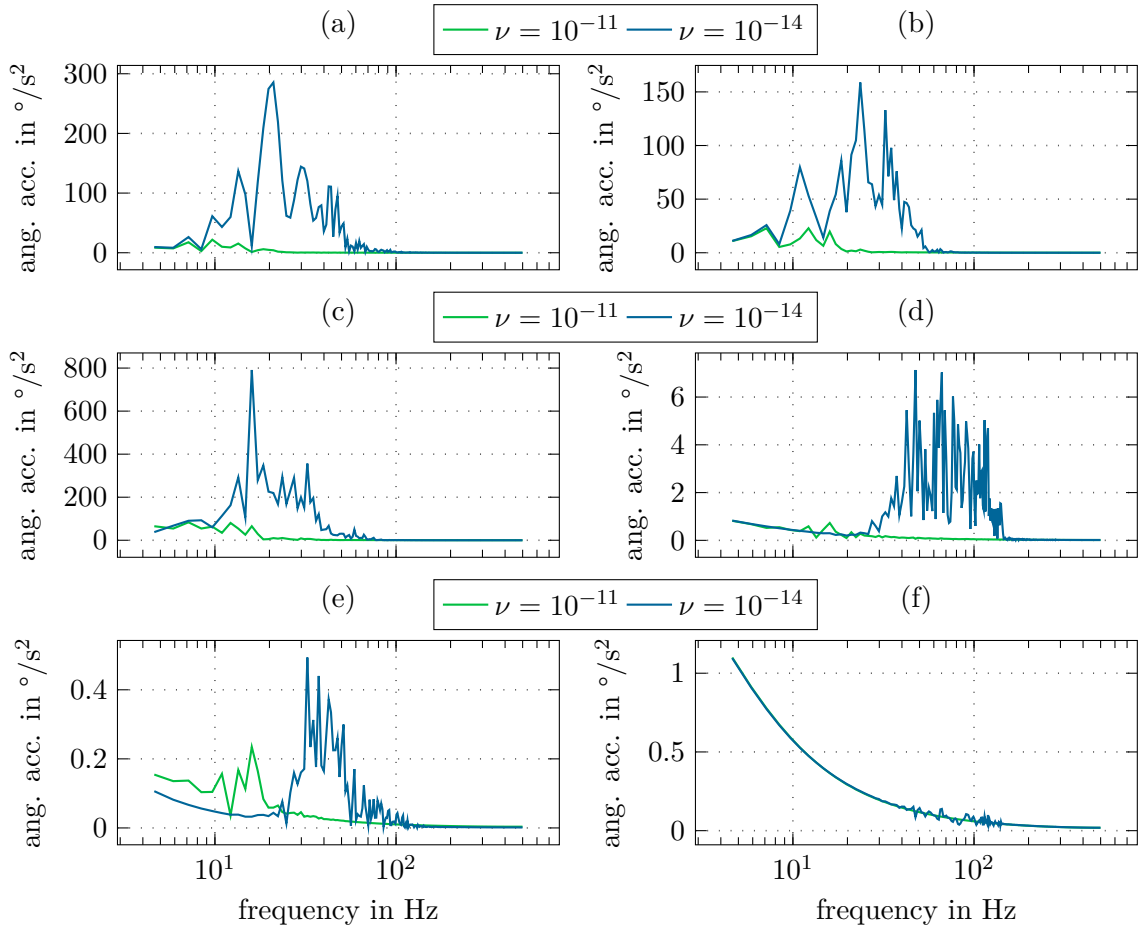


Figure 4.3: Frequency analysis of the control input $\mathbf{u} = \ddot{\boldsymbol{\theta}}$ calculated with two different weighting values ν for all axes (axis 1 (a), axis 2 (b), axis 3 (c), axis 4 (d), axis 5 (e) and axis 6 (f)) of the straight line example.

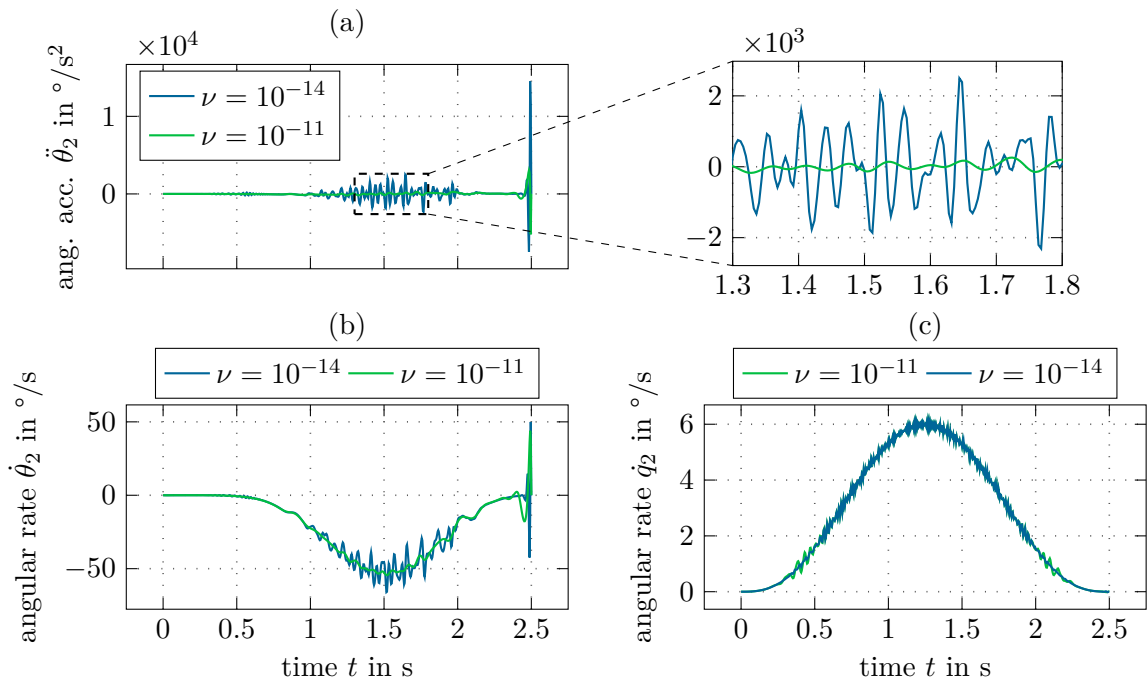


Figure 4.4: Comparison of the control input $u_2 = \ddot{\theta}_2$ in (a) and the states ($\dot{\theta}_2$ and \dot{q}_2 in (b) and (c), respectively) of axis 2 of the straight line trajectory calculated with different weighting factors ν .

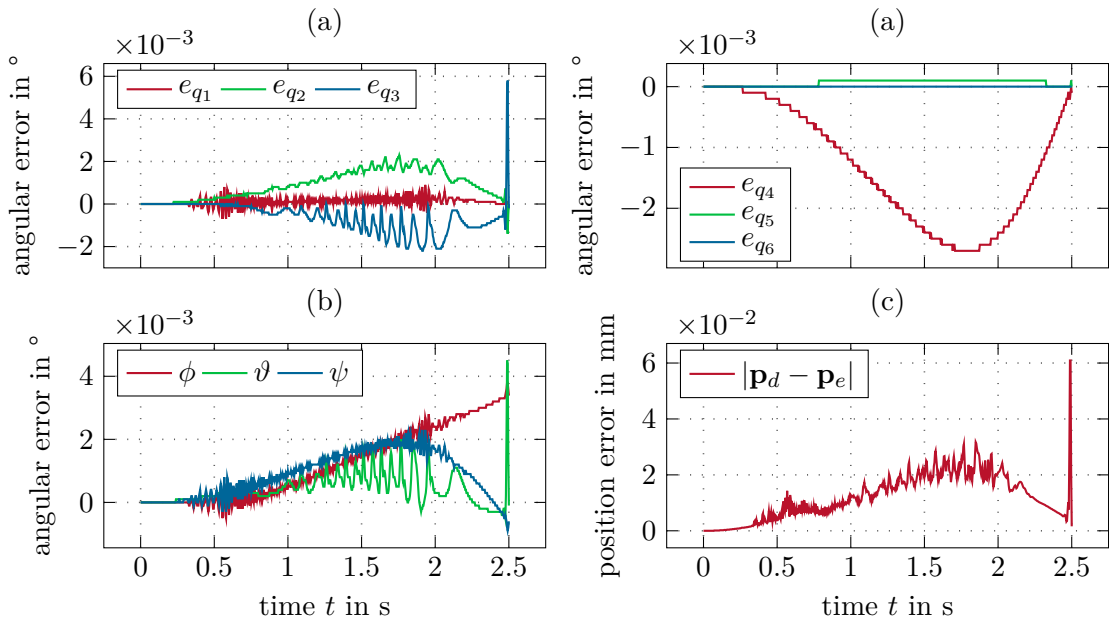


Figure 4.5: Errors of the link angles (a), of the orientation of the end-effector (b) and of the position of the end-effector (c) for the straight line trajectory. The optimal control problem is solved with a weighting factor of $\nu = 10^{-14}$.

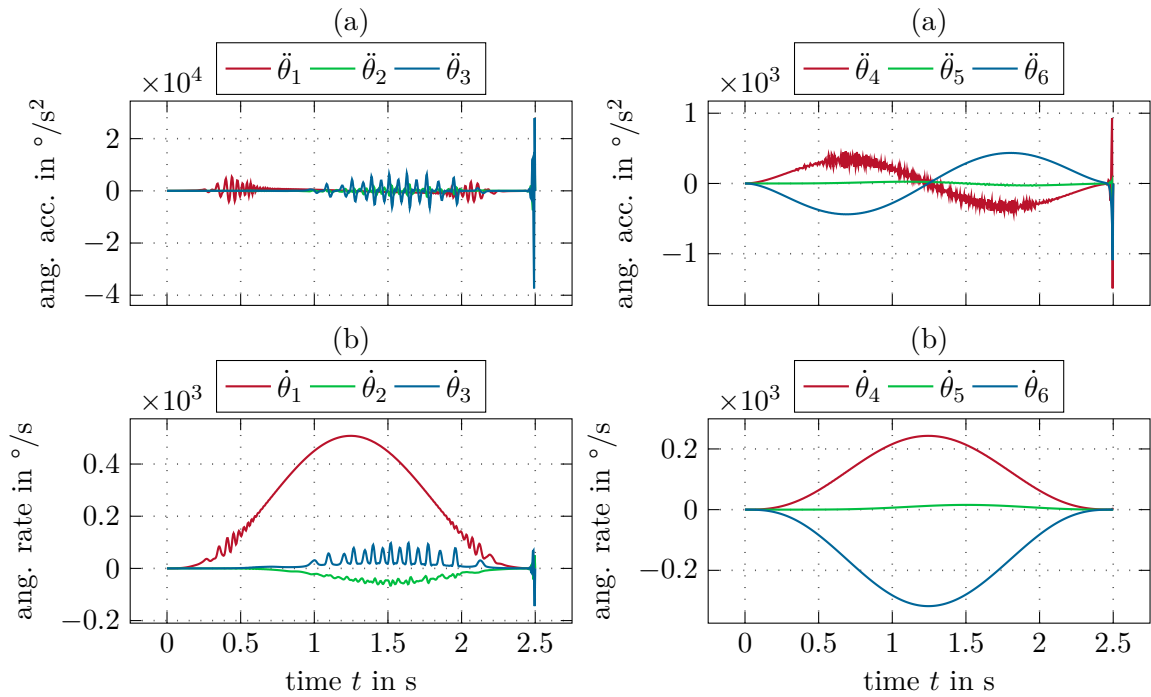


Figure 4.6: The control input $\mathbf{u} = \ddot{\theta}$ and the angular rate at the motor side $\dot{\theta}$ is depicted in (a) and (b), respectively, for the straight line trajectory. The optimal control problem is solved with a weighting factor of $\nu = 10^{-14}$.

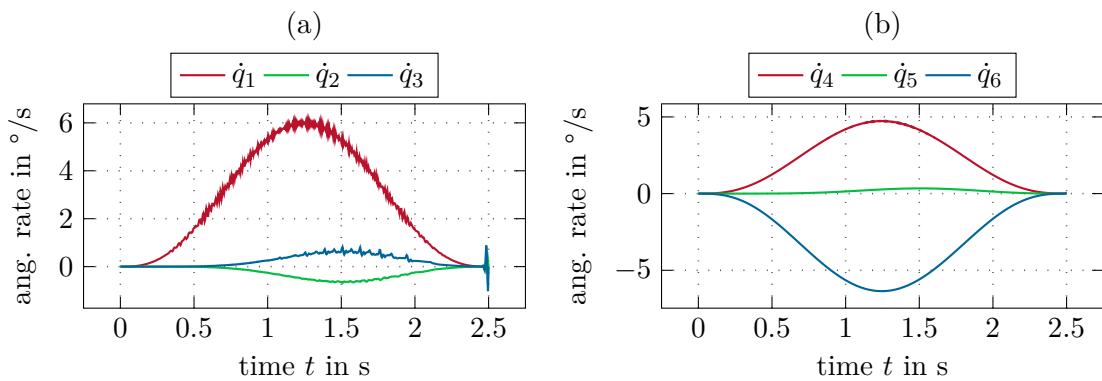


Figure 4.7: The angular rate at the link side $\dot{\mathbf{q}}$ for the straight line trajectory. The optimal control problem is solved with a weighting factor of $\nu = 10^{-14}$.

4.3.2 Conical Spiral

The spiral angle $\lambda_\mu(t)$ is determined over the time interval $t = [t_0, t_e]$, see (4.4). The start angle $\lambda_\mu(t_0)$ and the termination angle $\lambda_\mu(t_e)$ are given. The desired Euclidean position reads as

$$\mathbf{p}_d(t) = \begin{bmatrix} a\lambda_\mu(t) \cos(\lambda_\mu(t)) \\ a\lambda_\mu(t) \sin(\lambda_\mu(t)) \\ \lambda_z(t) \end{bmatrix}, \quad (4.8)$$

where the amplitude a is determined by the given maximum radius r_{max} and the given number of rotations n as $a = r_{max}/(2\pi n)$. The z -position $\lambda_z(t)$ is determined by (4.4) over the time interval $t = [t_0, t_e]$. The start value of the z -position $\lambda_z(t_0)$ and the terminal value of the z -position $\lambda_z(t_e)$ are given.

The conical spiral parameters are $n = 3/2$, $r_{max} = 0.10$ m, $z_d(t_0) = 1.10$ m, $z_d(t_e) = 1.50$ m, $\mu_d(t_0) = \pi/2$, $\mu_d(t_e) = 2\pi n$, $t_0 = 0$ s and $t_e = 2.50$ s with a sampling time of $T_s = 1$ ms. The resulting trajectory is depicted in Figure 4.8.

The desired link angle trajectories $\mathbf{q}_{d,i}$, $i = 1, \dots, 6$, of the conical spiral are calculated by the inverse kinematics (4.5) using the desired end-effector position given in (4.8).

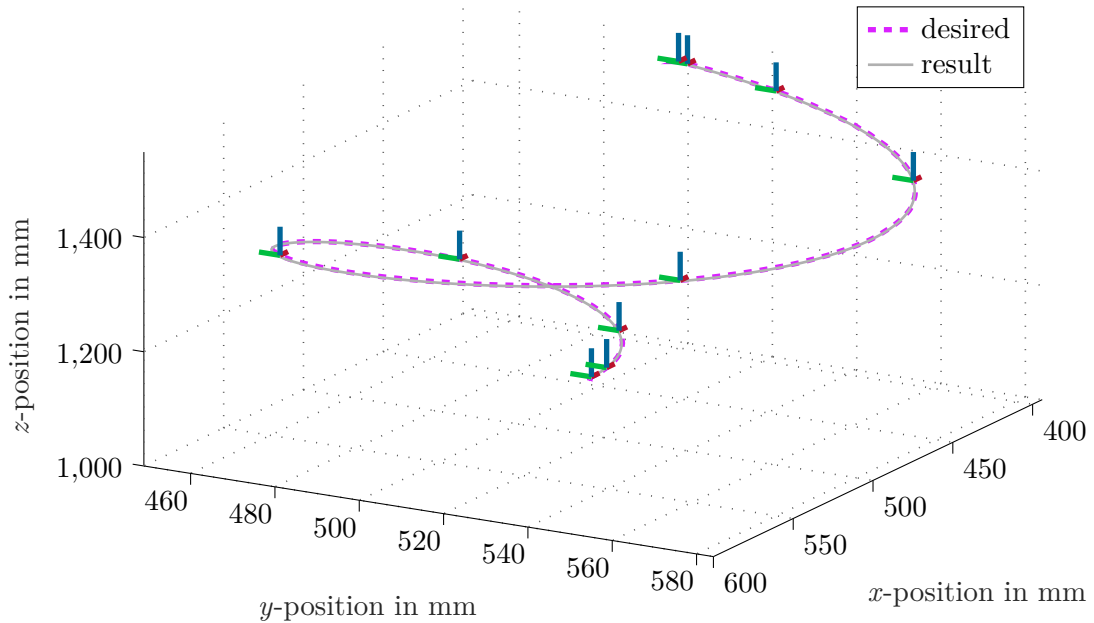


Figure 4.8: Comparison between the desired and the calculated conical spiral trajectory including orientation frames of the end-effector.

The optimal control problem (4.3) for the conical spiral trajectory is solved using two different weighting factors ν . The results are needed to investigate the influence of ν on the required control bandwidth and on the pose accuracy. The velocity of the desired

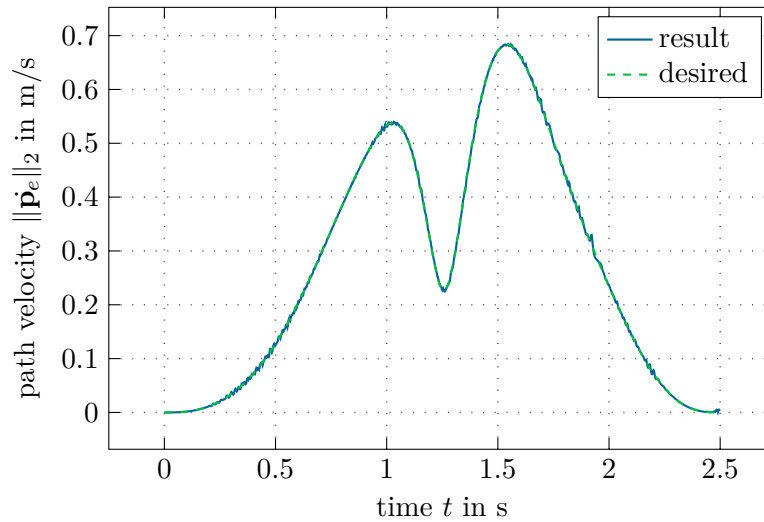


Figure 4.9: Velocity of the conical spiral trajectory. Result using the optimal control input determined with (4.3) and a weighting factor of $\nu = 10^{-14}$.

end-effector trajectory in the output space is illustrated in Figure 4.9. The comparison between the desired and the calculated velocity ((4.3) with a weighting factor $\nu = 10^{-14}$) in Figure 4.9 shows a good tracking behaviour. The frequency analysis for two weighting factors for all axes are depicted in Figure 4.10. All results indicate that by decreasing the weighting factor ν , the bandwidth increases slightly.

The influence of the weighting factor ν on the states and the control input is illustrated in Figure 4.11. In Figure 4.12, it can be seen that the choice of the weighting factor has a significant influence on the result. A large weighting factor increases the end-effector position error significantly, see Figure 4.12.

A solution of the optimal control problem (4.3) with a weighting factor of $\nu = 10^{-14}$ for the conical spiral trajectory shows moderate errors for the desired link angles as well as for the orientation of the end-effector. The results are depicted in Figure 4.13. The position error is illustrated in Figure 4.13(c) and the link and motor angular rates are depicted in Figure 4.14 and Figure 4.15, respectively. The control input is illustrated in Figure 4.15 and the resulting end-effector trajectory is depicted in Figure 4.8.

The initial and terminal constraints on the angular rate and acceleration are fulfilled as can be seen in Figure 4.14 and Figure 4.15. Due to the small weighting factor ν , large oscillations are present in the control input, as can be seen in Figure 4.15.

The results indicate the same conclusions as for the straight line example.

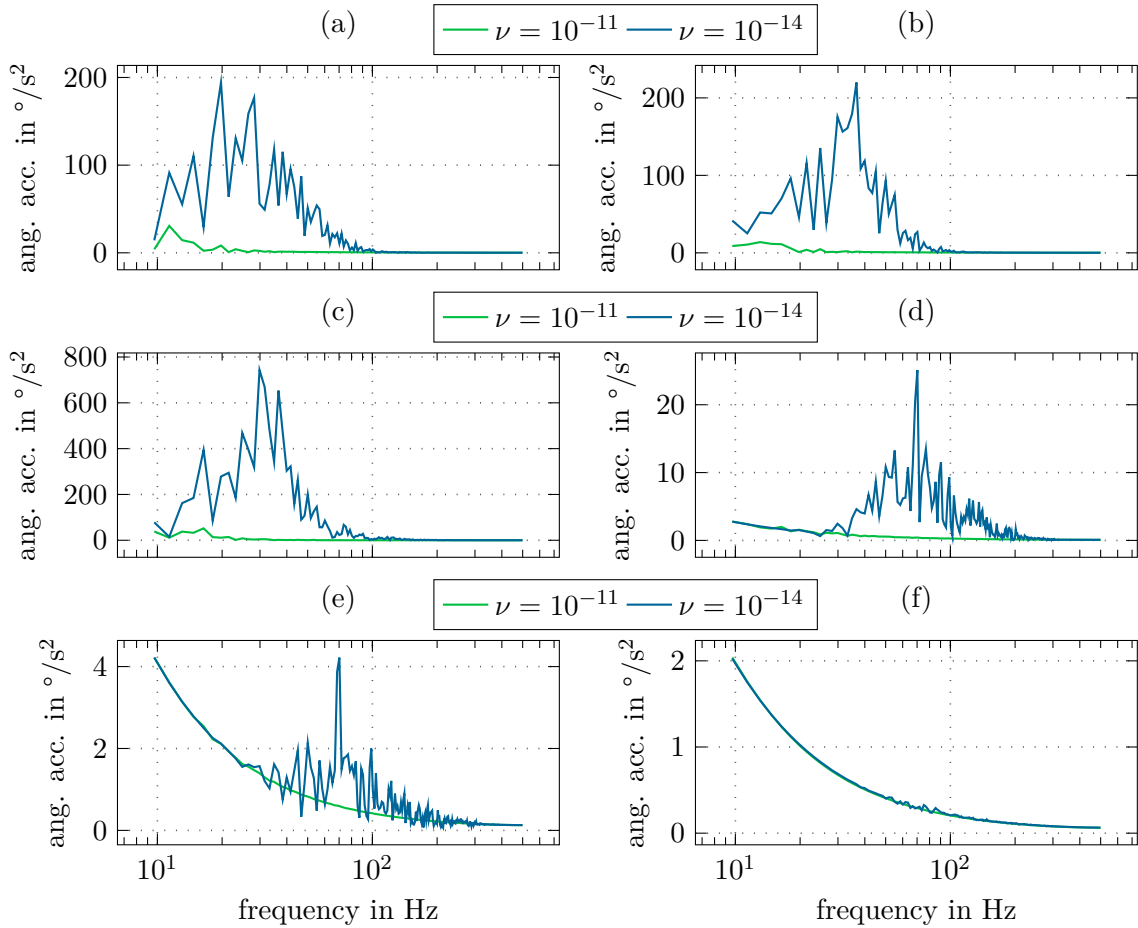


Figure 4.10: Frequency analysis for the control input $\mathbf{u} = \ddot{\boldsymbol{\theta}}$ calculated with different weighting factors ν for all axes (axis 1 (a), axis 2 (b), axis 3 (c), axis 4 (d), axis 5 (e) and axis 6 (f)) of the conical spiral example.

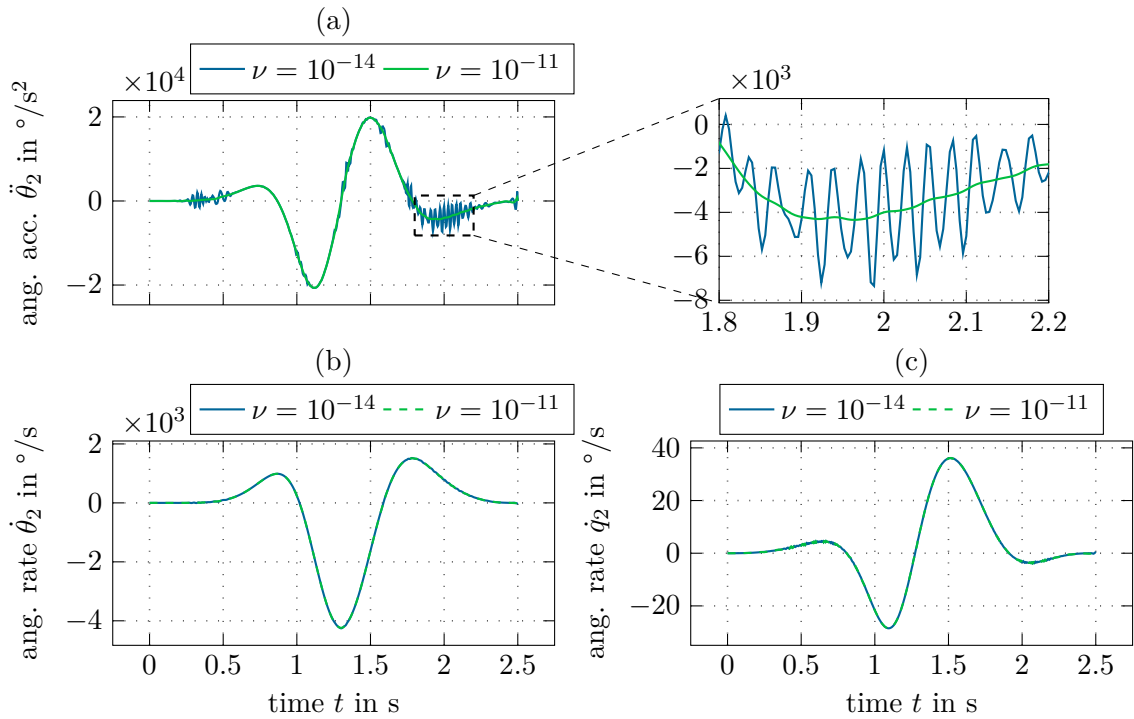


Figure 4.11: Comparison of the control input $u_2 = \ddot{\theta}_2$ (a) and the states ($\dot{\theta}_2$ in (b) and \dot{q}_2 in (c)) of axis 2 of the conical spiral trajectory calculated with different weighting factors ν .

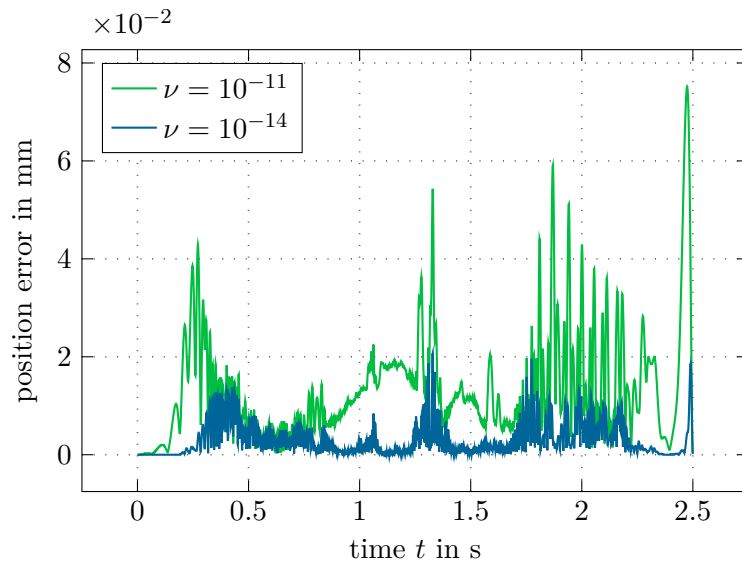


Figure 4.12: Norm of the position error $\|\mathbf{p}_d - \mathbf{p}_e\|_2$ of the conical spiral trajectory. Two results with different weighting factors are compared. A larger weighting factor ν increases the error significantly.

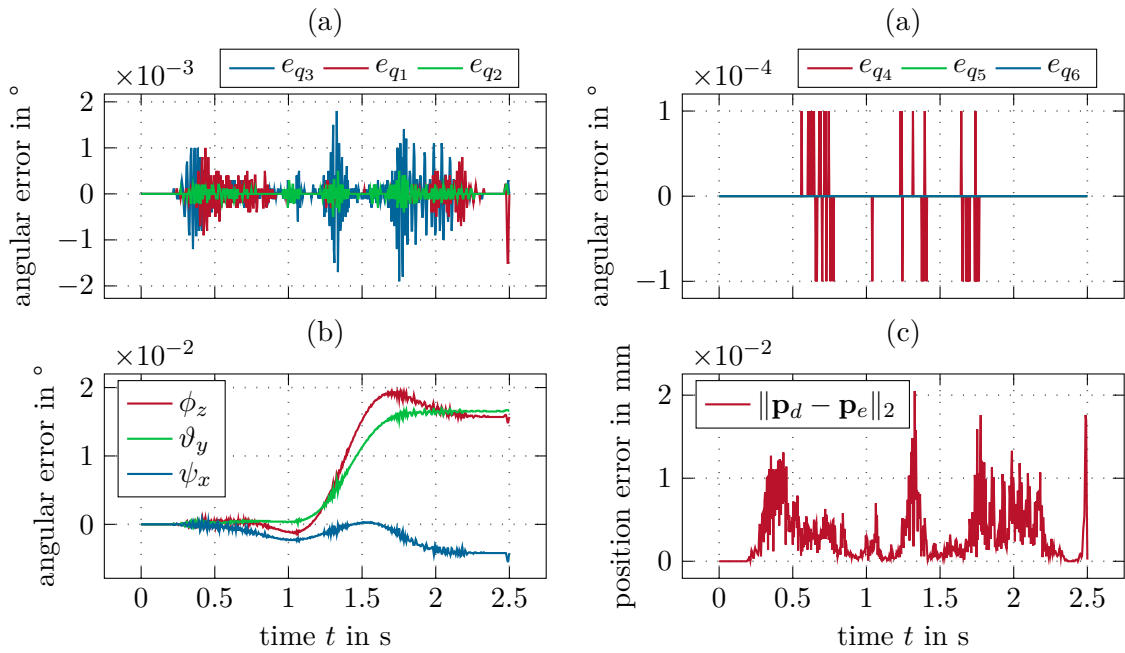


Figure 4.13: Errors of the link angles (a), of the orientation of the end-effector (b) and of the position of the end-effector (c) for the conical spiral trajectory. The optimal control problem is solved with a weighting factor of $\nu = 10^{-14}$.

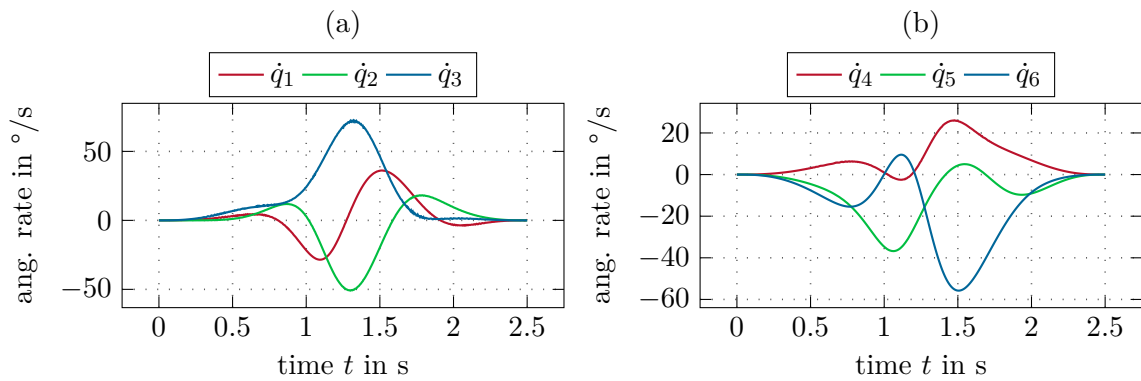


Figure 4.14: Angular rate at the link side $\dot{\mathbf{q}}$ of the conical spiral trajectory. The optimal control problem is solved with a weighting factor of $\nu = 10^{-14}$.

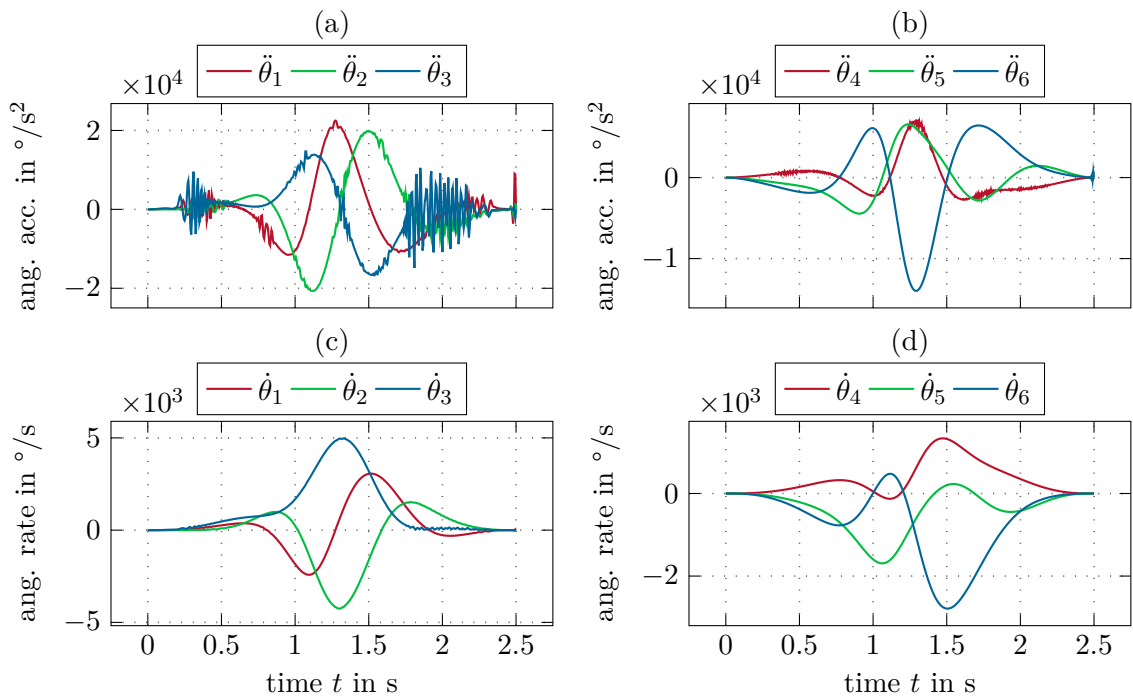


Figure 4.15: The control input $\mathbf{u} = \ddot{\boldsymbol{\theta}}$ of the conical spiral trajectory is illustrated in (a) and (b). The angular rate at the motor side $\dot{\boldsymbol{\theta}}$ is depicted in (c) and (d) of the conical spiral trajectory. The optimal control problem is solved with a weighting factor of $\nu = 10^{-14}$.

5 Conclusion

An offline trajectory planning algorithm is developed in this thesis in order to improve the absolute accuracy of a serial robot with six degrees of freedom. For this, accurate kinematic and dynamic models of the robot are required. These models incorporate non-constant gear ratios and non-linear joint stiffness. The so-called modified Denavit-Hartenberg (mDH) parameters are used for the kinematic model and are identified by exploiting 50 different position measurements. These 50 poses are determined by maximizing two observability indices. The non-constant gear ratios are composed of a linear ratio and a Fourier series and are identified for the first three gears. The non-linear joint stiffness is approximated by a linear and cubic term for the gears 2 and 3, whereby the parameters were identified in a previous work.

The considered control concept incorporates a high-bandwidth motor velocity controller. An optimal control problem is formulated to determine the motor's angular accelerations. The optimal control problem minimises the difference between the reference and the calculated link side angle. A quadratic term for the control input with a weighting factor is added to the cost functional to be able to limit the bandwidth of the control input. The results indicate that a smaller weighting factor increases the necessary controller bandwidth and the position accuracy.

The general strength of offline trajectory planning lies in the fact that the robot's operation does not need to be interrupted for teach-in of novel tasks. Applying the developed algorithm would have the advantage that tasks which require high precision could be performed with a standard industrial robot, instead of buying costly high-precision machinery. A number of different effects is jointly taken into consideration, such as deviations from nominal parameters, the behaviour of the dynamic system with joint elasticity and non-constant gear ratio, leading to highly precise results. The optimal trajectories can be used in conjunction with standard joint velocity controllers as reference signals. Another advantage is that no additional sensors are required, as would be the case for feedback control strategies.

Despite the multiple strengths of the presented approach, there are also several weaknesses. The major disadvantage is the necessary effort to model all the different effects in the system and the identification of the parameters. The proposed identification concept of the non-constant gear ratio neglects gear effects, such as friction, wear and backlash. These effects reduce the precision of the gear ratio model and bring along a different behaviour in both rotational directions.

Suggestions for future work and improvements for the presented algorithm:

- Due to the orientation inaccuracy of the optical sensor system, it was not possible to include orientation data for the identification process for the mDH-parameters. Therefore, in future work, it would be interesting to improve the identification of the geometric parameters, which would also lead to the possibility of identifying more parameters compared to the current situation.
- Moreover, it should be investigated in more detail, which of the gear effects (friction, wear, inner elasticity, backlash) should be included in the model to compensate the different behaviour of the non-constant gear ratio in both rotation directions.
- In this work, the acceleration is determined by solving the optimal control problem. However, it would be of interest to determine the jerk instead of the acceleration in order to see whether a damped jerk has a positive effect on the absolute accuracy due to a reduction of system vibrations.
- The offline trajectory planning should be tested on a real robot to verify the proposed approach.

A System Parameters

The angular link limits are listed in Table A.1. The angular rate limits at link side are

joint 1	$\pm 165^\circ$	joint 4	$\pm 210^\circ$
joint 2	-85° to 155°	joint 5	$\pm 135^\circ$
joint 3	-170° to 0°	joint 6	$\pm 270^\circ$

Table A.1: List of the joint position limits.

listed in Table A.2. The angular acceleration limits at link side are listed in Table A.2.

joint 1	$\pm 220^\circ/\text{s}$	joint 4	$\pm 550^\circ/\text{s}$
joint 2	$\pm 250^\circ/\text{s}$	joint 5	$\pm 550^\circ/\text{s}$
joint 3	$\pm 300^\circ/\text{s}$	joint 6	$\pm 600^\circ/\text{s}$

Table A.2: List of the joint angular velocity limits.

joint 1	$\pm 400^\circ/\text{s}^2$	joint 4	$\pm 1279.07^\circ/\text{s}^2$
joint 2	$\pm 555.56^\circ/\text{s}^2$	joint 5	$\pm 1279.07^\circ/\text{s}^2$
joint 3	$\pm 666.67^\circ/\text{s}^2$	joint 6	$\pm 1395.35^\circ/\text{s}^2$

Table A.3: List of the joint angular acceleration limits.

A.1 Non-Constant Gear Transmission

The basic frequencies used to filter the measurements for the non-constant gear ratio identification are listed in Table A.4. The identified basic gear ratio u_0 of all gears are listed in Table A.5. The identified non-constant gear ratio parameters for gear 1 are listed in Table A.6 and Table A.9 for the clockwise and counter-clockwise rotation direction, respectively.

The identified non-constant gear ratio parameters for gear 2 are listed in Table A.7 and Table A.10 for the clockwise and counter-clockwise rotation direction, respectively.

The identified non-constant gear ratio parameters for gear 3 are listed in Table A.8 and Table A.11 for the clockwise and counter-clockwise rotation direction, respectively.

Gear 1	200 $\frac{84.8639}{360}$
Gear 2	150 $\frac{83}{360}$
Gear 3	300 $\frac{69}{360}$

Table A.4: 3 dB frequencies of the acausal Gaussian filter used to process the raw sensor data at gears.

Gear 1	84.86	Gear 4	51.42
Gear 2	82.84	Gear 5	46.03
Gear 3	69.05	Gear 6	50

Table A.5: Basic gear ratio u_0 of each gear ($\theta = u_0\varphi$).

Frequency	84	85	86
\hat{a}	$-1.9599 \cdot 10^{-4}$	$-8.0138 \cdot 10^{-4}$	$8.1075 \cdot 10^{-5}$
\hat{b}	$6.8974 \cdot 10^{-4}$	$3.3481 \cdot 10^{-3}$	$-3.4429 \cdot 10^{-4}$
Frequency	100	101	102
\hat{a}	$1.2010 \cdot 10^{-4}$	$1.1480 \cdot 10^{-3}$	$-3.0640 \cdot 10^{-5}$
\hat{b}	$3.4218 \cdot 10^{-5}$	$1.7547 \cdot 10^{-3}$	$-2.4775 \cdot 10^{-4}$
Frequency	201	202	203
\hat{a}	$-5.0571 \cdot 10^{-5}$	$-8.3859 \cdot 10^{-4}$	$1.4426 \cdot 10^{-5}$
\hat{b}	$2.0278 \cdot 10^{-4}$	$8.7013 \cdot 10^{-4}$	$2.2636 \cdot 10^{-7}$
Frequency	302	303	304
\hat{a}	$-1.4690 \cdot 10^{-5}$	$-7.2201 \cdot 10^{-4}$	$3.2964 \cdot 10^{-4}$
\hat{b}	$6.4590 \cdot 10^{-5}$	$-4.4223 \cdot 10^{-4}$	$8.9773 \cdot 10^{-5}$

Table A.6: Calculated Fourier series parameters for the gear ratio of the first gear at a link side speed of $\sim 88^\circ/\text{s}$ (clockwise rotation).

A.2 Modified Denavit-Hartenberg Parameters

The nominal modified Denavit-Hartenberg parameters are listed in Table A.12. The 50 poses used to identify the mDH-parameters are listed in Table A.13 and Table A.14.

Frequency	82	83	84
\hat{a}	$-7.9810 \cdot 10^{-4}$	$8.1529 \cdot 10^{-4}$	$-9.2458 \cdot 10^{-4}$
\hat{b}	$1.7784 \cdot 10^{-5}$	$-5.0526 \cdot 10^{-4}$	$2.8779 \cdot 10^{-4}$
Frequency	166	167	168
\hat{a}	$-9.7930 \cdot 10^{-4}$	$1.7552 \cdot 10^{-3}$	$-5.6119 \cdot 10^{-4}$
\hat{b}	$-2.8176 \cdot 10^{-4}$	$1.8198 \cdot 10^{-5}$	$1.1522 \cdot 10^{-4}$
Frequency	332	333	334
\hat{a}	$-3.7139 \cdot 10^{-4}$	$6.7582 \cdot 10^{-4}$	$-3.8982 \cdot 10^{-4}$
\hat{b}	$-1.3090 \cdot 10^{-4}$	$4.3719 \cdot 10^{-5}$	$1.9972 \cdot 10^{-5}$

Table A.7: Calculated Fourier series parameters for the gear ratio of the second gear at a link side speed of $\sim 100^\circ/\text{s}$ (clockwise rotation).

Frequency	69	70	71
\hat{a}	$-3.6720 \cdot 10^{-3}$	$-1.8020 \cdot 10^{-4}$	$1.6928 \cdot 10^{-3}$
\hat{b}	$-2.5104 \cdot 10^{-3}$	$-9.7410 \cdot 10^{-4}$	$1.1443 \cdot 10^{-3}$
Frequency	139	140	141
\hat{a}	$4.3869 \cdot 10^{-3}$	$5.2646 \cdot 10^{-3}$	$-5.3575 \cdot 10^{-3}$
\hat{b}	$-4.3598 \cdot 10^{-3}$	$1.1936 \cdot 10^{-2}$	$5.1064 \cdot 10^{-4}$
Frequency	279	280	281
\hat{a}	$-1.5404 \cdot 10^{-3}$	$3.3034 \cdot 10^{-3}$	$1.0239 \cdot 10^{-3}$
\hat{b}	$-1.0324 \cdot 10^{-3}$	$-2.5814 \cdot 10^{-3}$	$2.0083 \cdot 10^{-3}$

Table A.8: Calculated Fourier series parameters for the gear ratio of the third gear at a link side speed of $\sim 61^\circ/\text{s}$ (clockwise rotation).

Frequency	84	85	86
\hat{a}	$1.3196 \cdot 10^{-5}$	$-1.5298 \cdot 10^{-4}$	$-4.1560 \cdot 10^{-5}$
\hat{b}	$6.9446 \cdot 10^{-4}$	$2.6671 \cdot 10^{-3}$	$-1.2274 \cdot 10^{-4}$
Frequency	100	101	102
\hat{a}	$8.7795 \cdot 10^{-5}$	$1.8095 \cdot 10^{-3}$	$-1.6665 \cdot 10^{-4}$
\hat{b}	$-2.4542 \cdot 10^{-4}$	$-5.4497 \cdot 10^{-4}$	$-9.4132 \cdot 10^{-5}$
Frequency	201	202	203
\hat{a}	$4.8143 \cdot 10^{-4}$	$1.8396 \cdot 10^{-4}$	$2.2408 \cdot 10^{-4}$
\hat{b}	$1.3366 \cdot 10^{-4}$	$3.3193 \cdot 10^{-4}$	$-5.3538 \cdot 10^{-5}$
Frequency	302	303	304
\hat{a}	$-5.4537 \cdot 10^{-5}$	$4.2001 \cdot 10^{-4}$	$-9.7523 \cdot 10^{-5}$
\hat{b}	$-2.0219 \cdot 10^{-5}$	$-5.6079 \cdot 10^{-4}$	$2.2711 \cdot 10^{-4}$

Table A.9: Calculated Fourier series parameters for the gear ratio of the first gear at a link side speed of $\sim 88^\circ/\text{s}$ (counter-clockwise rotation).

Frequency	82	83	84
\hat{a}	$2.0578 \cdot 10^{-4}$	$-7.6000 \cdot 10^{-5}$	$7.4211 \cdot 10^{-4}$
\hat{b}	$-4.9481 \cdot 10^{-4}$	$1.2640 \cdot 10^{-3}$	$-1.0959 \cdot 10^{-3}$
Frequency	166	167	168
\hat{a}	$3.2368 \cdot 10^{-4}$	$-8.5019 \cdot 10^{-4}$	$4.7525 \cdot 10^{-4}$
\hat{b}	$6.1619 \cdot 10^{-4}$	$-1.2524 \cdot 10^{-3}$	$3.5221 \cdot 10^{-4}$
Frequency	332	333	334
\hat{a}	$9.3045 \cdot 10^{-5}$	$-2.0740 \cdot 10^{-4}$	$8.5329 \cdot 10^{-5}$
\hat{b}	$6.9828 \cdot 10^{-5}$	$-1.1308 \cdot 10^{-5}$	$-8.5659 \cdot 10^{-5}$

Table A.10: Calculated Fourier series parameters for the gear ratio of the second gear at a link side speed of $\sim 100^\circ/\text{s}$ (counter-clockwise rotation).

Frequency	69	70	71
\hat{a}	$-1.1903 \cdot 10^{-2}$	$1.0328 \cdot 10^{-2}$	$2.0117 \cdot 10^{-2}$
\hat{b}	$-4.9637 \cdot 10^{-3}$	$-2.4999 \cdot 10^{-2}$	$5.1772 \cdot 10^{-3}$
Frequency	139	140	141
\hat{a}	$-3.1309 \cdot 10^{-3}$	$7.0925 \cdot 10^{-3}$	$4.4961 \cdot 10^{-4}$
\hat{b}	$-3.3092 \cdot 10^{-3}$	$-2.1233 \cdot 10^{-3}$	$2.5442 \cdot 10^{-3}$
Frequency	279	280	281
\hat{a}	$3.2194 \cdot 10^{-4}$	$-8.8841 \cdot 10^{-4}$	$-5.0971 \cdot 10^{-4}$
\hat{b}	$5.4501 \cdot 10^{-4}$	$4.1734 \cdot 10^{-4}$	$-6.7765 \cdot 10^{-4}$

Table A.11: Calculated Fourier series parameters for the gear ratio of the third gear at a link side speed of $\sim 61^\circ/\text{s}$ (counter-clockwise rotation).

i	d_i in m	a_i in m	α_i in rad	β_i in rad	i	d_i in m	a_i in m	α_i in rad	β_i in rad
1	0.43	0.15	$\pi/2$	x	4	0.684	0	$-\pi/2$	x
2	0	0.59	0	x	5	0	0	$\pi/2$	x
3	0	0.13	$\pi/2$	0	6	0.1	0	0	x

Table A.12: Nominal mDH parameters of the COMAU Racer-7-1.4 [15].

θ_1 in $^\circ$	θ_2 in $^\circ$	θ_3 in $^\circ$	θ_4 in $^\circ$	θ_5 in $^\circ$	θ_6 in $^\circ$
-2180.083	-3077.643	-3643.426	3223.564	1423.491	-1488.244
-1875.437	-3512.313	-4424.812	6754.946	4124.396	807.597
-845.255	-3669.127	-6155.887	218.914	309.474	-9588.460
-979.080	2424.316	-9665.747	6356.931	2656.646	7685.968
-5726.955	4479.118	-10863.371	-2387.989	-1062.051	-5954.475
-7224.281	936.207	-9565.772	-6789.914	2773.138	-13295.945
-7136.717	97.308	-9825.016	-298.758	-1453.258	-12777.447
-11505.547	-1731.540	-11139.852	-9545.681	-4237.484	2207.891
-9070.587	-4361.686	-4787.823	-620.215	-2810.819	-10290.958
-3188.804	-2442.735	-561.291	3418.046	-4134.150	1200.045
-9687.183	-7165.367	-54.062	6971.438	4192.396	-11796.451
-8127.942	6125.954	-1494.390	6749.290	4270.702	3922.184
-10770.048	-6688.187	-537.194	-9289.079	-4063.482	12136.450
6265.160	6138.765	-775.402	-5743.967	4081.977	5127.979
-8092.441	-577.624	-7290.493	4428.614	659.296	-6229.474
10141.562	5614	-391.424	6036.050	-1881.363	683.847
10931.416	6297.492	-130.698	8596.409	-1289.561	5559.477
-3798.521	-5045.677	-4504.999	-3632.223	675.905	10841.955
-3756.650	-1985.604	-2554.670	2126.090	-3624.334	-8451.965
-8624.701	6994.378	-5972.554	-307.007	-688.787	3230.037
13398.650	4002.437	-1910.766	5296.071	2326.078	-3783.234
475.909	-1507.093	-2301.425	5928.576	2922.619	1496.844
1242.789	2397.612	-8033.751	9724.119	1769.058	-6311.474
-11100.428	3815.176	-1424.822	6344.589	-4176.063	-7759.468
1514.312	3772.249	-6349.423	7229.068	-975.326	-383.878

Table A.13: First half of the 50 robot configurations, used to identify the mDH parameters of the COMAU Racer-7-1.4.

θ_1 in $^\circ$	θ_2 in $^\circ$	θ_3 in $^\circ$	θ_4 in $^\circ$	θ_5 in $^\circ$	θ_6 in $^\circ$
12 911.997	5276.580	-7198.792	2730.055	-2775.761	12 631.948
4313.879	6353.313	-6927.137	-3137.841	3658.610	4419.182
2392.665	2727.878	-2212.206	6965.781	-3179.620	-4613.731
5735.278	5001.054	-2559.428	9894.844	4004.729	8199.466
8404.391	6220.791	-4031.327	3189.110	335.307	10 633.456
-3777.628	-3141.533	-215.634	-3746.537	-3065.474	-2611.839
-12 215.567	-2724.916	-58.406	-3524.389	-3480.145	3341.486
949.354	5190.728	-316.760	3451.934	4187.658	5366.478
13 558.319	-187.245	-8485.359	320.269	-2399.599	-10 561.956
11 456.287	-2199.153	-8705.993	-5296.585	-3990.743	8732.464
10 043.891	-967.021	-10 237.325	-4682.027	-1800.435	2199.841
3080.772	-2201.566	-10 349.710	-3066.826	4226.948	-6825.472
4431.593	-4197.718	-5161.176	-5169.570	-3666.754	-1300.345
3759.622	-7497.047	-341.650	-6835.680	205.086	2747.889
-10 550.927	6351.399	-287.926	-2380.635	-467.626	-4391.982
-10 852.431	5713.163	-33.909	-5814.417	-3887.961	2727.539
7371.720	-3789.753	-2138.708	8195.309	3566.088	-122.614
6340.153	-2910.347	-1315.401	-4262.774	4259.890	6773.972
4973.705	-3679.193	-313.209	-3296.070	578.092	-416.253
10 037.097	-381.245	-2965.117	4289.566	2042.438	-6706.972
-5768.825	3827.072	-2854.938	-9373.413	-1918.262	-8131.466
11 313.604	-3923.190	-396.954	-554.496	4028.976	-6259.474
-4837.476	4831.845	-604.756	-3891.807	4250.413	-5314.478
9058.697	-7262.117	-393.003	519.168	180.044	7736.968
1241.855	-6823.122	-270.145	3258.068	-3429.812	-187.354

Table A.14: Second half of the 50 robot configurations, used to identify the mDH parameters of the COMAU Racer-7-1.4.

A.3 Non-linear Stiffness

The non-linear stiffness is determined by experiments in a previous work. The load experiments exhibit a hysteresis behaviour. The stiffness is approximated by a sum of a cubic and a linear term. The results for axis 2 and axis 3 are depicted in Figure A.1(a) and (b), respectively.

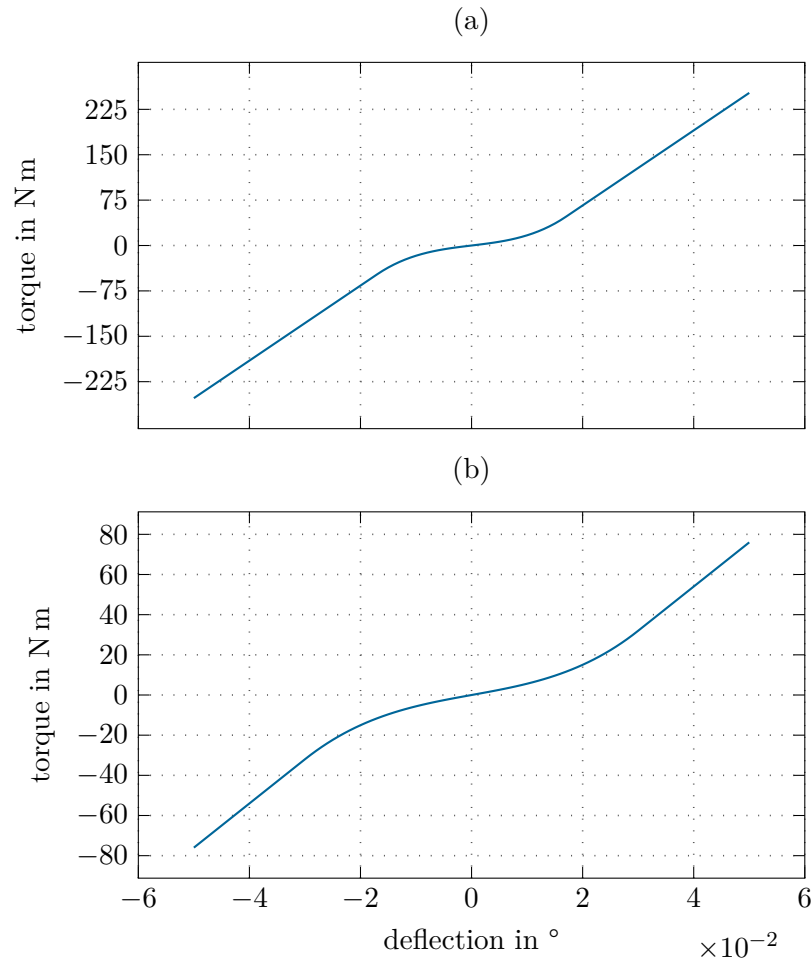


Figure A.1: The stiffness curve of axis 2 (a) and 3 (b) determined by load experiments by Moien Reyhani-Masouleh.

A.4 Dynamic Parameters

The dynamic parameters are determined by optimal trajectory experiments in [15]. For a detailed list of the dynamic parameters, please see [15].

Bibliography

- [1] B. Siciliano and O. Khatib, Eds., *Springer Handbook of Robotics*. New York: Springer International Publishing, 2016, ISBN: 978-3-319-32552-1.
- [2] A.-D. Pham and H.-J. Ahn, “High precision reducers for industrial robots driving 4th industrial revolution: state of arts, analysis, design, performance evaluation and perspective,” *International Journal of Precision Engineering and Manufacturing-Green Technology*, vol. 5, no. 4, pp. 519–533, 2018.
- [3] T. D. Tuttle, “Understanding and modeling the behavior of a Harmonic drive gear transmission,” MIT ARTIFICIAL INTELLIGENCE LAB, Tech. Rep. AITR-1365, May 1992.
- [4] J. W. Sensinger and J. H. Lipsey, “Cycloid vs. Harmonic drives for use in high ratio, single stage robotic transmissions,” in *Proceedings of the IEEE International Conference on Robotics and Automation*, St Paul, MN, USA, May 2012, pp. 4130–4135.
- [5] T. Tuttle and W. Seering, “A nonlinear model of a Harmonic drive gear transmission,” *IEEE Transactions on Robotics and Automation*, vol. 12, no. 3, pp. 368–374, 1996.
- [6] X. Shi, Y. Han, J. Wu, and Z. Xiong, “An FFT-based method for analysis, modeling and identification of kinematic error in Harmonic Drives,” in *Proceedings of the International Conference on Intelligent Robotics and Applications*, Shenyang, China, Aug. 2019, pp. 191–202.
- [7] F. H. Ghorbel, P. S. Gandhi, and F. Alpeter, “On the kinematic error in Harmonic drive gears,” *Journal of Mechanical Design*, vol. 123, no. 1, pp. 90–97, 2001.
- [8] M. Yamamoto, M. Iwasaki, H. Hirai, Y. Okitsu, K. Sasaki, and T. Yajima, “Modeling and compensation for angular transmission error in Harmonic drive gearings,” *Transactions on Electrical and Electronic Engineering*, vol. 4, no. 2, pp. 158–165, 2009.
- [9] M. Thümmel, “Modellbasierte Regelung mit nichtlinearen inversen Systemen und Beobachtern von Robotern mit elastischen Gelenken,” Ph.D. dissertation, Technische Universität München – Lehrstuhl für Elektrische Antriebssysteme, Munich, Germany, 2006.
- [10] M. Aberger, “Modellierung und Identifikation eines CYCLO-Getriebes für Industrieroboter,” M.S. thesis, Johannes Kepler Universität - Institut für Design und Regelung Mechatronischer Systeme, Linz, Austria, 2003.
- [11] H. Tonshoff and J. Kummetz, “Active compensation of kinematic transmission errors in servo drives for machine tools and robots,” in *Proceedings of the American Control Conference*, vol. 4, San Diego, CA, USA, Jun. 1999, pp. 2590–2594.

- [12] L. R. Rabiner, R. W. Schafer, and C. M. Rader, "The Chirp Z-transform algorithm and its application," *Bell System Technical Journal*, vol. 48, no. 5, pp. 1249–1292, 1969.
- [13] P. Tomei, "A simple PD controller for robots with elastic joints," *IEEE Transactions on Automatic Control*, vol. 36, no. 10, pp. 1208–1213, 1991.
- [14] A. D. Luca, B. Siciliano, and L. Zollo, "PD control with on-line gravity compensation for robots with elastic joints: Theory and experiments," *Automatica*, vol. 41, no. 10, pp. 1809–1819, 2005.
- [15] B. Bischof, *Path and Surface Following Control for Industrial Robotic Applications*, A. Kugi and K. Schlacher, Eds., ser. Modellierung und Regelung komplexer dynamischer Systeme. Aachen: Shaker Verlag, 2020, ISBN: 978-3-8440-7200-6.
- [16] B. Siciliano, L. Sciavicco, L. Villani, and G. Oriolo, *Robotics: Modelling, Planning and Control*. London: Springer, 2010, ISBN: 978-1-84628-642-1.
- [17] Chen-Gang, Li-Tong, Chu-Ming, J.-Q. Xuan, and S.-H. Xu, "Review on kinematics calibration technology of serial robots," *International Journal of Precision Engineering and Manufacturing*, vol. 15, no. 8, pp. 1759–1774, 2014.
- [18] K. M. Lynch and F. C. Park, *Modern Robotics: Mechanics, Planning and Control*. Cambridge: Cambridge University Press, 2017, ISBN: 978-1107156302.
- [19] S. Hayati and M. Mirmirani, "Improving the absolute positioning accuracy of robot manipulators," *Journal of Robotic Systems*, vol. 2, no. 4, pp. 397–413, 1985.
- [20] W. Khalil, S. Besnard, and P. Lemoine, "Comparison study of the geometric parameters calibration methods," *International Journal of Robotics and Automation*, vol. 15, no. 2, pp. 56–67, 2000.
- [21] W. Khalil and M. Gautier, "Calculation of the identifiable parameters for robots calibration," in *Proceedings of the 9th IFAC/IFORS Symposium on Identification and System Parameter Estimation*, vol. 24, Budapest, Hungary, Jul. 1991, pp. 687–691.
- [22] M. A. Meggiolaro and S. Dubowsky, "An analytical method to eliminate the redundant parameters in robot calibration," in *Proceedings of the IEEE International Conference on Robotics and Automation*, vol. 4, San Francisco, CA, USA, Aug. 2000, pp. 3609–3615.
- [23] Y. Sun and J. M. Hollerbach, "Observability index selection for robot calibration," in *Proceedings of the IEEE International Conference on Robotics and Automation*, Pasadena, CA, USA, May 2008, pp. 831–836.
- [24] A. Nahvi and J. M. Hollerbach, "The noise amplification index for optimal pose selection in robot calibration," in *Proceedings of the IEEE International Conference on Robotics and Automation*, vol. 1, Minneapolis, MN, USA, Apr. 1996, pp. 647–654.
- [25] J. M. Hollerbach and C. W. Wampler, "The calibration index and taxonomy for robot kinematic calibration methods," *The International Journal of Robotics Research*, vol. 15, no. 6, pp. 573–591, 1996.

- [26] W. Wang, H. Song, Z. Yan, L. Sun, and Z. Du, "A universal index and an improved PSO algorithm for optimal pose selection in kinematic calibration of a novel surgical robot," *Robotics and Computer-Integrated Manufacturing*, vol. 50, pp. 90–101, 2018.
- [27] T. J. Mitchell, "An algorithm for the construction of D-Optimal experimental designs," *Technometrics*, vol. 42, no. 1, pp. 48–54, 2000.
- [28] A. Nubiola and I. A. Bonev, "Absolute calibration of an ABB IRB 1600 robot using a laser tracker," *Robotics and Computer-Integrated Manufacturing*, vol. 29, no. 1, pp. 236–245, 2013.
- [29] D. Daney, Y. Papegay, and B. Madeline, "Choosing measurement poses for robot calibration with the local convergence method and Tabu Search," *The International Journal of Robotics Research*, vol. 24, no. 6, pp. 501–518, 2005.
- [30] J.-L. Caenen and J.-C. Angue, "Identification of geometric and nongeometric parameters of robots," in *Proceedings of the IEEE International Conference on Robotics and Automation*, Cincinnati, OH, USA, May 1990, pp. 1032–1037.
- [31] J.-H. Borm and C.-H. Meng, "Determination of optimal measurement configurations for robot calibration based on observability measure," *The International Journal of Robotics Research*, vol. 10, no. 1, pp. 51–63, 1991.
- [32] T. Chettibi, "Smooth point-to-point trajectory planning for robot manipulators by using radial basis functions," *Robotica*, vol. 37, no. 3, pp. 539–559, 2018.
- [33] Y. Fang, J. Hu, W. Liu, Q. Shao, J. Qi, and Y. Peng, "Smooth and time-optimal S-curve trajectory planning for automated robots and machines," *Mechanism and Machine Theory*, vol. 137, pp. 127–153, 2019.
- [34] M. Vakilinejad, A. Olabi, and O. Gibaru, "Identification and compensation of periodic gear transmission errors in robot manipulators," in *Proceedings of the IEEE International Conference on Industrial Technology*, Melbourne, Australia, Feb. 2019, pp. 126–132.
- [35] A. Olabi, M. Damak, R. Bearee, O. Gibaru, and S. Leleu, "Improving the accuracy of industrial robots by offline compensation of joints errors," in *Proceedings of the International Conference on Industrial Technology*, Kos, Greece, Mar. 2012, pp. 492–497.
- [36] D. Chen, T. Wang, P. Yuan, N. Sun, and H. Tang, "A positional error compensation method for industrial robots combining error similarity and radial basis function neural network," *Measurement Science and Technology*, vol. 30, no. 12, p. 125 010, 2019.
- [37] Z. Liu, J. Xu, Q. Cheng, Y. Zhao, Y. Pei, and C. Yang, "Trajectory planning with minimum synthesis error for industrial robots using screw theory," *International Journal of Precision Engineering and Manufacturing*, vol. 19, no. 2, pp. 183–193, 2018.
- [38] J. T. Betts, "Survey of numerical methods for trajectory optimization," *Journal of Guidance, Control, and Dynamics*, vol. 21, no. 2, pp. 193–207, 1998.

- [39] J. Betts, *Practical Methods for Optimal Control using Nonlinear Programming*. Philadelphia: Society for Industrial and Applied Mathematics, 2010, ISBN: 978-0-89871-688-7.
- [40] A. V. Rao, “A survey of numerical methods for optimal control,” *Advances in the Astronautical Sciences*, vol. 135, no. 1, pp. 497–528, 2009.
- [41] H. Gattringer, R. Riepl, and M. Neubauer, “Optimizing industrial robots for accurate high-speed applications,” *Journal of Industrial Engineering*, vol. 2013, pp. 1–12, 2013.
- [42] Y. M. Zhao, Y. Lin, F. Xi, and S. Guo, “Calibration-based iterative learning control for path tracking of industrial robots,” *IEEE Transactions on Industrial Electronics*, vol. 62, no. 5, pp. 2921–2929, 2015.
- [43] P. Stuckelmaier, M. Grotjahn, and C. Frager, “Iterative improvement of path accuracy of industrial robots using external measurements,” in *Proceedings of the International Conference on Advanced Intelligent Mechatronics*, Munich, Germany, Jul. 2017, pp. 688–693.
- [44] W. Verdonck and J. Swevers, “Improving the dynamic accuracy of industrial robots by trajectory pre-compensation,” in *Proceedings of the IEEE International Conference on Robotics and Automation*, vol. 4, Washington, DC, USA, Aug. 2002, pp. 3423–3428.
- [45] B. C. Hall, *Lie Groups, Lie Algebras, and Representations*. New York: Springer International Publishing, 2015, ISBN: 978-3-319-13467-3.
- [46] T. Glück, A. Kugi, and A. Steinböck, “Fortgeschrittene Methoden der nichtlinearen Regelung,” Automation and Control Institute (ACIN), TU Wien, 2019, Lecture Notes, URL: <https://www.acin.tuwien.ac.at/en/master/fortgeschrittene-methoden-der-nichtlinearen-regelung/>, Last visited on 01.09.2020.
- [47] A. M. Aurand, J. S. Dufour, and W. S. Marras, “Accuracy map of an optical motion capture system with 42 or 21 cameras in a large measurement volume,” *Journal of Biomechanics*, vol. 58, pp. 237–240, 2017.
- [48] J. A. E. Andersson, J. Gillis, G. Horn, J. B. Rawlings, and M. Diehl, “CasADi: a software framework for nonlinear optimization and optimal control,” *Mathematical Programming Computation*, vol. 11, no. 1, pp. 1–36, 2018.
- [49] A. Wächter and L. T. Biegler, “On the implementation of an interior-point filter line-search algorithm for large-scale nonlinear programming,” *Mathematical Programming*, vol. 106, no. 1, pp. 25–57, 2005.
- [50] HSL, *A collection of Fortran codes for large scale scientific computation*. Version 2019.05.21, Sep. 2020. eprint: <http://www.hsl.rl.ac.uk/ipopt/>.

Eidesstattliche Erklärung

Hiermit erkläre ich, dass die vorliegende Arbeit gemäß dem Code of Conduct – Regeln zur Sicherung guter wissenschaftlicher Praxis (in der aktuellen Fassung des jeweiligen Mitteilungsblattes der TU Wien), insbesondere ohne unzulässige Hilfe Dritter und ohne Benutzung anderer als der angegebenen Hilfsmittel, angefertigt wurde. Die aus anderen Quellen direkt oder indirekt übernommenen Daten und Konzepte sind unter Angabe der Quelle gekennzeichnet. Die Arbeit wurde bisher weder im In- noch im Ausland in gleicher oder in ähnlicher Form in anderen Prüfungsverfahren vorgelegt.

Vienna, 10. November 2020

Ing. Robert Sturmlechner, BSc